Thèse

Présentée a

l'Université de Lille

Ecole doctorale Sciences de la Matière, du Rayonnement et de l'Environnement

Pour obtenir le grade de

Docteur De l'Université

Spécialité: Sciences des Matériaux

Srinivasan MAHENDRAN

Modélisation numérique des propriétés de cœurs de dislocations dans l'Olivine (Mg_2SiO_4)

Soutenance prévue le 3 juillet 2018, devant le jury compose de

Prof. Sandrine BROCHARD	Université de Poitiers	Rapporteur
Prof. Sandro SCANDOLO	International Centre for Theoretical Physics, Trieste	Rapporteur
Dr. Andréa TOMMASI	Université de Montpellier 2	Examinateur
Dr. Andrew WALKER	Université de Leeds	Examinateur
Prof. Philippe CARREZ	Université de Lille	Directeur de thèse
Prof. Patrick CORDIER	Université de Lille	Co-directeur de thèse

Thesis

Presented at

l'Université de Lille

Ecole doctorale Sciences de la Matière, du Rayonnement et de l'Environnement

To obtain the degree of

Docteur De l'Université

In Materials Science

Srinivasan MAHENDRAN

Numerical modelling of dislocation core properties in olivine (Mg_2SiO_4)

Defence scheduled on 3 July 2018, before the jury composed of

Prof. Sandrine BROCHARD	University of Poitiers	Reviewer
Prof. Sandro SCANDOLO	International Centre for Theoretical Physics, Trieste	Reviewer
Dr. Andréa TOMMASI	University of Montpellier 2	Examiner
Dr. Andrew WALKER	University of Leeds	Examiner
Prof. Philippe CARREZ	University of Lille	Supervisor
Prof. Patrick CORDIER	University of Lille	Co-supervisor

Abstract

Convection is a heat transfer process in which heat in the system is transmitted in a fluid like manner. It is widely accepted that the dissipation of heat from the core to the surface of the Earth through a thermally insulating mantle is only possible by a convective process. Mantle convection is responsible for a large number of geological activities that occur on the surface of the Earth such as plate tectonic, volcanism, etc. It involves plastic deformation of mantle minerals. Among the several layers of the Earth's interior, the outer most layer beneath the thin crust is the upper mantle. One of the most common minerals found in the upper mantle is the olivine $(Mg,Fe)_2SiO_4$. Knowledge of the deformation mechanisms of olivine is important for the understanding of flow and seismic anisotropy in the Earth's upper mantle. Plastic deformation of olivine has been the subject of numerous experimental studies highlighting the importance of dislocations of Burgers vector [100] and [001]. In this work, we report a numerical modelling at the atomic scale of dislocation core structures and slip system properties in Mg_2SiO_4 forsterite, at pressures relevant to upper mantle conditions. Computations are performed using the so-called THB1 empirical potential set for Mg_2SiO_4 and molecular statics. The energy landscape associated with the dislocation mobility are computed with the help of nudge elastic band calculations. Therefore, with this work, we were able to accurately predict the different possible dislocation core structures and some of their intrinsic properties. In particular, we show that at ambient pressure [100](010) and [001]{110} correspond to the primary slip systems of forsterite. Moreover, we propose an explanation for the so-called "pencil glide" mechanism based on the occurrence of several dislocation core configurations for the screw dislocation of [100] Burgers vector. Finally, the modelling of the intrinsic dislocation properties in a pressure range relevant of the Earth's upper mantle allows to address the effect of high pressure on the primary slip systems of olivine.

Résumé

Il est aujourd'hui largement accepté que les mécanismes de convection mantellique dans le manteau supérieur sont reliés aux propriétés plastiques de l'olivine constituant principale du manteau supérieur. Ce minéral, un silicate de composition $(Mg,Fe)_2SiO_4$, se déforme essentiellement par glissement de dislocations de vecteurs de Burgers [100] et [001]. Dans le cadre de ce travail de thèse, nous avons donc choisi de modéliser les propriétés de ces dislocations ainsi que les systèmes de glissement potentiels de l'olivine à partir de calculs à l'échelle atomique. L'ensemble des calculs ont été effectués à l'aide du potentiel THB1. Une fois les structures de cœurs des défauts déterminées, les paysages énergétiques associés au glissement des dislocations ont été analysés par la méthode « Nudge Elastic Band ». A basse pression, la modélisation atomique montre que les systèmes [100](010) et [001]{110} correspondent aux systèmes de glissement primaires de l'olivine. L'étude des paysages énergétiques des dislocations nous permet de plus de rationaliser les observations expérimentales de « pencil glide » reportées dans l'olivine depuis les années 70 et de proposer un mécanisme original de blocage-déblocage pour le glissement des dislocations de vecteurs de Burgers [001]. Enfin, l'application de ce type de modélisation aux conditions de pression du manteau supérieur (0-10 GPa) confirme l'existence d'un effet de durcissement de la pression sur le glissement des dislocations de vecteur de Burgers [100].

Table of contents

1. Introduction

After 4.6 billion years since the formation of the Earth, its interior is still hot. The heat flux coming towards the Earth surface is measured to be about 46±3 TW for the whole planet (Jaupart and Mareschal 2015). How is this heat transferred to the surface? Since rocks are opaque and insulating, mantle convection is widely accepted to be the major contributor for the transfer of heat to the surface, and the Earth's mantle can be considered to behave over geological timescales as a fluid endowed with a very high viscosity (10^{21}-10^{22} Pa s) (Yokokura 1981). The convection movements occur by the plastic deformation of rocks, which is controlled by the plastic properties and chemical composition of their constituent minerals. Plastic deformation occurs through the deformation of the constituent crystals; this involves migration of defects such as point defects, dislocations, grain boundaries, etc. The knowledge on these defects helps us to link our understanding on the microscopic scale with the behaviours observed at macroscopic scale.

1.1. Earth's interior

The mineral olivine forms a solid solution between forsterite (Mg_2SiO_4) and fayalite (Fe_2SiO_4). Being one of the most abundant mineral in the Earth's upper mantle, olivine is a key mineral which controls the rheology of the upper mantle. The Earth's interior is divided into several layers; the upper mantle corresponds to the first subdivision of it, as deduced from the analysis of the time travel of seismic waves. One of the standards among seismological models is the preliminary reference Earth model (PREM) proposed by Dziewonski and Anderson (1981) (Figure 1.1). This is one-dimensional model in which all the physical parameters are assumed to change with depth only.

According to seismic information, several discontinuities are observed in the Earth's interior. The crust is the upper most divided into oceanic and continental crust (~7 – 70 km), below is the mantle divided into two layers, the upper mantle (~410 km) and the lower mantle (~670 – 2890 km), with a transition zone (~410 – 670 km) sandwiched between the two mantle layers and the Earth core (~2890 – 6370 km) subdivided into a liquid outer core and a solid inner core.

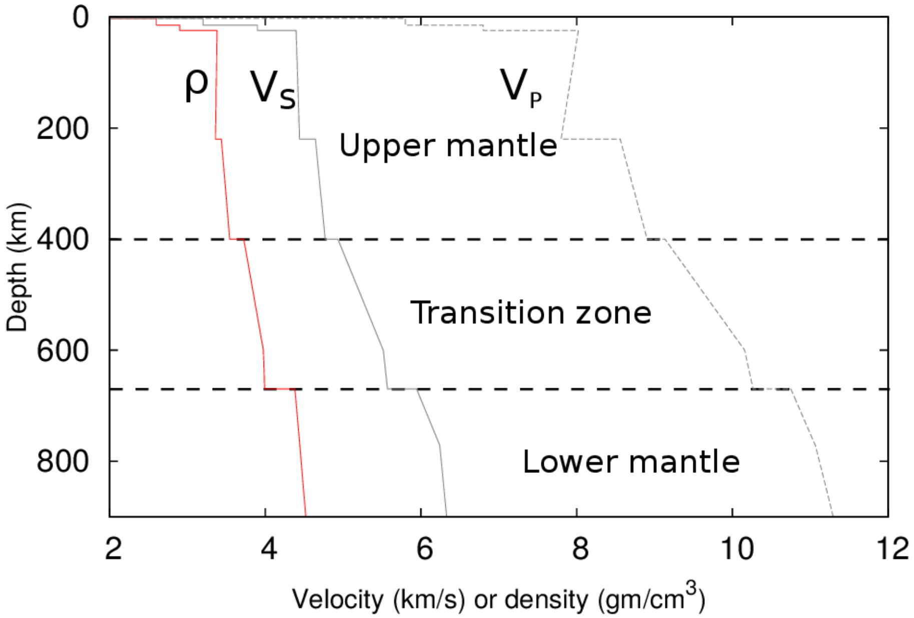

Figure 1.1. *Preliminary reference Earth model (PREM) from Dziewonski and Anderson (1981). Density and seismic velocities plotted as a function of depth.*

The data available on seismic wave velocities are mostly influenced by the density and the elastic properties of the rock aggregates. For instance, the outer core is known to be made mainly of liquid, as the shear waves vanish and the compression waves are solely recorded. Therefore, the discontinuities in PREM model can be interpreted as transformation of rock aggregates or material. Such modifications being driven by thermodynamics stability of minerals as pressure and temperature increase with depth.

Ringwood (1962; 1975) proposed a model on the chemical composition of the upper mantle known as the pyrolytic model. Based on this model (Figure 1.2), the upper mantle is composed of olivine $(Mg,Fe)_2SiO_4$, pyroxene $(Mg,Fe,Ca)_2Si_2O_6$ and garnets $(Mg,Fe,Ca)_3Al_2Si_3O_{12}$. At ~410 km, the pressure and temperature in the mantle reaches 13 GPa and 1400 °C respectively, under these conditions olivine transforms into a high-pressure polymorph named wadsleyite. Deeper into the transition zone (~520 km) wadsleyite transforms into ringwoodite, a denser high-pressure polymorph of olivine. At depths beyond ~670 km, (where the P, T conditions are 23 GPa, 1600 °C), ringwoodite and garnets decompose into a two-phases aggregate composed of a silicate with a perovskite structure now known as bridgmanite and ferropericlase (Fp) (Mg,Fe)O.

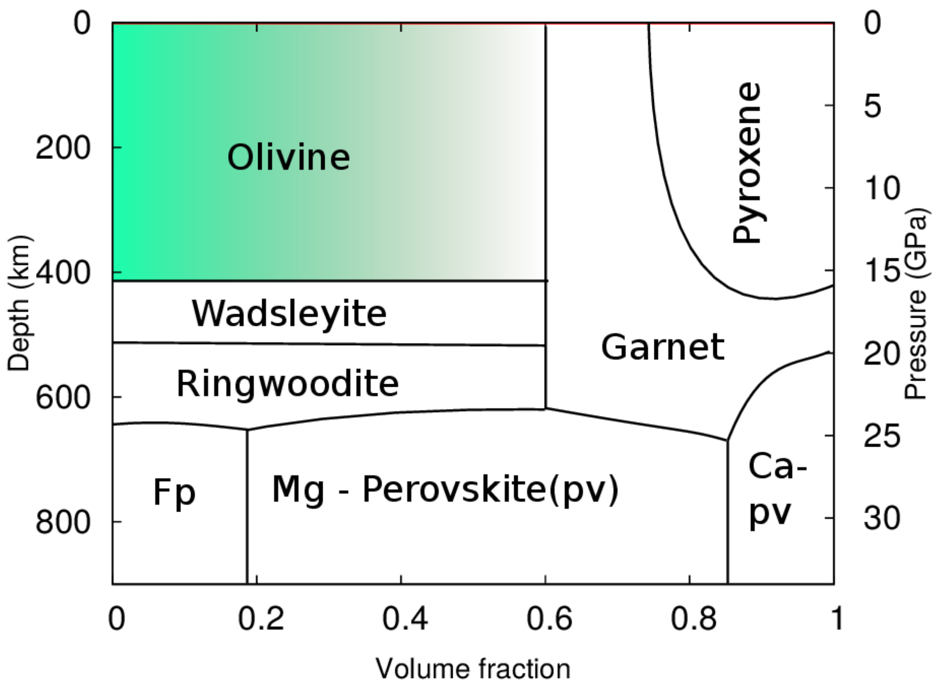

Figure 1.2. *Simplified mineralogy of the pyrolytic mantle layers of the Earth as a function of depth, pressure and volume fraction (Brown and Shankland (1981)).*

1.2. Olivine crystal structure

Olivine is an olive green mineral which exists as a solid solution of $(Mg,Fe)_2SiO_4$. In this thesis, we will focus on the magnesium-rich end-member forsterite (Mg_2SiO_4). It is close to the average composition of olivine in the upper mantle which contains a little bit less than 10% of iron. The melting point of forsterite and fayalite are 2163 K and 1473 K respectively (Bowen and Andersen 1914; Ohtani and Kumazawa 1981; Klein and Hurlbut 1999).

Forsterite corresponds to an orthorhombic crystal structure, which can be described within the *Pbnm* space group. The crystal structure which contains isolated SiO_4 tetrahedra can be viewed as slightly distorted hexagonal close packed (hcp) lattice of oxygen anions (Poirier 1975), with one eighth of the octahedral sites occupied by magnesium cations. In the *Pbnm* space group, the lattice constants (at ambient pressure and temperature) are a = 4.756 Å, b = 10.207 Å, c = 5.98 Å (Smyth and Hazen 1973).

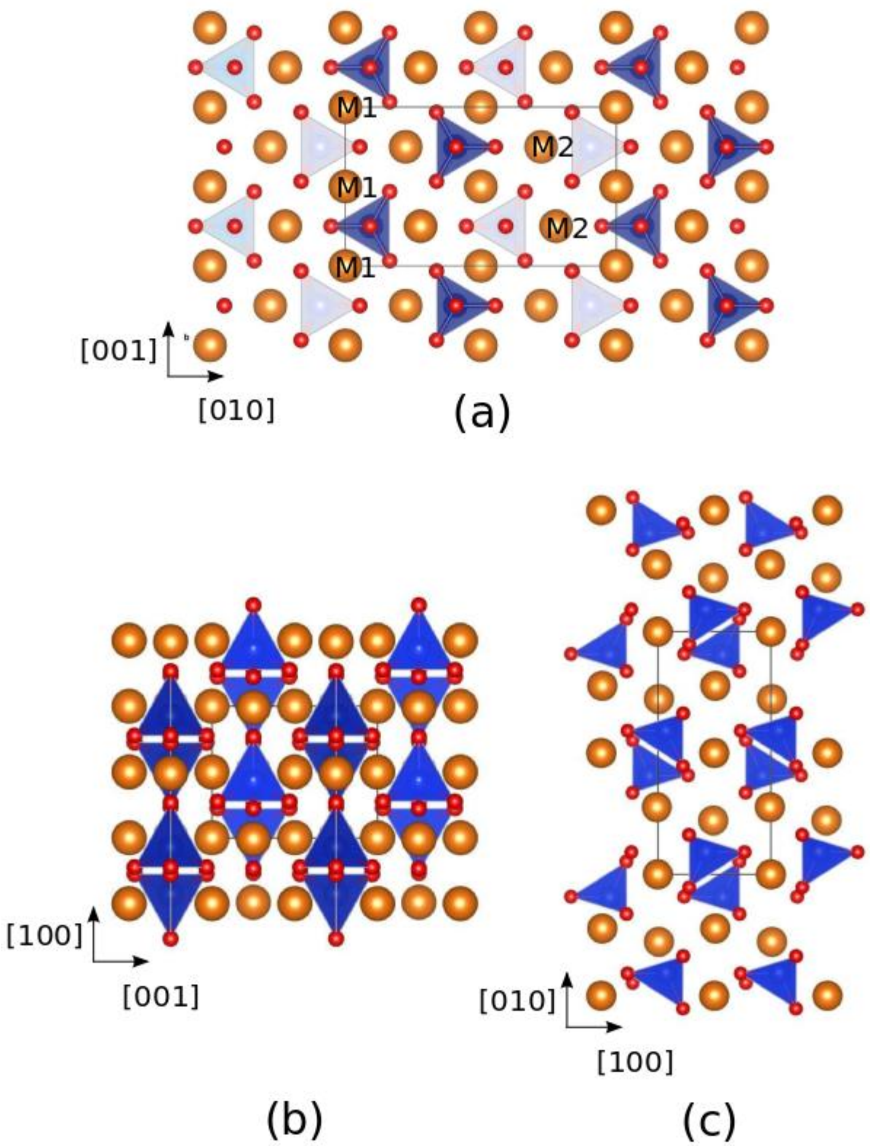

Figure 1.3. *The structure of orthorhombic forsterite, the Mg rich end-member of olivine described here with the Pbnm space group. The crystal structure projected along (a) [100] (b) [010] (c) [001] directions with unit cell marked with black line. Magnesium atoms are in yellow, oxygen is in red and silicon is in blue, located inside the* SiO_4 *tetrahedral units. The isolated* SiO_4 *tetrahedra are joined by Mg cations located in the M1 sites at the inversion centres. The Mg cations in the M2 site lie on a mirror plane.*

Figure 1.3 (a) shows the projection of forsterite unit cell SiO_4 tetrahedra viewed along [100] direction. The isolated tetraheadra point alternatively up and down along rows parallel to [001]. Each level of isolated tetrahedra are connected via octahedra containing metallic cations (Mg^{2+}). The metal cations M1 lie in the inversion centres between two SiO_4 tetrahedral units and M2 cations lie in the mirror plane (Deer *et al.* 1982).

1.3. Elastic properties of olivine

Based on the orthorhombic crystal symmetry, the elastic stiffness matrix, C_{ij}, of olivine consists of nine independent elastic constants.

$$\begin{bmatrix} C_{11} & C_{12} & C_{13} & 0 & 0 & 0 \\ C_{21} & C_{22} & C_{23} & 0 & 0 & 0 \\ C_{31} & C_{32} & C_{33} & 0 & 0 & 0 \\ 0 & 0 & 0 & C_{44} & 0 & 0 \\ 0 & 0 & 0 & 0 & C_{55} & 0 \\ 0 & 0 & 0 & 0 & 0 & C_{66} \end{bmatrix}$$

The nine elastic constant were initially determined by Isaak *et al.* (1989) at high temperature conditions. The effect of pressure on the elastic constants has been measured by Shimizu *et al.* (1982) and Zha *et al.* (1988) in a pressure range of 4 GPa and 16 GPa respectively (Table 1.1). The bulk modulus increases from 120 - 200 GPa and the shear modulus increases from 80 - 90 GPa at a pressure range of 0 – 16 GPa (Li *et al.* 1996; Zha *et al.* 1996; Yoneda and Morioka 1992) (Figure 1.4).

Table 1.1. *Single crystal elastic moduli of San Carlos Olivine (in GPa) as a function of pressure. The experimental results are gathered from Zha et al. (1996).*

Pressure (GPa)	C_{11}	C_{22}	C_{33}	C_{44}	C_{55}	C_{66}	C_{12}	C_{13}	C_{23}
2.5	332.5	209.4	251.4	68.7	80.1	82.7	80.7	80.2	84.4
5.0	352.8	224.2	267.1	70.8	85.7	90.2	91.2	92.7	95.2
8.1	378.9	244.0	283.5	77.6	91.9	96.3	100.8	102.3	104.7
14.1	395.3	270.4	295.3	81.2	96.6	103.6	122.5	118.0	123.0
18.8	424.1	270.4	326.8	86.3	99.8	112.8	129.2	133.2	138.2

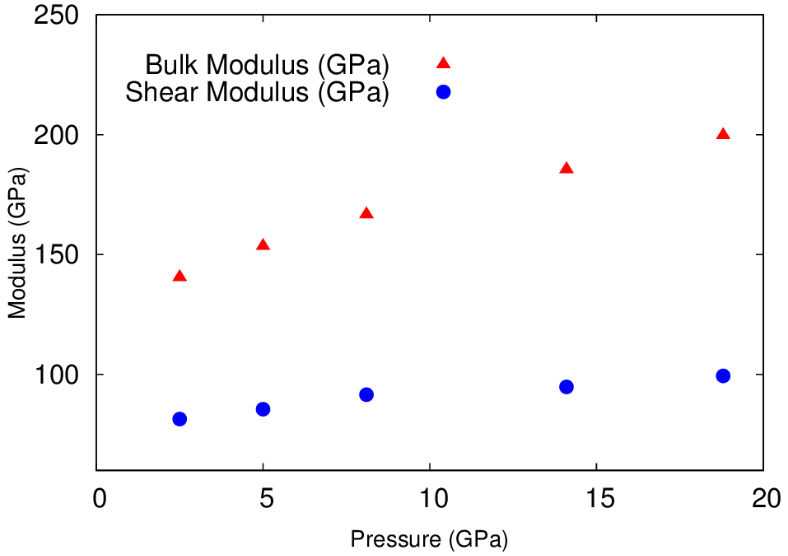

Figure 1.4. *Evolution of Bulk (K) and shear modulus (μ) as a function of pressure experimentally determined for single crystal San Carlos olivine (Zha et al. 1996). The data yields a pressure derivative of* K_0' *= 4 and* μ_0' *= 1.6 the values compares well with values of* K_0' *= 4.4 and* μ_0' *= 1.3 (Li et al. 1996).*

1.4. Plastic properties of olivine

For modelling the convection of the Earth's mantle, one needs information on the plastic properties of the constitutive materials, starting with olivine. As the elastic energy of a dislocation is proportional to the square of Burgers vector ($E_{el} \propto b^2$), this relation makes [010] dislocation energetically least favourable. Based on the hexagonal close packed arrangement of oxygen sub-lattice, Poirier (1975) further proposed the following slip systems: [001] dislocation gliding in (100), (010), {110} and [100] dislocation gliding in (010), (001), {011} and {031} (Figure 1.5).

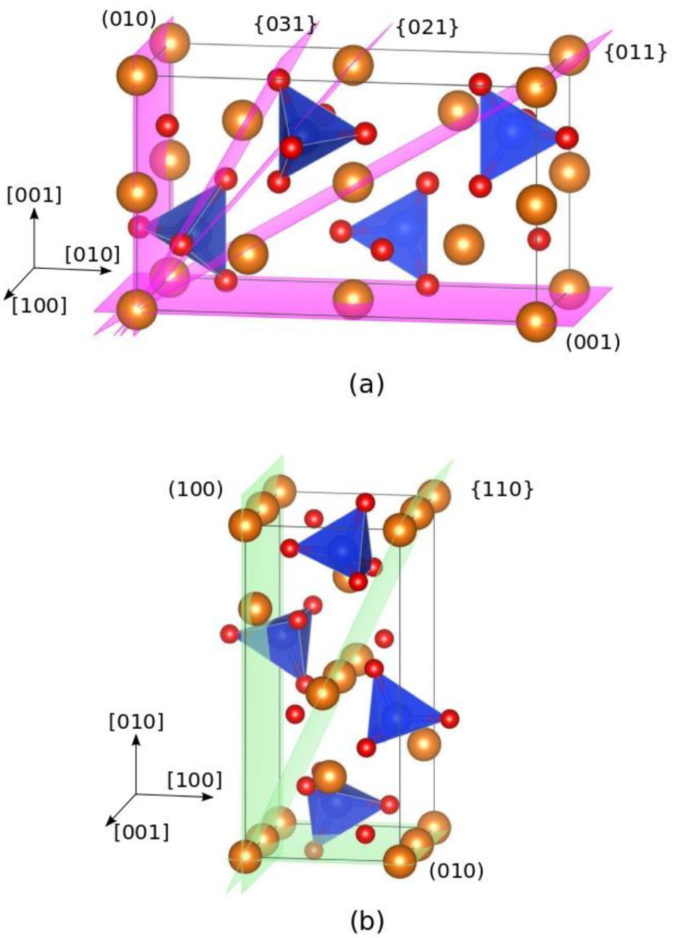

Figure 1.5. *Forsterite unit cell with possible slip planes of (a) [100] and (b) [001] dislocations.*

In natural samples, from the observations made with optical microscopy and transmission electron microscopy (TEM) techniques, one confirms that glide along [010] is unfavourable. Only dislocations with [100] and [001] Burgers vectors are commonly observed, whereas precise determination of slip systems is difficult and almost all the potential glides plane have been reported (Gueguen 1979; Kohlstedt *et al.* 1976).

From the deformation experiment performed at ambient pressure on polycrystalline olivine Raleigh (1968) shows that the plastic deformation results from activation of [001] dislocations at low temperature and high stress condition, whereas at temperature above 1000 °C Carter and Ave'Lallemant (1970) observed activation of [100] dislocations. At temperature greater than 1300 °C, only [100](010) seems to be activated. To proceed further, deformation experiments have been performed on single crystals. Based on the orientation of the single crystals, the activation of preferential slip planes can be analysed. From the experimental results (Phakey *et al*. 1972, Durham *et al*. 1977, Evans and Goetze 1979, Darot and Gueguen 1981, Gaboriaud *et al*. 1981, Gueguen and Darot 1982, Wang *et al*. 1988, Barber *et al*. 2010) [100] glide at high temperature and [001] glide at low temperature in various slip planes are observed. A composite non-crystallographic glide of [100] dislocation in {0kl} has long been reported (Raleigh 1968), such a mechanism is called the pencil glide.

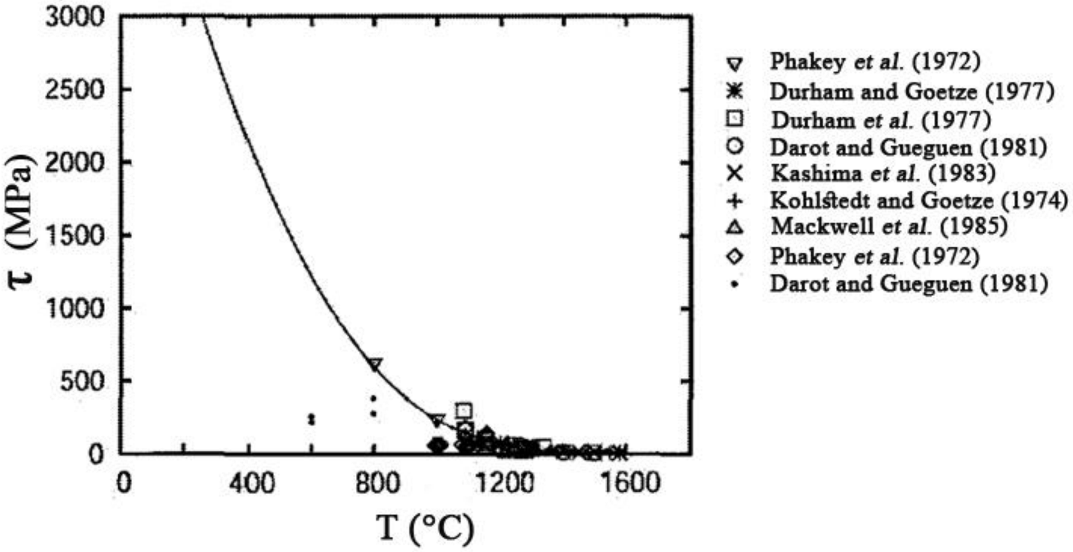

Figure 1.6. *Summary of critical resolved shear stress values for [100] dislocation glide, obtained from various single crystal deformation experiments. (adapted from the PhD thesis of Durinck (2005c)).*

More importantly, deformation experiments performed on single crystals give access to quantitative information on the mechanical behaviour of slip systems. In particular, critical resolved shear stress have been reported for at least four slip systems: [100](010), [001](010), [001](100),[001]{110}. From Figure 1.7 it is visible that data are available for [001] glide at low temperature, unlike the case of [100] where the glide is observed only at high temperature experimental conditions Figure 1.6.

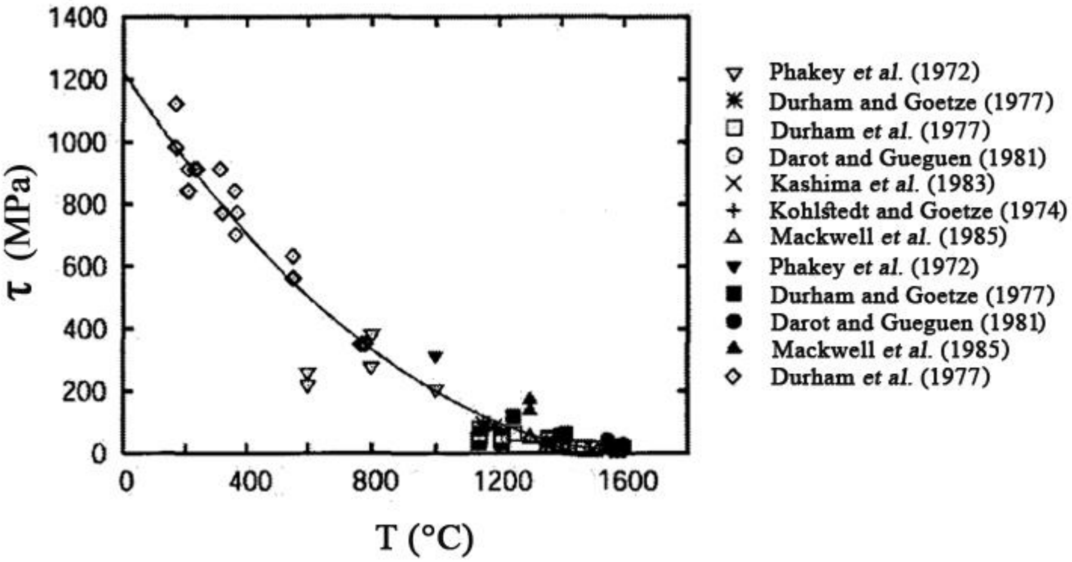

Figure 1.7. *Summary of critical resolved shear stress values for [001] dislocation glide, obtained from various single crystal deformation experiments. (adapted from the PhD thesis of Durinck (2005c)).*

In the context of upper mantle, temperature is not the only factor that influences the plastic properties. At depth close to the transition zone, the pressure in the mantle rises to 13 GPa. Also incorporation of water in the mantle is reported to influence plasticity. Thus, over the past two decades, deformation experiments have been performed to study the influence on plasticity due to the effect of pressure and the effect of incorporation of water. The experiments were carried out using both polycrystals and single crystals. For experiments performed with polycrystals, the analysis in terms of slip system is often performed through the analysis of crystal preferred orientation (CPO). According to change in CPO, Jung and Karato (2001) show that water has an influence on the preferential slip systems in olivine by promoting dislocation with [001] Burgers vectors. On the other hand, Couvy *et al.* (2004) show that pressure also strongly enhances activation of [100] glide under Earth mantle conditions (11 GPa, 1400 °C). Using single crystal deformation experiments, Raterron *et al.* (2005, 2007, 2009, 2011) reaches, with a series of single crystals deformation experiments at mantle pressure conditions a similar kind of conclusion, with an inversion of preferential slip system from [001] to [100] at high pressure.

Several explanations have been proposed to support one or the other conclusion, however a full theoretical understanding is still needed. For instance, either pressure or water has an effect on dislocation activity, such effect may have its origin from the core structure of the defect. It is well known that fundamental properties of dislocations, such as lattice friction, glide velocity, and also in a lesser extent climb velocity, are directly related to the atomic arrangements within the vicinity of the dislocation core, or to impurities.

Up to now, only a few works have been dedicated to study the atomic arrangement in the dislocation cores in olivine. The primary studies performed by Durinck and co-workers (2005a; 2005b; 2007) using Density Function Theory (DFT) calculations to compute generalised stacking fault (GSF) energies and to deduce the dislocation core configurations according to the Peierls Nabarro (PN) model. At the same period, Walker and co-workers (Walker *et al.* 2005a; Walker *et al.* 2005b; Carrez *et al.* 2008), used empirical potential models to compute dislocation core structures via atomistic simulations. However, due to the limitations in computational efficiency of the code existing at that time, mechanical properties have not been infered from the atomic core structure. The PN model is rather promising as it can provide some mechanical information through the computation of the Peierls stress, but has to be handled with great care while dealing with complex crystal structure. In general, the PN model gives satisfactory results in case of planar core configurations, it can also lead to several artefacts when the dislocations are non-planar or dissociated and computationally demanding (Schoeck 2005; 2006).

1.5. Plan of thesis

In this work, we intent to revisit the dislocation core structures of olivine (Mg_2SiO_4). We investigate the two Burgers vector [100] and [001], over a pressure range 0-10 GPa corresponding to upper mantle conditions. This work only focuses on screw dislocations, since uncertainties remain on the slip systems. It is common to analysis the screw core configurations to infer the potential slip systems for the plane where the cores tend to spread. To avoid artefacts encountered in the past, approaches such as PN model or generalisation of PN model will not be used, and we will perform full atomistic calculations. But still Peierls stresses determination will be carried out directly from the atomic configuration. Also as an advantage, full atomistic calculations give access to the energetic landscape around dislocation core. As described in the following chapter, the energy landscape along dislocation pathway will be computed using nudged elastic band (NEB) approach, a method used to investigate transition state paths. The results presented in chapters 4 and 5 correspond to [100] and [001] dislocation cores respectively. Finally, a discussion chapter will summarize our results and put them in perspective with the current state of the art of olivine plastic properties.

As described in the following pages, we have chosen to work with the open-source classical molecular mechanics code called the LAMMPS and the THB1 force field to describe forsterite. At the beginning of this work, THB1 potential was not available into LAMMPS, chapter 3 is thus a technical chapter dedicated to our implementation of THB1 potential model to LAMMPS library and some important checkpoints computations performed before addressing the heart of this thesis.

2. Model and methodology

Interatomic pair potentials play a significant role in performing molecular and materials simulation. In the process of modelling ionic or semi-ionic material like forsterite, various key parameters have to be considered. This chapter introduces basics of pairwise potential model; followed by the necessity of an interatomic potential library with core-shell approximation. The potential energy and its corresponding force fields are the basic input for the energy minimization and transition path algorithms. This chapter further introduces basic methodology of atomistic simulations that are performed in this work to the study the dislocation core structure and mobility of dislocation.

2.1 Interatomic interactions

Quantum mechanical methods can be used to predict mechanical behaviour and properties of materials accurately but are computationally expensive to model systems of large dimensions (*i.e.*, having few thousand atoms). The task of modelling dislocations and defects in olivine involves systems too large to be solved quantum mechanically. The density function theory (DFT) provides amendable numerical solutions to Schrodinger's equation. It is accepted as a strong method to solve bonding problems, whereas the expense of computational cost limits the simulation to few hundreds of atoms. Alternatively, tight-binding (TB) methods reduces the computational cost by parameterising many DFT integrals, whereas its description of electronic structure consisting of neutral atoms makes it difficult to model ionic systems. Force fields methods ignore the electron field and calculates energy (U) as an analytical/numerical function based on nuclear positions (equation 2.1).

$$U = U(r_1, r_2, r_3 \dots r_N) \tag{2.1}$$

$$U = \sum_{i}^{N} U_i + \frac{1}{2!}\sum_{i}^{N}\sum_{j}^{N} U_{ij} + \frac{1}{3!}\sum_{i}^{N}\sum_{j}^{N}\sum_{k}^{N} U_{ijk} + \cdots \tag{2.2}$$

Here, the total energy of the system can be decomposed into interactions between different numbers of atoms or ions as in equation 2.2. U_i represents the self-energy of the atoms. U_{ij} is the pairwise potential energy term that can be written as a sum of interaction of two atoms i and j separated by a distance r_{ij}. When a triad of atoms is considered, their energy of interaction is given by U_{ijk}. For example, the Stillinger-Weber potential (Stillinger and Weber 1985) used for a system of silicon atoms, includes two-body and three-body interactions. The three-body term penalizes the deviation of bond angle from tetrahedral angle (109.47 degree). The above decomposition is more accurate when order of interaction increases, but it is important to truncate the order at some stage.

This superposition of pairwise interactions works well to model ionic materials and semiconductor materials, as the bonds are well localised. Unlike for the case of metals the bonds are shared by many atoms. The embedded atom method (EAM) (Daw and Baskes 1984) is a well-suited model for atomistic modelling of metals. The embedded function of the EAM function is non-linear, and the many-body term included in this approach cannot be reproduced by superposition of any order of pairwise interactions.

In the following, we describe more precisely the modelling of ionic systems. Initially for modelling ionic or semi-ionic materials, only two body terms are considered. For a simple case, one can imagine an ionic solid being made of cations and anions, with frozen electron densities. In such cases the opposite charged ions attract each other due to Coulombic attraction and the like charged ions experience a similar repulsive force. The closest neighbour ions with opposite charges result in a strong net attractive force, which will tend to contract the system to arrive in a lower energy configuration. In order to bring the system in equilibrium a counter balancing repulsive force is required. This force can be obtained from the overlap of electron density of two ions, irrespective of the type of charge, which can be explained by Pauli repulsion between electrons. Thus the total energy of the system can be expressed as follows:

$$U_{Total} = U_{Coulomb} + U_{Short} \tag{2.3}$$

Here in equation 2.3, the Coulomb energy, $U_{Coulomb}$, is obtained by the summation of interactions of all atomic charges in the system, and this is an important component of cohesive energy. The short range energy term, U_{Short}, represents the rest of interactions in the system including Pauli repulsion, covalent and dispersive attractive terms.

2.1.1 Ionic polarisation

From the above explanation, the ions have a frozen spherical electron density and are represented with a point charge. This gives a simple representation, whereas for better accuracy it is necessary to include the effect of polarisation. For instance, in the case of an oxide with anion O^{2-}, first electron affinity of oxygen is favourable, while the second electron affinity is endothermic due to the Coulombic repulsion term which is strongly perturbed by the local environment (Gale 2005). Hence it is necessary to include a polarisation term to produce reliable results.

An additional point dipole term can be added to the point charge representation of ion. With inclusion of dipole polarisability $\alpha_{Polarisation}$, in presence of an electric field **E** the dipole moment **μ** is given in equation 2.4 which results in polarisation energy U_{PC} (equation 2.5), results in a total energy combination given in equation 2.6.

$$\mu = \alpha_{Polarisation} E \tag{2.4}$$

$$U_{PC} = -\frac{1}{2}\alpha_{Polarisation} E^2 \tag{2.5}$$

$$U_{Total} = U_{Coulomb} + U_{Short} + U_{PC} \tag{2.6}$$

Hence it is straightforward to include this polarisation self-energy contribution of each ion to the total energy. Whereas assuming a constant value of $\alpha_{Polarisation}$ prevents the system to polarise further beyond this value. It leads to imbalance in the ratio of increase in attractive term compared to the repulsive term, results in collision of ions during defect calculations. When the distance between two ions is zero the short range term (1/r) tends to infinity numerically. To avoid this adverse effect, the value of polarisation has to be iteratively solved.

2.1.2 The core-shell model

The above discussed collision of ions may lead to polarisation catastrophe (Catlow *et al.* 1982; Gale 2005). This problem can be overcome by using the core-shell model, a mechanical description of ions proposed by Dick and Overhauser (1958). This model describes each ion as two particles, a massive "core" which represents the nucleus and core electrons, and a massless "shell" which represents the polarisable valance shell electrons. The core and shell are connected using a spring with a spring constant *K*. The core is positively charged and the shell is negatively charged. The sum of the charges gives the charge of the ion. Both core and shell holding a positive charge is common in representation of a cation. A schematic description of the core-shell model is given in figure 2.1. The dipole moment can be modelled by the displacement of shell with respect to the core. In such a description the $\alpha_{Polarisation}$ can be related to the core-shell model parameters K and to the charge of the shell q_{shell} using a simple relation as follows:

$$\alpha_{Polarisation} = \frac{q_{shell}^{2}}{K} \tag{2.7}$$

From this description the potential library will consists of a set of atoms with charges, analytical function to model Pauli’s repulsion and covalent terms and a representation of polarisation with core-shell model ($U_{core\text{-}shell}$). Hence the split of energy is given as follows:

$$U_{Total} = U_{Coulomb} + U_{Short} + U_{core-shell} \tag{2.8}$$

In this work, we use the core-shell model potential library THB1 proposed by Price and Parker (1987) to model forsterite and its high-pressure polymorphs. This library supplements an additional three-body term, which helps to include the covalence of the bonding within the SiO_4 tetrahedra.

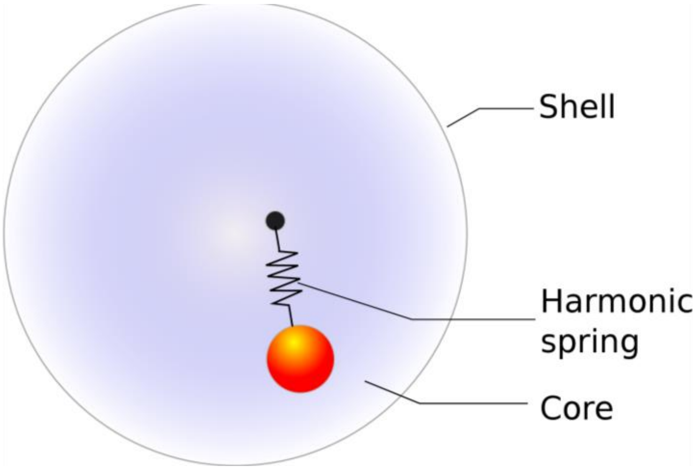

Figure 2.1. *Schematic representation of an ion in the core-shell model. Each ion is made of two parts. The core represents the nucleus and the shell represents the electron cloud. These two parts are connected with each other using a harmonic spring.*

The above mentioned core-shell approximation gives an effective solution to model ionic materials. However, the accuracy of core-shell methods suffers a drawback in computation of elastic constants and phonon dispersion curves in rock salts (like MgO, CaO, NaCl). In principle for centrosymmetric cubic crystals, the pairwise potential models obey Cauchy's relation $C_{44} = C_{12}$. But experimental results in rock salts suggests that $C_{44}/C_{12} > 1$ (Matsui 1998). In order to solve this problem, the "breathing shell" model (Schroder 1966; Sangster *et al.* 1970; Sangster 1973) is found to be more accurate than the normal shell model in modelling of rock salts (Sangster *et al.* 1970, Matsui 1998). In this work for the modelling of forsterite silicate we keep a normal core-shell model library with THB1 parameterisation.

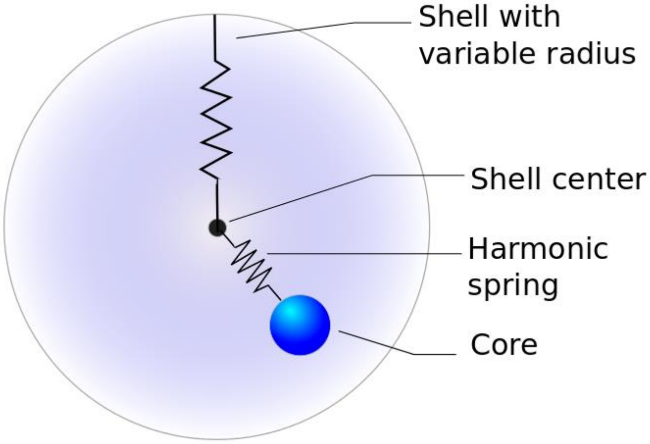

Figure 2.2. *Schematic representation of an ion using breathing shell model. The shell has a variable radius, which is allowed to deform isotropically due to the effect of neighbouring ions. The core and the shell are connected using a harmonic spring.*

2.1.3 THB1 Potential library

The THB1 potential is fully ionic empirical potential for accurate modelling the properties of forsterite (Mg_2SiO_4) and its high-pressure polymorphs. The effort of modelling forsterite using atomic simulation has a long and continuous history (Price and Parker 1984; Price et al. 1985 and Catlow et al. 1986). These models concentrated on the pairwise interactions but ignored the effect of many-body interactions. Whereas, the success of three-body interaction in modelling complex silicates (Matsui and Bushing 1984; Sanders et al. 1984) using bond-bending term, lead to the development of potential model of THB1 (Price and Parker 1987). The core-shell approximation enables every ion to polarize in response to an electric field due to the surrounding ions. Energy decomposition of THB1 model can be described as a summation of four terms as follows,

$$U_{Total} = U_{Coulomb} + U_{Short} + U_{core-shell} + U_{THB} \tag{2.9}$$

$U_{Coulomb}$ represents the long range electrostatic energy term, which arrives as a result of summation of charges of atomic species present in the system. It is given by energy of electron *e*, point charges q_i and q_j associated with ions i and j respectively and the distance of separation between them.

$$U_{Coulomb} = \sum_{ij} e^2 q_i q_j r_{ij}^{-1} \tag{2.10}$$

The ionic materials pose additional challenge in computing the electrostatic term. Coulombic summation is a computationally expensive task due to the long-range character of the interaction. Traditionally the Coulomb summation results in converging of equations under specific conditions, particularly the Madelung problem (Madelung 1919; Gdoutos *et al.* 2010). The Madelung problem was solved with the Ewald summation (Ewald 1921), which through certain mathematical manipulations calculates the conditionally convergent $O(r^{-1})$ Coulomb summation. The Ewald method assumes periodicity of the material. The result of this summation method is less reliable with non-periodic or quasi-periodic systems. Further, this method is computational expensive for large systems. To overcome these drawbacks, we replace the Coulomb term with a Wolf summation method (Wolf *et al.* 1999). The Wolf summation method for accumulation of electrostatic charges, involves a simple modification to the direct pairwise sum but scales approximately linearly with the system size (Fennel *et al.* 2006).

$$U_{Coulomb} = U_{sh} - U_{self} \tag{2.11}$$

$$U_{sh} \approx \frac{1}{2}\sum_{i=1}^{N} \sum_{\substack{j\neq i \\ (r_{ij}<R_c)}} \left(\frac{q_i q_j erfc(\alpha r_{ij})}{r_{ij}} - \lim_{r_{ij}\to R_c} \left\{ \frac{q_i q_j erfc(\alpha r_{ij})}{r_{ij}} \right\} \right) \tag{2.12}$$

$$U_{self} = \left(\frac{erfc(\alpha R_c)}{2R_c} + \frac{\alpha}{\pi^{1/2}} \right) \sum_{i=1}^{N} q_{ion\ i}^2 \tag{2.13}$$

where α is the damping factor and R_c is the cut-off distance for Columbic term. The Coulomb term is split into a charge neutralized Ewald potential term U_{sh} and a self-energy term for each ion U_{self} .

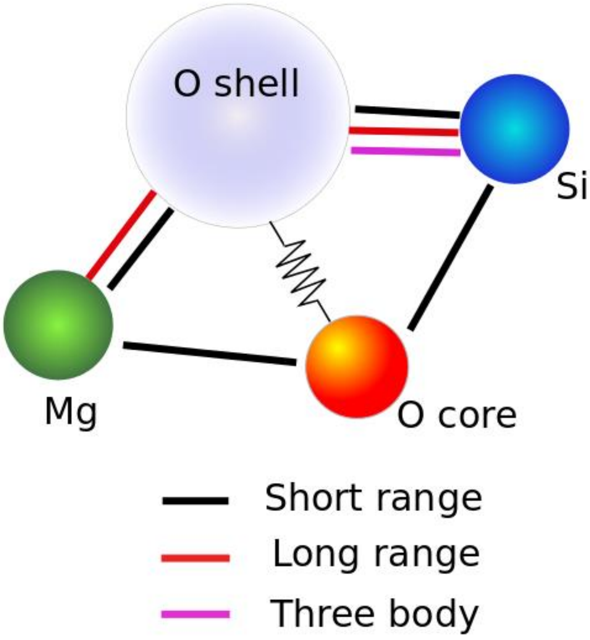

Figure 2.3. *Schematic representation of interactions in the THB1 potential model.*

Each ion is constituted of a nucleus and an electron cloud. U_{Short} is the short-ranged Buckingham potential term used to describe the effect of an electron cloud on nearest neighbour ions. This term is parametrized by three constants A_{ij}, B_{ij} and C_{ij} between ions *i* and *j*.

$$U_{Short} = \sum_{ij} A_{ij} exp\left(-\frac{r_{ij}}{B_{ij}}\right) - C_{ij} r_{ij}^{-6} \tag{2.14}$$

In case of an ion, core and its shell are Coulombically screened from each other and only allowed to interact via the harmonic spring term $U_{core-shell}$. Coupling between the core and its shell is described by this term, which requires shell spring constants $K1_i$, $K2_i$ and the distance of separation between core and its corresponding shell r_i,

$$U_{core-shell} = \frac{K1_i r_i^2}{2} + \frac{K2_i r_i^4}{24} \tag{2.15}$$

Table 2.1. *Parameters for the THB1 potential library proposed by Price and Parker (1987) to model forsterite.*

Charges (units of electronic charge)			**Core - shell spring constant (eV·Å^{-2})**
Ions	**Cores**	**Shells**	
Mg	2.0		
Si	4.0		
O	0.848190	-2.848190	74.92038
Short range term			
	A (eV)	**B (Å)**	**C (eV·Å^6)**
Si – O	1283.90734	0.32052	10.66158
O – O	22764.0	0.149	27.88
Mg – O	1428.5	0.29453	0.0
Harmonic three body term			
	k (eV·rad^{-2})	**θ$_0$ (degrees)**	
O – Si - O	2.09724	109.47	

For accurate modelling of structure and properties of silicates, it is important to describe the directionality of Si-O bonding using a bond-bending term into the potential (Price and Parker 1987, Sanders et al 1984). For that purpose, THB1 uses a harmonic three-body term, with k_{ijk}^{B} being a derivable spring constant, θ_{ijk} is the angle between the O-Si-O three-body term and θ_0 is the constant tetrahedral angle (109.47).

$$U_{THB} = \sum_{ijk} k_{ijk}^{B}\left(\theta_{ijk} - \theta_0\right)^2 \tag{2.16}$$

We implemented the described inter-atomic potential library and the corresponding force fields to LAMMPS molecular mechanics code. A schematic representation of allowed interactions between ions are given in Figure 2.3. The THB1 parameterization used in this work (Table 2.1) was previously derived by Price and Parker (1987) for forsterite.

2.2 Ground state properties

Using DFT or pairwise potential library like THB1 we can compute the potential energy of a system. In either methods, for a system containing N atoms with atomic positions $r_i = (r_1, \ldots r_N)$ known, the potential energy can be computed at a given position, $U = U(r)$. The potential energy landscapes are useful to explain various phenomena in materials science. The important properties of the energy landscapes are the local minima and the transition paths between them. These properties can be computed using the molecular statics framework.

2.2.1 Energy minimisation

Finding minima in potential energy landscape is a key task in molecular statics. For an energy landscape analogous to terrestrial type landscape with mountains, valleys and passes it is relatively easy for the human brain and eye to find minimum locations and pathways. Whereas, to do the same automatically using a set of numerical functions in a computer is complex. The search of a global minimum quickly and confidently is still a very attractive and open topic of research. The search of a “local” minimum or a nearby minimum position in a system can be done using rather simple and quicker algorithms like the Steepest Descent (SD) or the Conjugate Gradient (CG) methods.

The common terms used in the computation of local minima are “unrelaxed”, “relaxed” and “optimization”. Where the initial guess or starting position of the system is called the “unrelaxed” configuration. Running an algorithm to find an equilibrium structure is called the “optimisation” process. The output structure of this process it the “relaxed” structure at local minima. All the systems used in this work are optimized by using a conjugate gradient algorithm within the LAMMPS framework (Polak and Ribiere 1969). The minimization processes are carried out with a stopping tolerance force set at $10^{-12} eV/\text{Å}$.

2.2.2 Nudged elastic band approach

The nudged elastic band (NEB) is an efficient static method (Jónsson *et al.* 1998; Henkelman *et al.* 2000), which helps to find the minimum energy path (MEP) between two configurations corresponding to basins in the energy landscape. In this work we will use the NEB method to compute the Peierls potential associated with a glide event (Figure 2.4). For our case with large systems containing dislocations NEB saves computational time and resources in comparison with Hessian based methods. Since initial and final local minima are known in our case, the NEB is computationally efficient to trace the MEP.

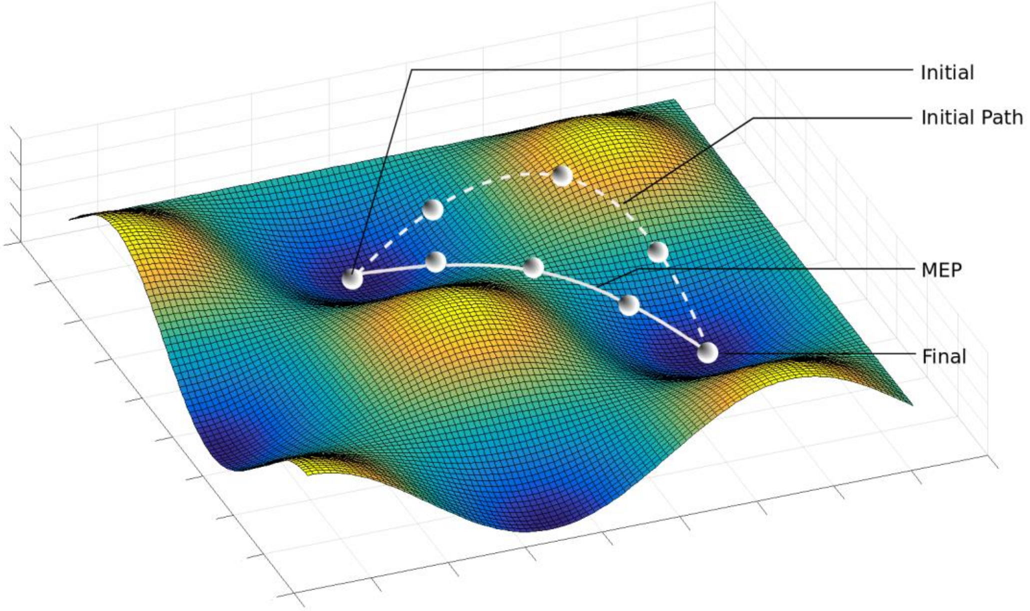

Figure 2.4. *Schematic representation of nudged elastic band calculation. Solid white balls in the 3D energy landscape represent the replicas. The initial and final replicas in the local energy minimum connected with other replicas using springs, the dashed line shows the initial guess and the solid line represents the minimum energy path.*

The calculation of MEP using NEB method involves three major steps (Figure 2.5). Initially a discretised transition path is defined by creating *R* replicas, each replica representing a copy of the whole system. The replicas *1* and *R* are at initial and final local minima. In other words, they can be considered as reactant and product of a reaction respectively. The remaining, intermediate *R-2* replicas contain the process path of the reaction. To prevent the replicas in the middle to move towards local minima during force minimization they are connected to each other using "springs" of unstretched length and spring constant *k*.

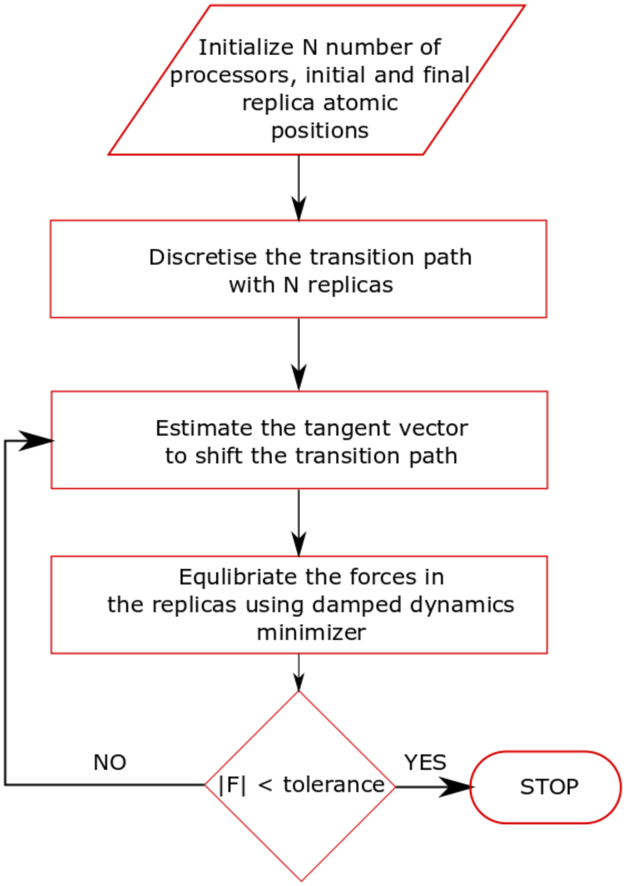

Figure 2.5. *A simple flowchart to describe the shifting of initial guessed transition path towards MEP in a NEB calculation.*

Firstly, the initial guess of the replicas in the reaction path are created using linear interpolation between the reactant and the product. Further, to reduce the force in the system the initial path is moved towards convergence by estimating the tangent vector to the path at each replica. The tangent vectors are determined to ensure better convergence in complex landscapes. Finally, the transition path is optimized by running the algorithm to move the replicas until forces in the system are below an expected force tolerance. The replicas in the middle are not to be moved to local minima (i.e., energy minimized) during optimization, so the default Conjugate gradient or Steepest-descent minimization algorithms cannot be used in this process. In this work we use Quickmin algorithm a damped dynamics based minimization algorithm implemented in LAMMPS (Sheppard 2008).

2.3 Dislocations modelling

All real materials contain defects which may be classified as point, line, surface, and volume defects. These defects significantly alter the theoretical properties of crystalline solids. In this work, we focus on the type of line defect called dislocations which play a major role in the plastic deformation of solids. The concept of dislocation has been independently proposed by Orowan, Polanyi and Taylor in 1934.

The discontinuity associated with a dislocation in a crystal can be well described using an atom to atom path drawn to form a closed loop around the defect, called the Burgers circuit. When the same loop is drawn in a perfect part of the same crystal, the circuit will not close. The closure vector is called the Burgers vector. Based on the Burgers vector direction respective to the dislocation line, dislocations can be classified in to two end-member types as screw and edge dislocations. The Burgers vector is parallel to the dislocation line for screw dislocations and perpendicular to the dislocation line for edge dislocations.

The long-range displacement fields associated with dislocations can be described using continuum mechanics, whereas the elastic theory associated with this method fails near the dislocation core since the dislocation line represents a discontinuity in the displacement field. Hence, atomistic modelling of dislocation cores became an attractive tool to model dislocation cores which is an important component to understand intrinsic dislocations properties in particular lattice friction.

At the atomic scale, one can start from the solution provided by the isotropic elastic theory (Hirth and Lothe 1968) to introduce dislocations in a system. For screw dislocations, as mentioned earlier, the Burgers vector b is parallel to dislocation line ξ (Figure 2.6.a). There are no addition or removal of atoms in the case of screw dislocations, Figure 2.6.b and c shows a typical example for creation of edge dislocation that involves the removal of atoms in a half plane. A displacement is applied to each atom along the z-direction. The magnitude of the displacement increases from zero to b based on the θ value of the displacement u_z given as follows.

$$u_z = \frac{b}{2\pi}\theta = \frac{b}{2\pi}\left[tan^{-1}\left(\frac{y}{x}\right)\right] \tag{2.17}$$

$$u_x = u_y = 0 \tag{2.18}$$

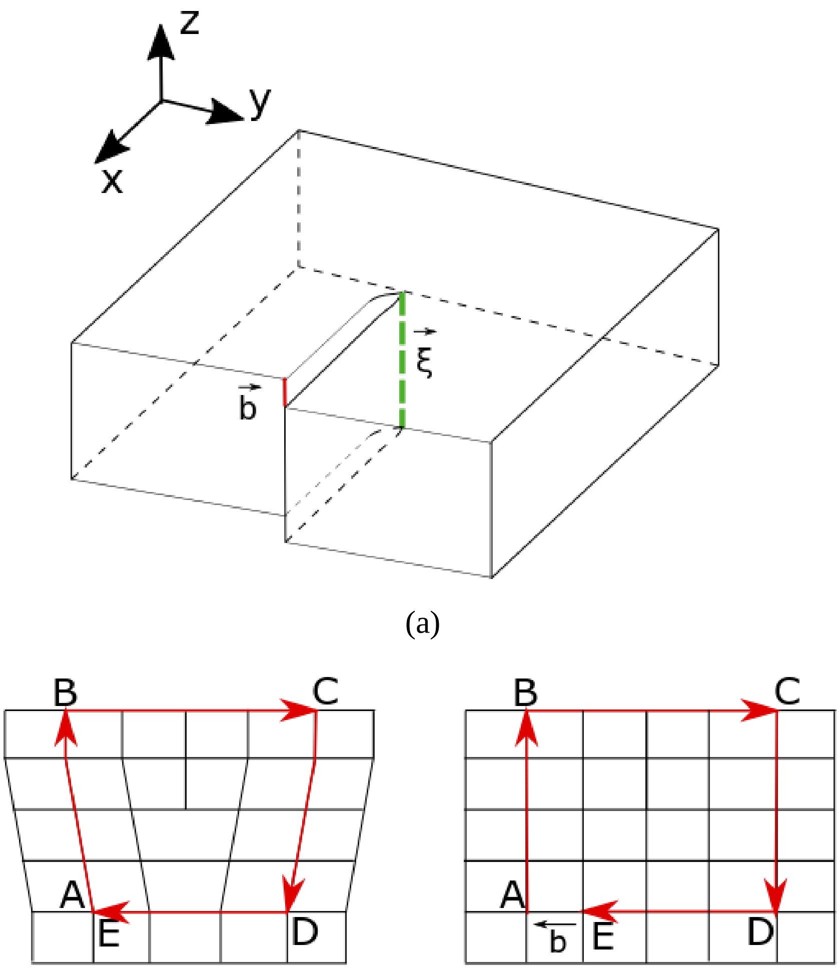

(a)

(b) (c)

Figure 2.6. *(a) A simple screw dislocation in created by "cut and slip" procedure. The slip or Burgers vector and the dislocation line are parallel to each other. (b) A simple cubic system containing edge dislocation represented using a Burgers circuit and (c) the same circuit represented in a perfect crystal.*

In case of an edge dislocation with a dislocation line ξ along the z-direction, the atoms are displaced along the x and y directions. For a material with a Poisson ratio ν, the displacements applied to the atoms are as follows,

$$u_x = \frac{b}{2\pi}\left[tan^{-1}\left(\frac{y}{x}\right) + \frac{xy}{2(1-\upsilon)(x^2+y^2)}\right] \tag{2.19}$$

$$u_y = -\frac{b}{2\pi}\left[tan^{-1}\left(\frac{y}{x}\right) + \frac{xy}{2(1-\upsilon)(x^2+y^2)}\right] \tag{2.20}$$

For simplicity, the isotropic expressions are given, however for the case of materials with lower symmetry in order to find the correct displacement field needed to move an atom from its position in the perfect crystal into its location in the dislocated crystal, we must turn to the anisotropic elastic theory. In general, for the case of more than two independent elastic constants, analytical solutions are not readily available and the displacement field must be found numerically (Steeds and Wills 1979). For a system containing straight dislocation analytical solutions equivalent to (2.18) – (2.20) are given by Steeds (Steeds 1973; Walker *et al.* 2005).

The only advantage of using anisotropic elastic theory to insert a screw dislocation is to have a better starting point for atomic positions far from the dislocation core. Irrespective of the chosen elastic theory, the final dislocation core with anisotropic effects can be obtained after minimization of energy and forces in the system using pairwise potential. Since, the force fields used are intrinsically anisotropic. In this thesis, we limit our discussion to modelling of screw dislocations in forsterite. These displacements are introduced into the atomic system using an open-source program called ATOMSK (Hirel 2015). The ATOMSK code helps to create, modify and analyse the atomic systems.

In case of screw dislocations, the major displacements are along the dislocation line (at least in the elastic theory description). Hence it is hard to visualize a screw dislocation, especially when viewed edge-on. For the purpose of visualizing screw dislocations, we use the differential displacement (DD) maps proposed by Vitek (1968). In this method, the relative displacements of neighbouring atoms due to the dislocation are represented using arrows between them. The magnitude of an arrow is directly proportional to the magnitude of the difference in displacement between the two atoms. The magnitudes of the arrows are larger closer to the dislocation core centres.

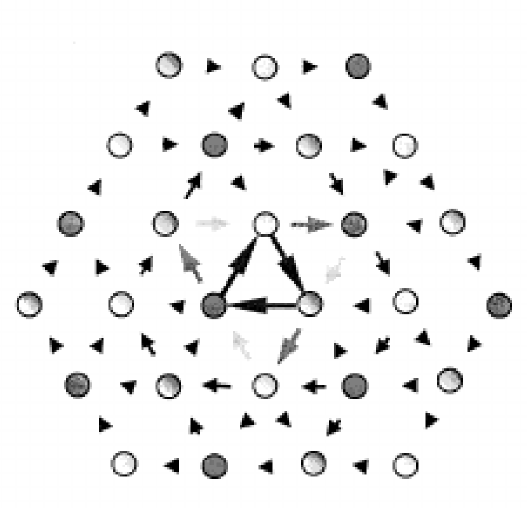

Figure 2.7. *Differential displacement plot of ½<111> screw dislocation core in BCC tantalum single crystal, plotted with respect to the displacement of neighbouring atom in oxygen sub-lattice. This picture is taken from Yang and Moriarty (2006).*

2.4 Atomistic modelling

The basic problem with modelling dislocations using atomistic systems it that these defects have the long range field which cannot be truncated. This drawback can be solved by keeping maximum possible periodicity of the system. Simulations carried out in this work are performed using two types of simulation cells, the quasi-periodic slab type and the fully periodic quadrupole type. Both systems are built with a thickness equal to the Burger’s vector length, to simulate a straight, infinite dislocation line using periodic boundary conditions along the dislocation line.

2.4.1 Slab type system

Hirel *et al.* (2014) proposed a slab type geometry with a quasi-periodic boundary condition explained as follows. The dislocation line is introduced along the z-direction, and the direction of glide along the x-direction. The system is considered to be quasi-periodic since the periodicity is maintained along x and z directions, whereas along the y-direction the atoms at the top and bottom are frozen to replicate an infinite perfect crystal. The frozen zones help to prevent spurious elastic interaction between periodic replicas along y direction. With dislocation of Burgers vector ***b*** in the box, the periodic replicas along the x direction are matched by providing an additional tilt of *b/2* along z as explained in Figure 2.8. The supercell is maintained long enough along the x direction to prevent dislocations interacting with their own periodic replicas, and the frozen zones are maintained far from each other along y direction. To reduce the effect of spurious interaction between periodic replicas, the box dimension is gradually increased to 480 Å and 140 Å along x and y Cartesian directions, respectively.

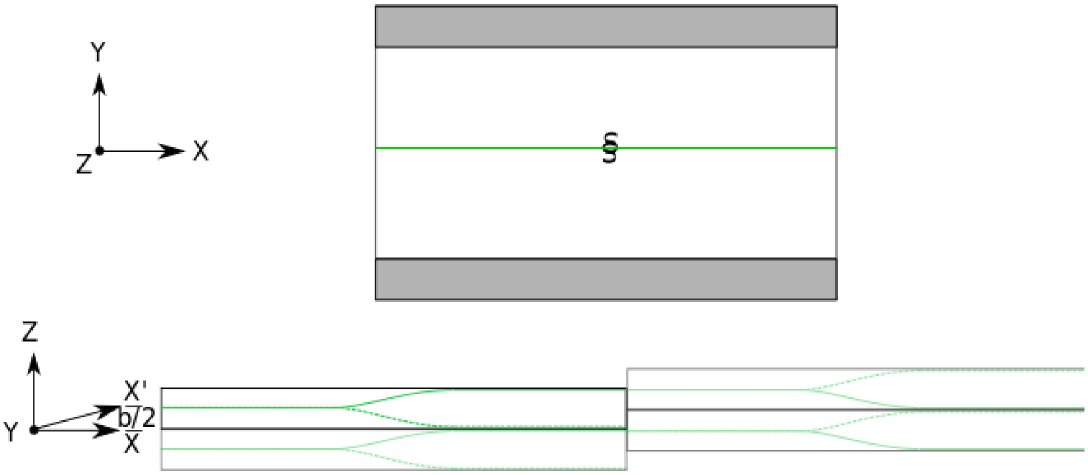

Figure 2.8. *Schematic representation of "Slab" type geometry used in this work. The screw dislocation is introduced along the z Cartesian direction with glide plane along x direction. The b/2 tilt is added to the system to maintain the periodicity along x direction.*

2.4.2 Quadrupole system

For ionic materials like forsterite, it is undesirable to have free surfaces, which can be charged. Hence, the periodic systems are preferred to model dislocations and their properties. The quadrupolar system is created by introducing four screw dislocations with two positive and two negative Burgers vectors along z-direction arranged simultaneously as shown in Figure 2.9. This alternate arrangement of dislocations of opposite Burgers vectors helps to lower the long-range elastic fields of the four dislocations (Lehto *et al.* 1998; Cai *et al.* 2004). This method helps to extract the dislocation core energies, to compute Peierls stresses and the energy barriers. The size effect due to the distance between dislocations can be reduced by increasing the box dimension proportionately along the x and y directions.

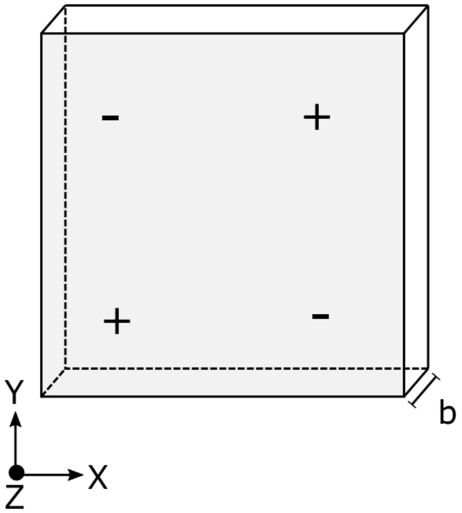

Figure 2.9. *Schematic illustration of a quadrupole simulation cell with two positive and two negative screw dislocation arranged alternatively.*

2.5 Dislocation motion

Plastic deformation of a crystal can result from the motion of dislocations. Here we restrict ourselves to the conservative motion of dislocations in their glide planes. To move a dislocation from one position to another, it has to overcome a potential barrier. In absence of thermal vibrations, the dislocation needs an external stress to overcome the potential barrier. The critical stress required to move a dislocation without assistance of thermal activation is called the Peierls stress. To move a dislocation with a Burgers vector b, the force F acting on the dislocation line ξ due to a local stress field σ can be described using the Peach-Koehler equation.

$$F = (\sigma . b) \times \xi \tag{2.21}$$

Based on the above relation, to trigger motion of a screw dislocation aligned with the z-direction to move along x direction, the system is loaded with ε_{yz} shear strain increments of 1%, ensuring quasi-static loading. After each increment the system is relaxed using a conjugate gradient minimization scheme. As a result, the stress in the system increases linearly. The stress-strain curve deviates from linearity for a critical stress at which the dislocation starts to move, defining the onset of the plastic regime. The critical stress at which the dislocation motion is observed defines the Peierls stress. This calculation is carried out using both simulation cells of quadrupole and slab type geometries. The calculations are repeated with gradual increase in simulation cell sizes along x, y directions to ensure independence with system size effects.

NEB calculations are used to determine the Peierls potential V_P as soon as the MEP is plotted with respect to the good reaction co-ordinate so in this case the dislocation core position. The Peierls potential represents the energy barrier that the dislocation has to overcome to move from one stable position to another. The Peierls stress associated with the motion can be computed from the maximum slope of the energy barrier.

$$\left(\frac{dV_P}{dx}\right)_{max} = b.\sigma_P \tag{2.22}$$

In this work, the NEB calculations are performed using the THB1 pair potential via Quickmin damped dynamics minimization algorithm. The MEP are computed using 15 and 23 replicas which are connected to each other with springs having a spring constant of 0.1 eV/Å. To perform the damped dynamics minimization, shell model simulations are performed using adiabatic dynamics as suggested by Mitchell and Fincham (Mitchell and Fincham 1992). This involves allocating each shell a fraction of mass of its corresponding core and their motions integrated in the same way as that of the core, by integration of classical equations of motion. This method has been tested in simulations of various ionic materials and has been proved successful and computationally efficient (Mitchell and Fincham 1992; de Leeuw and Parker 1998; X.W. Sun *et al.* 2007, Yihui Zhang *et al.* 2009).

3. Implementation and validation of THB1 potential library

In the previous chapter we described the pairwise potential library with core-shell approximation used to model forsterite. In this chapter we will briefly discuss the implementation of a core-shell model potential library to a well parallelised open-source classical molecular mechanics package. After the algorithm for implementation, the energy and force fields implemented are validated by computing bulk properties of forsterite in comparison with first-principle calculations. The THB1 parametrisation is further validated by modeling non-equilibrium properties.

3.1 LAMMPS dependencies

LAMMPS is an acronym for Large-scale Atomic/Molecular Massively Parallel Simulator. LAMMPS is a classical molecular mechanics code (Plimpton 1995), developed at Scandia National Laboratory, a US Department of Energy Facility. It is an open-source code distributed under the GNU/GPL (General Public License). Initially the LAMMPS code was written in Fortran F77 and F90, whereas the present version of LAMMPS are developed in C++ with MPI message-passing library. Well optimized LAMMPS algorithm effectively runs simulations with systems containing few particles to millions. Hence, it can be used for model systems of various applications such as atomic, metallic, biological, granular and coarse-grained structures with the help of a variety of force fields and boundary conditions.

To model dislocation core and its mobility with systems having few thousands of particles, a well parallelised and optimized code is necessary. We choose LAMMPS, because it is faster for large systems in comparison to the existing codes containing core-shell models (for instance GULP (Gale 1997)), thanks to effective neighbour list implemented in LAMMPS (Thompson *et al.* 2009; Plimpton and Thompson 2012) and the flexibility for developers to extend.

The LAMMPS source code has been divided into various classes and the data are passed between them using pointers. The backbone of LAMMPS is constructed on a dozen of top-level class, which are visible throughout the code (for example the atomic co-ordinates from Atom class). Next to these are a set of virtual parent classes, which LAMMPS defines as "*style*". The *style* classes contain the parameters and constraints that are imposed during a simulation. Each parent class holds a list of child classes, which the developers are expected to contribute to increase the capability of LAMMPS. In this work the THB1 potential library is implemented as a child class under a parent class called "Pair style". The layers of the LAMMPS code and their different classes are illustrated in Figure 3.1.

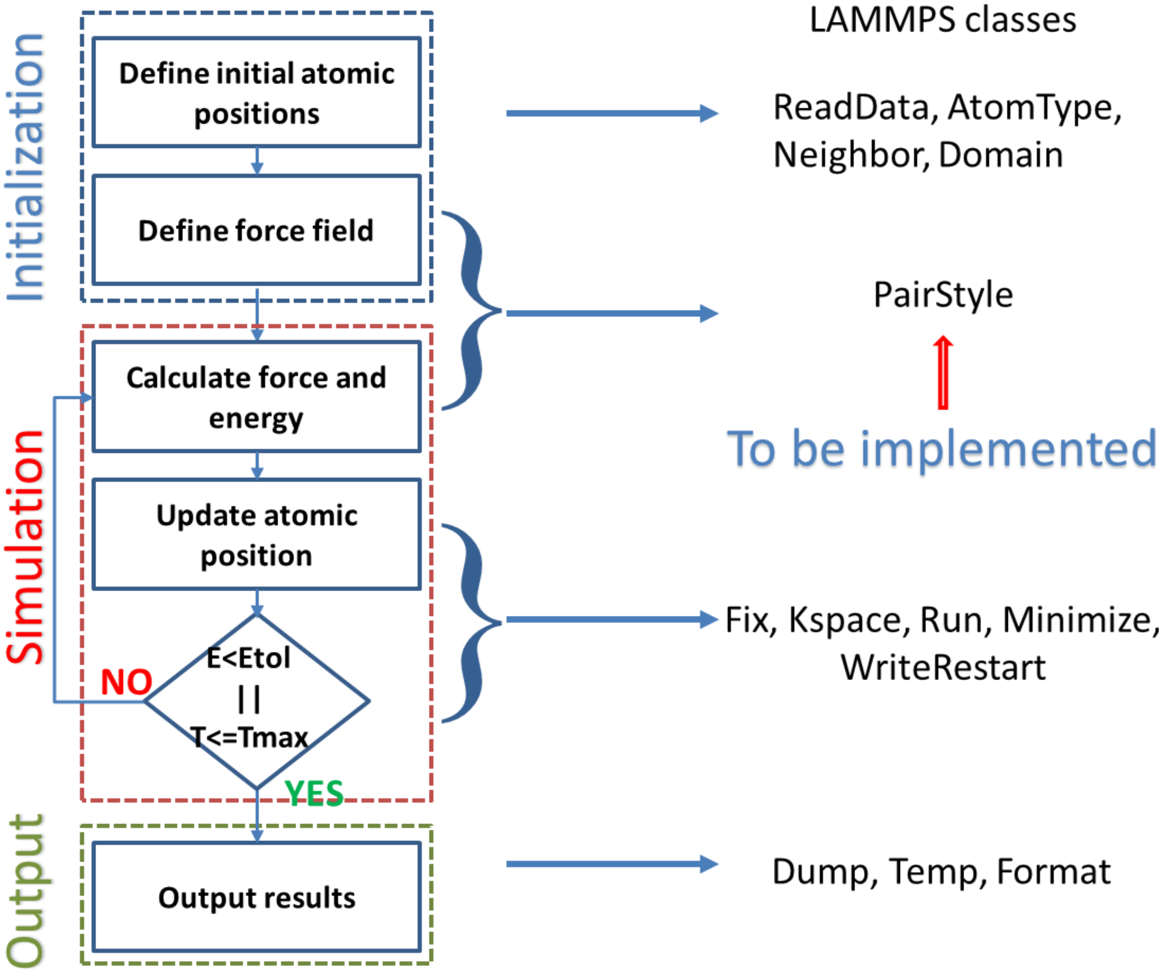

Figure 3.1. *Flowchart representation of structure of LAMMPS and classes in LAMMPS.*

3.2 Force fields

This section explains about the implementation of core-shell library of inter-atomic potentials and their corresponding analytical forces into LAMMPS code. LAMMPS is designed in such a way to allow users to develop new potentials as class Pair styles without disturbing the core of the source code. The THB1 potential library consists of an electrostatic term, a short-range Buckingham potential, a harmonic spring term and a three-body term. The expressions required for calculating force fields acting on every ion can be calculated from the negative gradient of the potential energy in equation (2.10). In summary, the force is calculated as,

$$f = -\nabla U_{Total} \tag{3.1}$$

The force field of ions from Columbic interaction is computed using the Wolf summation method (Wolf *et al.* 1999), it is a spherically truncated, charge-neutralized pair potential which makes a $1/r$ summation. A cautious implementation of a self-energy term is carried out, to ensure that q_{ion} is the total charge of ion (i.e., charge of core and shell are not separately added to the self-energy term). The first derivative calculation for the electrostatic term is well discussed by Wolf *et al.* (1999). In summary, the final form of the electrostatic force term implemented is as follows,

$$f_{Coulomb\ \alpha} = \sum_{\substack{j\neq i \\ (r_{ij}<R_c)}} q_i q_j \left\{ \begin{array}{c} \left(\frac{erfc(\alpha R_c)}{r_{ij}^2} + \frac{2\alpha}{\pi^{1/2}} \frac{exp\left(-\alpha^2 r_{ij}^2\right)}{r_{ij}}\right) \times \frac{r_{ij\alpha}}{r_{ij}} \\ -\left(\frac{erfc(\alpha R_c)}{R_c^2} + \frac{2\alpha}{\pi^{1/2}} \frac{exp(-\alpha^2 R_c^2)}{R_c}\right) \times \frac{r_{ij\alpha}}{R_c}\bigg|_{r_{ij}=R_c} \end{array} \right\} \tag{3.2}$$

Forces from short-range pair interaction between shells separated by a distance less than a user-defined cut-off of R_B, is described by first derivative of two-body Buckingham potential U_{Short} from equation (2.12) is as follows,

$$f_{Short\ \alpha} = \left(-6C_{ij}r_{ij}^{-6} + \frac{A_{ij}}{B_{ij}} exp\left(-\frac{r_{ij}}{B_{ij}}\right) \times r_{ij}\right) \times \frac{r_{ij\alpha}}{r_{ij}^2}\ , r_{ij} < R_B \tag{3.3}$$

The attraction force between the core and its corresponding shell is provided by the first derivative of the harmonic spring term with respect to the distance of separation between them r_i, and the maximum distance between a core and its shell is given by a spring cut off term R_{spring}.

$$f_{spring\ \alpha} = -\left(K_1 + \frac{K_2 r_i^2}{6}\right) r_{i\alpha}\ , r_i < R_{spring} \tag{3.4}$$

The force field from the covalent three-body term on ion *i* due to its neighbours *j* and *k* are given as a set of expressions as follows.

$$f_{THB\ i\alpha} = -f_{THB\ j\alpha} - f_{THB\ k\alpha} \tag{3.5}$$

$$f_{THB\ j\alpha} = A_{11} r_{ij\alpha} + A_{12} r_{ik\alpha} \tag{3.6}$$

$$f_{THB\ k\alpha} = A_{22} r_{ik\alpha} + A_{12} r_{ij\alpha} \tag{3.7}$$

where,

$$\varDelta\theta = k_{ijk}^{B} \cdot \left(\theta_{ijk} - \theta_0\right) \tag{3.8}$$

$$A = -2\,\varDelta\theta \sin\theta_{ijk} \tag{3.9}$$

$$A_{11} = \frac{A\cos\theta_{ijk}}{r_{ij}^2} \tag{3.10}$$

$$A_{12} = \frac{A}{\left(r_{ij} \times r_{ik}\right)} \tag{3.11}$$

$$A_{22} = \frac{A\cos\theta_{ijk}}{r_{ik}^2} \tag{3.12}$$

3.3 Command description

The execution in LAMMPS is by reading of an input script. The input script contains a collection of required predefined keywords. Each keyword has a syntax which makes LAMMPS to define an internal variable or to perform a task. The “pair_style” command contains a library of formulas that LAMMPS uses to compute pairwise interactions. The coefficients associated with the pair style to model an interaction between a pair of atoms are specified using “pair_coeff” command. The THB1 potential library has been implemented as a module under the “pair_style” class, respecting the constraints imposed in the parent code. Table 3.1 shows the “pair_style” command used in an input script with the THB1 parameters from Table 2.1. Figure 3.2 illustrates the algorithm of implementation of the THB1 potential library with help of a flow chart.

Table 3.1. *Commands to cause LAMMPS to call core/shell sub-class implemented to model forsterite with THB1 parametrisation. The Mg, Si, O core and O shell are represented as atom types 1, 2, 3, 4 in the sample set of commands, which can be modified based on user preference.*

THB1 Pair style arguments

# Class	Style	Si type	k_{ijk}^{B}	θ_o (radian)	α	Formal charge for ions				R_B	R_C
						1	2	3	4		
pair_style	core/shell	2	2.09	1.910612	0.2	2.0	4.0	-2.0	0.0	12	16

Coefficients of potential

# Command	Atom type		A_{ij}	B_{ij}	C_{ij}	K_1	K_2	R_{Spring}	R_{THB}
	i	j							
pair_coeff	1	4	1428.5	0.2945	0.0	0.0	0.0	0.0	0.0
pair_coeff	2	4	1283.9	0.3205	10.66	0.0	0.0	0.0	2.0
pair_coeff	4	4	22764.3	0.1490	27.88	0.0	0.0	0.0	3.0
pair_coeff	1	2	0.0	1.0	0.0	0.0	0.0	0.0	0.0
pair_coeff	1	1	0.0	1.0	0.0	0.0	0.0	0.0	0.0
pair_coeff	2	2	0.0	1.0	0.0	0.0	0.0	0.0	0.0
pair_coeff	1	3	0.0	1.0	0.0	0.0	0.0	0.0	0.0
pair_coeff	2	3	0.0	1.0	0.0	0.0	0.0	0.0	0.0
pair_coeff	3	3	0.0	1.0	0.0	0.0	0.0	0.0	0.0
pair_coeff	3	4	0.0	1.0	0.0	74.92	0.0	0.5	0.0

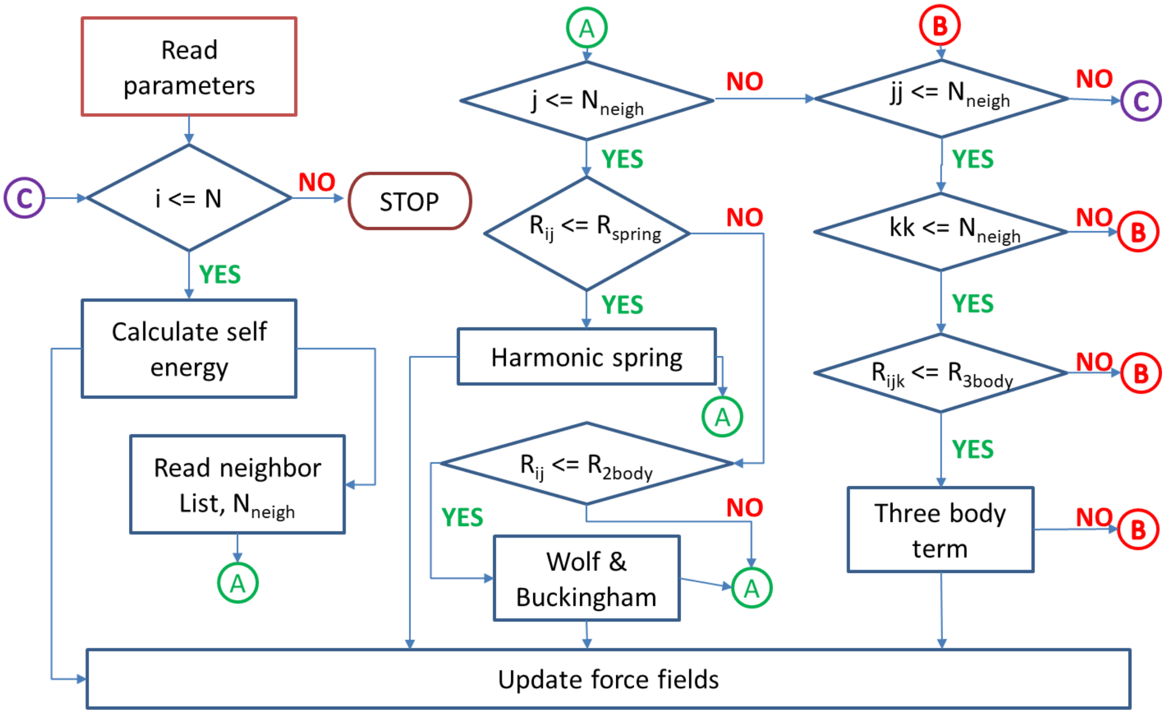

Figure 3.2. *Algorithm of THB1 potential library implemented in LAMMPS as a sub-class under the main class Pairstyle.*

3.4 Validation of THB1 potential

3.4.1 Lattice constants

The evolution of the lattice constants of forsterite as a function of pressure is computed as primary test of validation. The lattice constants are optimised for an isostatic pressure ranging from 0 to 10 GPa. The optimisation is achieved by applying an external pressure to the simulation box during energy minimisation. During the iteration of the minimiser the shape and size of the simulation box are allowed to vary, to attain a final configuration that is energy minimised and the system pressure tensor is close to the specified external pressure tensor. The orthorhombic symmetry of forsterite is preserved during the minimisation process.

Table 3.2. *Evolution of lattice constant as function of pressure. The lattice constants and volume of unit cell computed using THB1 semi-empirical potential is compared with the values estimated using DFT calculations (given within parenthesis) by Durinck et al. (2005a).*

Pressure (GPa)	a (Å)	b (Å)	c (Å)	V (Å^3)
0	4.7874	10.2717	6.0227	296.1646
	(4.7932)	(10.2807)	(6.0408)	(297.6752)
5	4.7274	10.1345	5.9483	284.9820
	(4.7467)	(10.1243)	(5.9511)	(285.9921)
10	4.7009	9.9928	5.8994	277.1252
	(4.7148)	(9.9799)	(5.8807)	(276.7059)

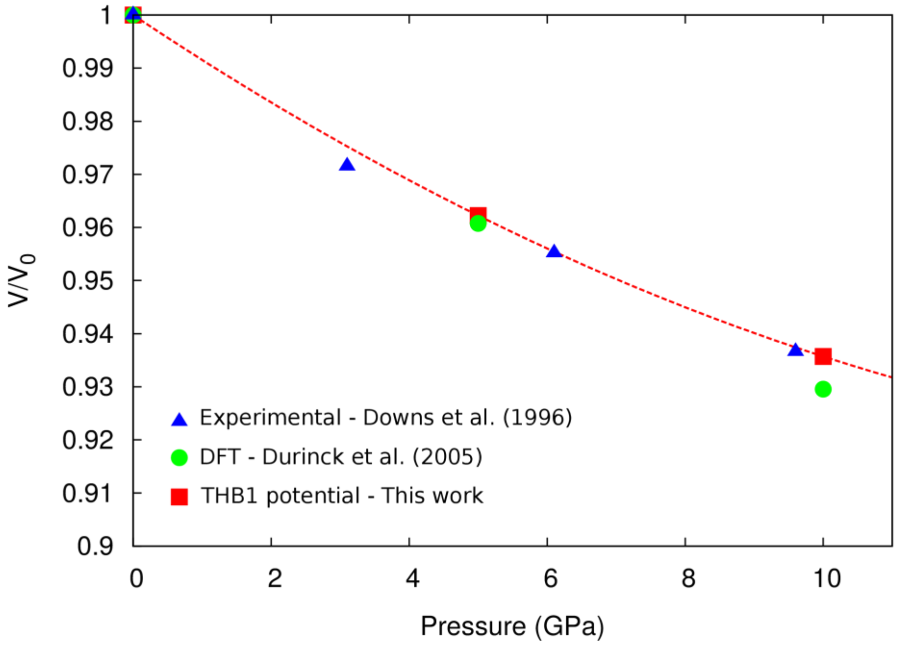

Figure 3.3. *The compression data from the experiment performed on forsterite (Downs et al. 1996) is well reproduced by the calculations performed using THB1semi-emprical potential parameterisation. The calculated volume are well fitted with the Birch-Murnaghan equation of state* $V(P) = V_0\left(1 + K_0'\left({}^{P}/_{K_0}\right)\right)^{-1/K_0'}$*, where* V_0*,* K_0*,* K_0' *are the equilibrium volume, Bulk modulus and pressure derivative of bulk modulus respectively (fit plotted as dashed lines).*

The lattice constants computed at different isostatic pressure values are reproduced in Table 3.2 in comparison with the DTF result (Durinck *et al.* 2005). Figure 3.3 shows a comparison of our results with the first-principles calculations and experimental results from literature. From Table 3.2 it is clear that all the lattice parameters are in good agreement with the DFT values to a deviation less than 0.4 %. The cells are constructed for pressure between 0 to 10 GPa using the same procedure. This initial verification gives the confidence to perform calculations under pressure using this THB1 potential parametrisation.

3.4.2 Elastic constants

The elastic response of a crystal to an applied load is described by Hooke's law:

$$\bar{\bar{\sigma}} = \bar{\bar{\bar{\bar{C}}}}\bar{\bar{\varepsilon}} \text{ or } \sigma_{ij} = C_{ijkl}\varepsilon_{kl} \tag{3.13}$$

Where $\bar{\bar{\sigma}}$ is the stress tensor, $\bar{\bar{\varepsilon}}$ is the strain tensor and $\bar{\bar{\bar{\bar{C}}}}$ is the elasticity tensor. In Voigt's notation, the fourth rank elasticity tensor $\bar{\bar{\bar{\bar{C}}}}$ can be replaced by a 6x6 elastic tensor matrix $[C_{ij}]$. An anisotropic material has a maximum of 21 non-zero elastic components C_{ij} (depending on the symmetry while in an isotropic crystal the number of independent components reduces to 2). In a crystal with orthorhombic symmetry like forsterite, 9 independent elastic constants (C_{11}, C_{22}, C_{33}, C_{44}, C_{55}, C_{66}, C_{12}, C_{13} and C_{23}) must be taken into account.

Computing elastic constants of a solid is important because they are directly linked to interatomic potentials. They can be written as the second derivatives of the potential energy of a system with volume V, as follows:

$$C_{ijkl} = \frac{1}{V}\left[\frac{\partial^2 U_{Total}}{\partial \varepsilon_{ij}\varepsilon_{kl}}\right] \tag{3.14}$$

This expression can be simplified using Voigt notation,

$$C_{ij} = \frac{1}{V}\left[\frac{\partial^2 U_{Total}}{\partial e_i \partial e_j}\right] \tag{3.15}$$

With a 3x3 strain tensor matrix

$$\varepsilon = \begin{pmatrix} e_1 & \frac{1}{2}e_6 & \frac{1}{2}e_5 \\ \frac{1}{2}e_6 & e_2 & \frac{1}{2}e_4 \\ \frac{1}{2}e_5 & \frac{1}{2}e_4 & e_3 \end{pmatrix} \tag{3.16}$$

To calculate nine elastic constants for an orthorhombic crystal, nine independent applied strains must be considered. They are presented in Table 3.3. (Beckstein *et al.* 2001). So to compute each elastic constant, we strained the equilibrium cell with an adapted deformation at constant pressure. The applied stains are of magnitudes between -2 % to 2 %. In those strained configurations the atoms are allowed to relax their positions to minimize energy using a conjugate gradient algorithm with a stopping tolerance for force set at 10^{-12} eV/Å (1.602×10^{-21} N). As a test of validation of force fields implemented with Wolf summation long-range term, our results of elastic constants are compared with an existing implementation of the THB1 potential library with Ewald long-range term in GULP code (Gale 1997). Based crystal symmetry it is also possible to run strain patterns of e1+e4, e2+e5 and e3+e6 as the stresses don't mix for these pairs of strains.

The elastic constants computed are listed in Table 3.4. From the results, it is clear that irrespective of the long-range summation technique (Wolf or Ewald), the elastic constants are in perfect agreement with a difference of less than 1%. The elastic constants calculated for systems at 0, 5 and 10 GPa of pressure are compared with DFT results (Durinck *et al.* 2005) in Table 3.5. In comparison with the first-principle calculations, all diagonal elements C_{11}, C_{22} and C_{33} are 20 % stiffer. Components C_{44} and C_{55} of the elastic matrix are 45 % and 5 % softer respectively. As in many cases elastic constants computed using empirical potential does not exactly reproduce the first-principles values, but they correspond to the best compromise for forsterite (Price and Parker 1987).

Table 3.3. *Parametrisation of nine strains used to compute nine independent elastic constants of orthorhombic forsterite crystal.*

Strain	Parameters (unlisted e$_i$ = 0)	$\frac{\Delta E}{V}$
1	$e_1 = \gamma$	$\frac{1}{2}C_{11}\gamma^2$
2	$e_2 = \gamma$	$\frac{1}{2}C_{22}\gamma^2$
3	$e_3 = \gamma$	$\frac{1}{2}C_{33}\gamma^2$
4	$e_1 = 2\gamma, e_2 = -\gamma, e_3 = -\gamma$	$\frac{1}{2}(4C_{11} - 4C_{12} - 4C_{13} + C_{22} + 2C_{23} + C_{33})\gamma^2$
5	$e_1 = -\gamma, e_2 = 2\gamma, e_3 = -\gamma$	$\frac{1}{2}(C_{11} - 4C_{12} + 2C_{13} + 4C_{22} - 4C_{23} + C_{33})\gamma^2$
6	$e_1 = -\gamma, e_2 = -\gamma, e_3 = 2\gamma$	$\frac{1}{2}(C_{11} + 2C_{12} - 4C_{13} + C_{22} - 4C_{23} + 4C_{33})\gamma^2$
7	$e_4 = \gamma$	$\frac{1}{2}C_{44}\gamma^2$
8	$e_5 = \gamma$	$\frac{1}{2}C_{55}\gamma^2$
9	$e_6 = \gamma$	$\frac{1}{2}C_{66}\gamma^2$

Table 3.4. *Elastic constants C_{ij} (in GPa) computed at 0 GPa using either Wolf summation (implementation of this work in LAMMPS) or Ewald summation (Gale 1997). The DFT results performed by Durinck et al. (2005) are provided for comparison to the THB1 results.*

	C_{11}	C_{22}	C_{33}	C_{44}	C_{55}	C_{66}	C_{12}	C_{13}	C_{23}
Using Wolf summation	344.4	200.9	279.2	36.1	75.9	82.2	88.2	92.4	87.8
Using Ewald summation	344.9	201.7	279.4	37.0	76.1	81.7	88.5	92.3	88.5
DFT	300.7	195.7	224.1	65.8	78.3	77.3	61.1	62.3	64.7

Table 3.5. *Comparison of elastic moduli (in GPa) as a function of pressure. The THB1 results computed in this work are compared with the DFT results performed by Durinck et al. (2005).*

Pressure (GPa)	0		5		10	
	THB1	DFT	THB1	DFT	THB1	DFT
C_{11}	344.4	300.7	367.5	332.8	389.7	375.5
C_{22}	200.9	195.7	221.0	215.8	235.2	231.7
C_{33}	279.2	224.1	308.3	242.1	330.9	277.1
C_{44}	36.1	65.8	51.8	73.6	61.3	82.9
C_{55}	75.9	78.3	83.4	86.7	87.8	94.1
C_{66}	82.2	77.3	95.2	85.8	103.3	97.6
C_{12}	88.2	61.1	110.5	83.0	127.8	95.3
C_{13}	92.4	62.2	109.8	79.5	123.3	96.0
C_{23}	87.8	64.7	221.0	85.1	235.2	97.7

3.4.3 Generalised stacking fault energy

Being able to reproduce the elastic properties satisfactorily is a first validation. It is however not sufficient to model dislocations since in the core, atomic positions which may differ significantly from equilibrium positions are to be expected (breakdown of linear elasticity). To further validate our implementation with a view to perform crystal defect calculations using THB1 potential library we calculate generalized stacking fault (GSF) energy surfaces as introduced by Vitek (1968). The GSF (or the γ-surface) energy can be computed by cutting a perfect crystal along a given crystallographic plane followed by a rigid body shear. The GSF energy in combination with continuum model of dislocation provides information on nature of dislocation (Durinck *et al.* 2007; Carrez *et at.* 2015). This GSF energy computation has been proved to be an effective approach for minerals with complex crystal structure to extract fundamental characteristics of the structure of dislocations (Gouriet *et al.* 2014; Goryaeva *et al.* 2015).

A fully periodic system is used to calculate the excess energies associated with GSF. The super cells constructed of lattice vectors a_x, a_y and a_z, the stacking plane of interest is oriented normal to z Cartesian direction (Figure 3.4). The excess energies of GSF are calculated for [100] slip on (010), (001) and {021} planes and for [001] slip on (100),

(010) and {110} planes. For {021} and {110}, the GSF calculations are performed using monoclinic cells. Stacking faults are introduced to the system by shearing the upper block of the supercell and then the system is allowed to minimize. Crystal chemistry plays an important role in determining the cutting plane level. Shearing the Si-O bonds results in higher stacking fault energies. The planes containing magnesium atoms are more preferable to introduce stacking faults than planes containing atoms belonging to SiO_4 tetrahedra. An optimum size (~100 Å) of supercell is maintained along z Cartesian direction, long enough for the atoms close to the slip plane to relax, without causing any atomic distortion near the periodic boundary. Care has been taken to study the effect of atomic relaxations on energy barrier heights in 1D GSF energy calculations. Two types of relaxations schemes are compared in this work. In the first case (Case 1), one allows the atoms to relax normal to the plane of shear. In the second case (Case 2), as proposed by Durinck *et al.* (2005a), the Mg and O atoms are allowed to relax freely in every direction whereas the Si atoms are constrained to relax normal to the fault plane to preserve the SiO_4 tetrahedra.

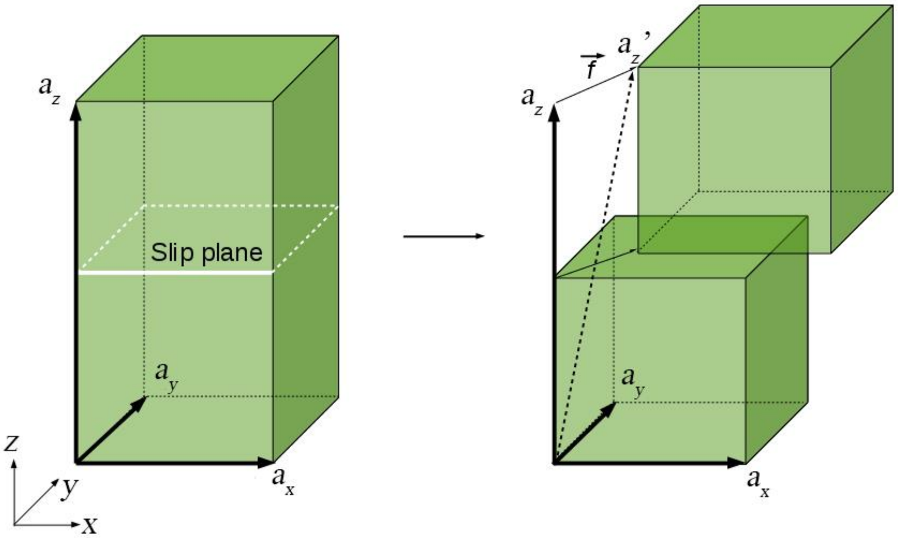

Figure 3.4. *Schematic representation of 2D γ-surface calculation. The lattice vector* a_z *is given an additional component* $\vec{f}$ *corresponding to the applied shear, to maintain the 3D periodicity of the system. The periodicity is maintained to avoid any charged free surfaces containing ions*

Further to determine the excess energies of the γ-surface, rigid body shear parallel to the shear plane is applied to the upper block of the structure with respect to the lower block. The displacement applied to the system is of magnitude $\vec{f} = e_x\vec{a}_x + e_y\vec{a}_y$. 400 data points were calculated for each slip plane with 5 % increment of each displacement. The lattice vector a_z is tilted along $\vec{f}$ to maintain periodicity of the system. After the displacement atoms are allowed to relax along z Cartesian direction, at constant volume minimization condition.

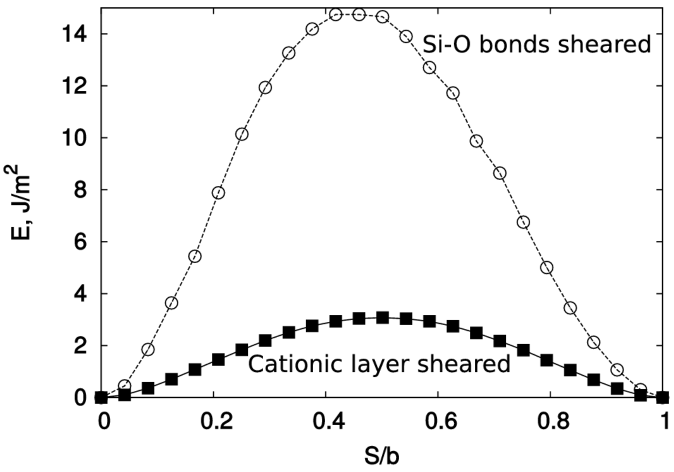

Figure 3.5. *Generalised stacking fault energy barriers computed for [100] rigid shear in (010) plane. Two different energy barriers corresponds to the shearing of different layers.*

The GSF gives the height of the energy barrier associated with the rigid shear along the selected slip plane. First step is to validate the hypothesis that shear in silicates occur whenever possible along cationic layers rather than the layers containing Si-O bonds. Figure 3.5 shows that the [100] shear along (010) requires less energy to shear along layers containing Mg atoms than shearing Si-O bonds. This also validates the efficiency of our three-body term to describe the covalency within SiO_4 tetrahedra. Hence, care has been taken in this work to ensure that shearing of Si-O bonds is avoided during GSF energy calculations (Figure 3.6). For [001] slip in (100) a corrugated surface is used to create a fault plane (Figure 3.7).

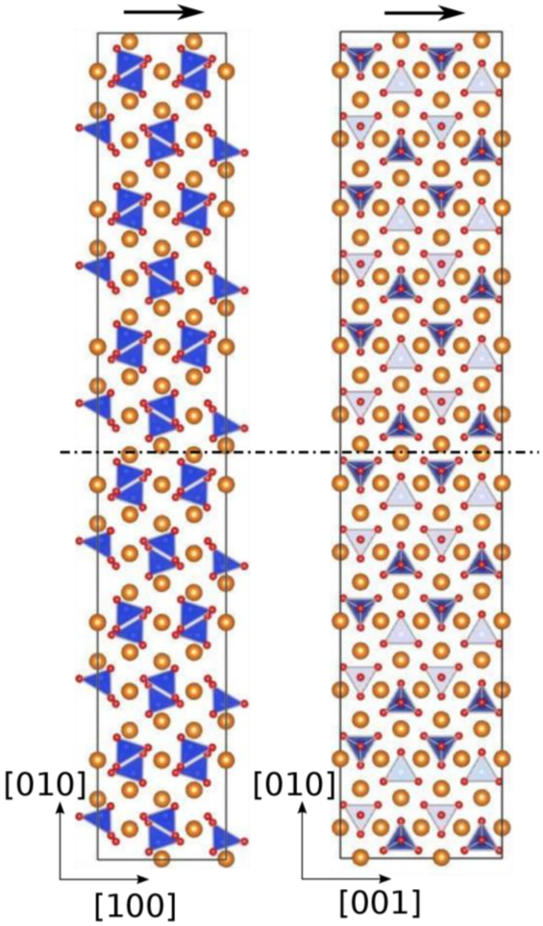

Figure 3.6. *Unsheared supercell used to calculate (010) stacking fault (where O and Mg ions are represented as red and yellow balls respectively and Si ions, trapped in the centre of the tetrahedron, are represented as small blue balls). The upper part of the supercell is moved with respect to the lower one. In this case, the fault vector is along [100] or [001] and the fault plane does not break Si-O bonds*

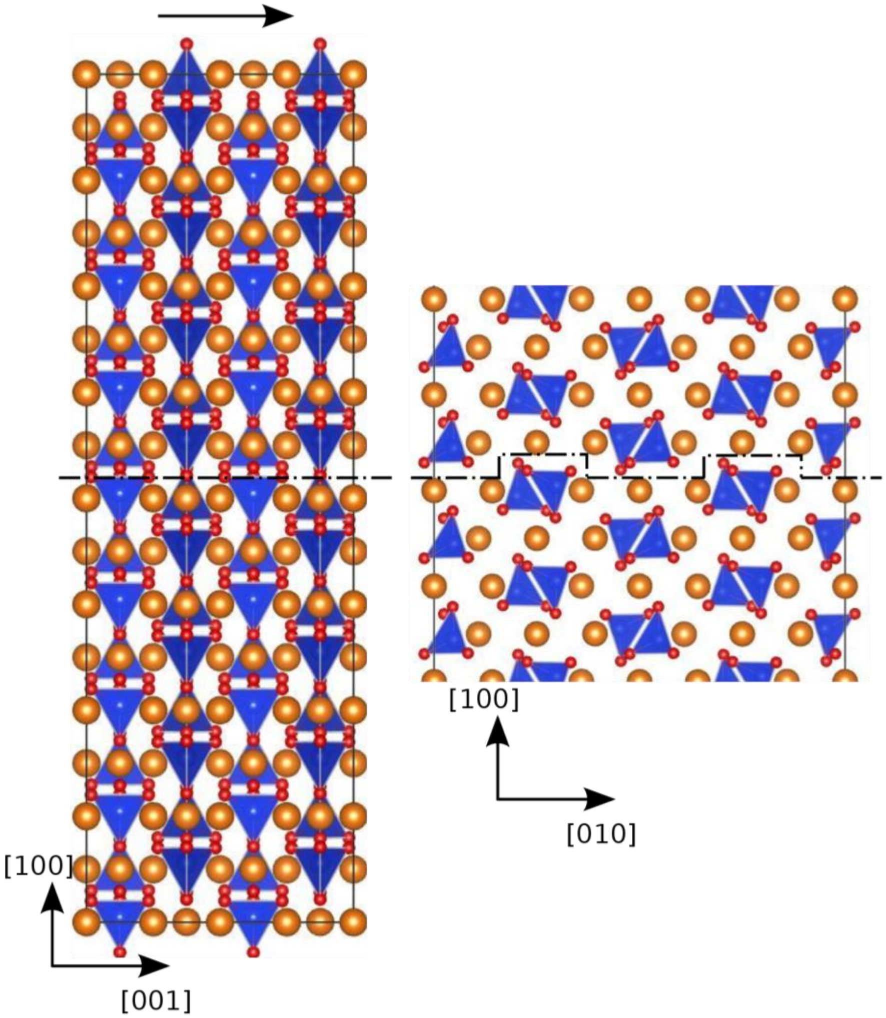

Figure 3.7. *Unsheared supercell used to calculate (100) stacking fault by [001] shear is given in the left. To prevent the shearing of Si-O bond in the fault plane a corrugated surface is used shown in the right.*

The γ-surfaces s for (100), (010) and (001) planes are calculated using Case 1 minimisation scheme (Figure 3.8). Calculation of shear along [010] in (100) is restricted to approximately 15 % (Figure 3.8.c), The maximum energy observed in the middle of the γ-surface is a result of oxygen atoms of different tetrahedra that comes close to each other during rigid shear. The observation of maximum energy values for [010] slip in (001) shows that [010] dislocation is highly unfavourable.

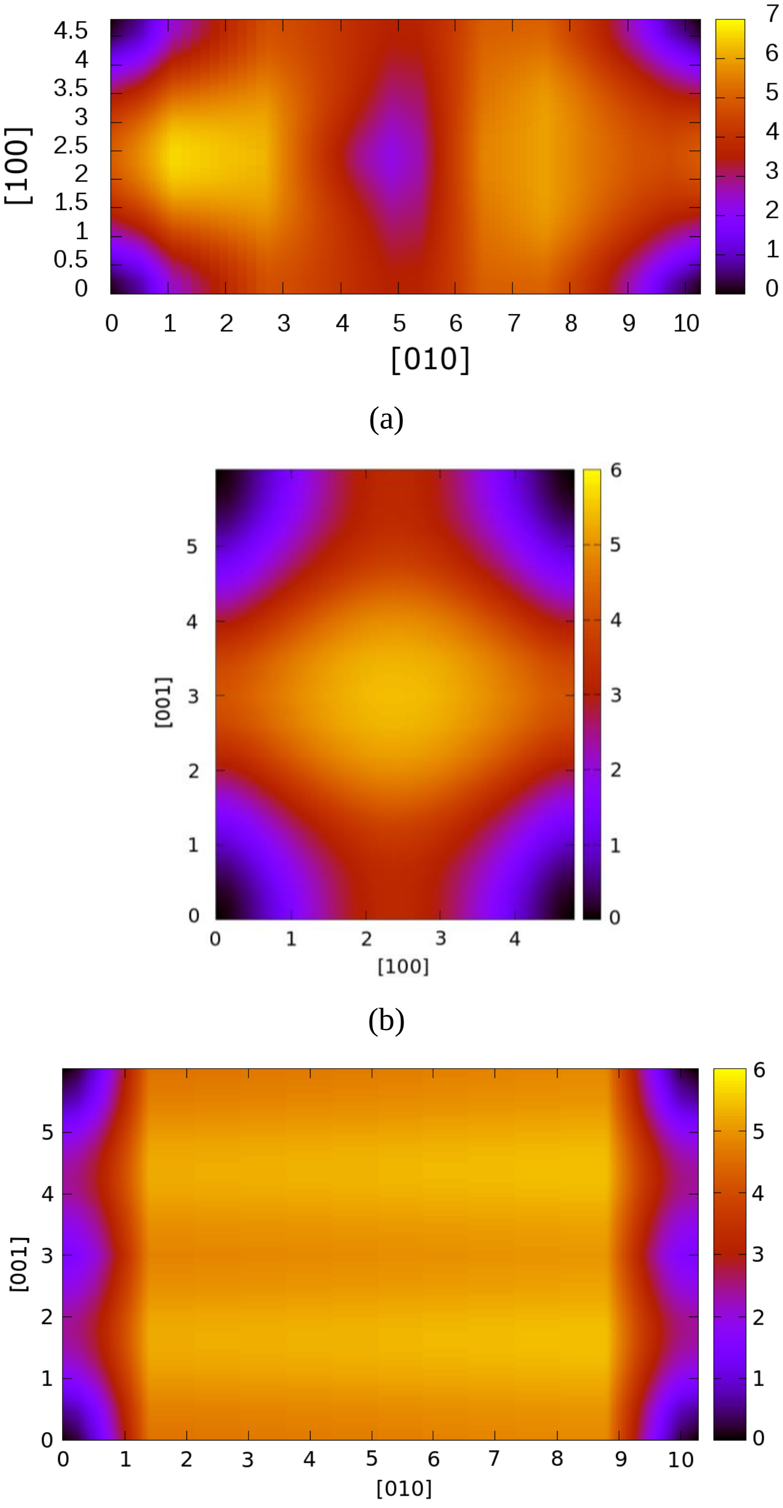

(a)

(b)

(c)

Figure 3.8. *2D γ-surface (in J/m^2) computed using THB1 potential library associated with shearing of two layers located above and below the slip plane. The planes considered are (a) (001), (b) (010), and (c) (100).*

For highly symmetric crystals with simple chemical compositions, the relaxation during GSF calculations have been traditionally restricted normal to the fault plane (Garvik *et al.* 2014). In contrary additional degrees of freedom has to be allowed for forsterite due to complex crystal chemistry (Durinck *et al.* 2005a). In the Case 2 relaxation scheme, Mg and O are allowed to relax freely in all direction, this enables the SiO_4 tetrahedra to tilt/deform during relaxation. We observe in Figure 3.9 the importance of this relaxation technique through significant reduction of barrier heights in comparison to the regular relaxation scheme (Case 1).

The Case 2 relaxation scheme helps to reduce the barrier height yielding results closer to the first-principles calculations performed by Durinck *et al.* (2005a). The increase in degrees of freedom helps relax to lower energy values, but a less smooth GSF curve is expected (Figure 3.9). Case 1 regular relaxation scheme predicts slightly higher stacking fault energies due to insufficient relaxation of atomic positions. The increased barrier height is the drawback of semi-empirical potential parameters usage whereas they conserve the shape of the energy barriers for both stable and unstable GSF curves. With suitable relaxation conditions, for [100] shear in (010), (001) and {021} exhibit similar intrinsic resistance as predicted by earlier DFT calculations. Further, other than the [001](010) shear, the [001] shear exhibit lower barrier heights compared to [100] shear. Though the energy barrier comparison is not an accurate measurement of the plastic properties, shearing the forsterite structure along [001] seems intrinsically easier than along [100], which is in agreement with low temperature plasticity data (Phakey *et al.* 1972, Gaboriaud *et al.* 1982, Gaboriaud 1986). Thus, THB1 potential library parameters and the implementation are validated to explain the shear properties of forsterite.

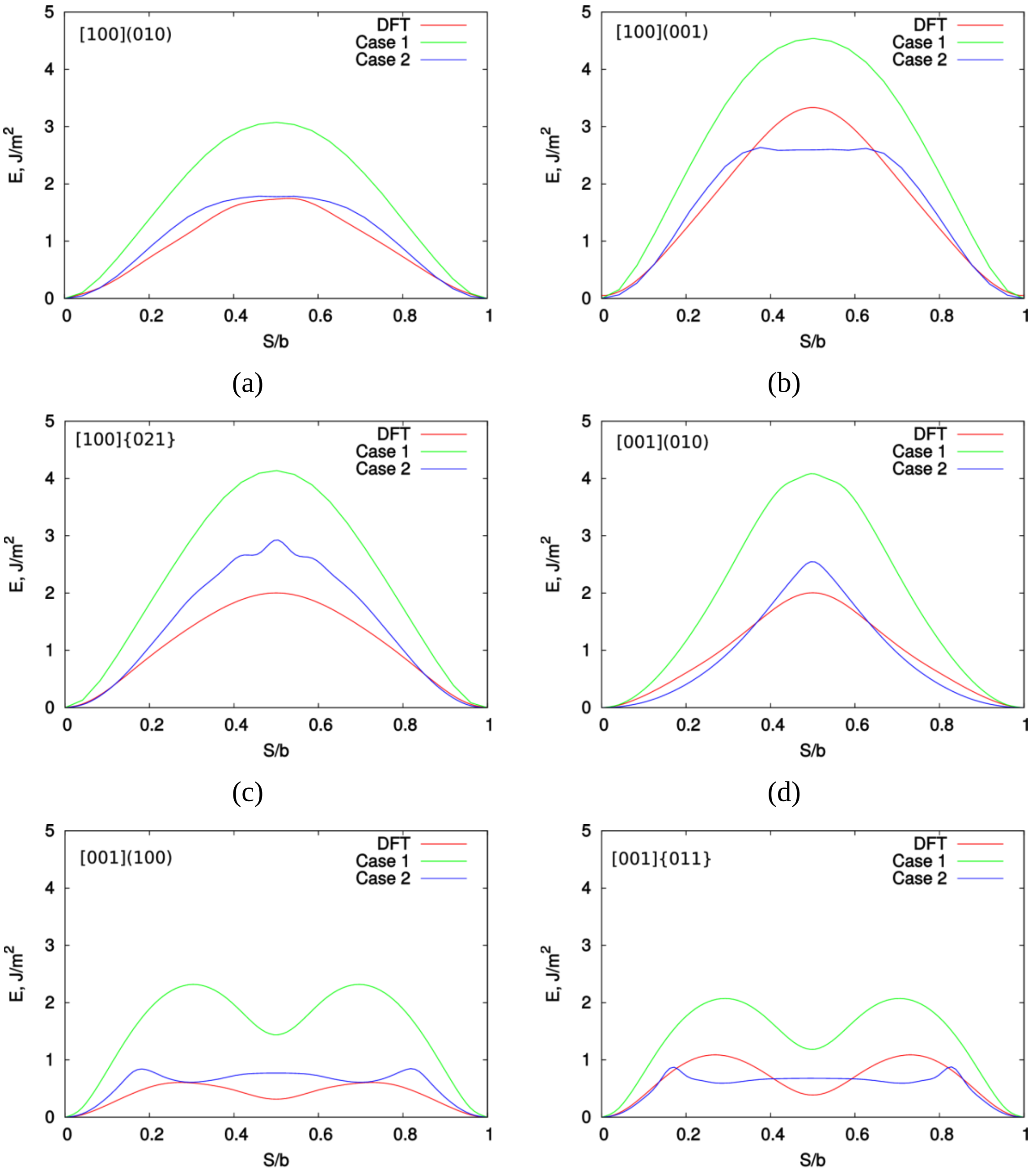

(a) (b)

(c) (d)

(e) (f)

Figure 3.9. *Generalised stacking fault energy barriers computed in this work using THB1 potential library is compared with results of first principal calculation performed in earlier works (Durinck et al. 2005a). Case 1 represents the results from the minimization of atoms normal to the fault plane and Case 2 represents the relaxation scheme given by Durinck et al. (2005a), i.e. Mg and O atoms can relax freely in all directions whereas Si is constrained to relax only normal to the fault plane.*

3.5 Summary

The structure of the LAMMPS open-source molecular mechanics package is studied to understand the architecture of the code. Further the core-shell potential library is implemented to the software as an auxiliary module. The values of energy and the force fields implemented with Wolf summation electrostatic term to the module are compared with the exiting core-shell implementation with traditional Ewald summation term. Further the THB1 pair-potential parameters are validated by comparison of results from this work with existing first-principle results from literature (Durinck *et al.* 2005a). The results are found to be in good agreement. The elastic-constant tensor validates for a system in equilibrium and the second derivative of the potential energy terms implemented. For validating the parameters of THB1 for systems far from equilibrium, like system containing dislocations, the theoretical generalized stacking faults are computed. The 1D and 2D γ-surfaces results are calculated using THB1 parameters. The pair-potential from our implementation has well reproduced the shape of the stacking-fault curves. However, similar to the case of elastic constants the values of stacking fault energies are slightly higher than the DFT results.

4. [100] Screw dislocations

This chapter deals with the theoretical modelling of dislocation core and slip system activities involving dislocations with [100] Burgers vector. The atomic systems are developed to analyse the dislocation core structure and to estimate lattice friction associated with different slip systems in the absence of thermal activation. The spreading of [100] dislocation cores and lattice friction are analysed at 0 GPa. Further, the effect of pressure (up to 10 GPa) on the dislocation core stability and mobility are investigated with the support of NEB calculations.

4.1 Screw dislocation cores at 0 GPa

4.1.1 Dislocation core structures

The atomic systems used are designed to study dislocation core properties, and how they can glide in different planes. The simulations were performed using periodic systems, described in section (2.4.1). After the optimisation procedure, the dislocation core structures are analysed using differential displacement maps (Vítek 1968) and atomic disregistries. The spreading of the core in each plane is represented using a disregistry function S(r) by plotting the disregistries parallel to the dislocation line as a function of distance from the core. To plot the disregistry function along x-axis, we use an analytical solution as a sum of arctan written as follows,

$$S(x) = \frac{b}{2} + \frac{b}{\pi}\sum_{i}^{N} \alpha_i tan^{-1}(\frac{x - x_i}{\zeta_i}) \tag{4.1}$$

Where b corresponds to the dislocation Burgers vector (i.e. [100] magnitude in this chapter), x_i and ζ_i correspond to the position of the fractional density *i* of the Burgers vector, and its half width respectively. In any case, the sum of α_i is equal to one. The first derivative dS/dx, gives the density of Burgers vector from which one can define the width of the total dislocation core. In case of dissociated core, the distance between Burgers vector density peaks gives at first order the distance of separation between partial or fractional dislocations.

Figure 4.1 shows the differential displacements map around the core of a [100] screw dislocation. Based on neighbours' cations analysis, the core of the [100] screw dislocation shows a clear tendency of spreading in (010) with a core centre located between SiO_4 tetrahedra at the M2 site (we used the classical distinction M1, M2 of cation sites in olivine group structure; Deer *et al.* 1982). To be quantitative, the spreading of the core is investigated by extraction of the disregistry functions within (010) from the atomic positions. Dissociation of the core into two strongly correlated Burgers vector density peaks is observed. The distance between these peaks, approximately 7 Å (Table 4.1), is close to one lattice parameter along the [001] direction.

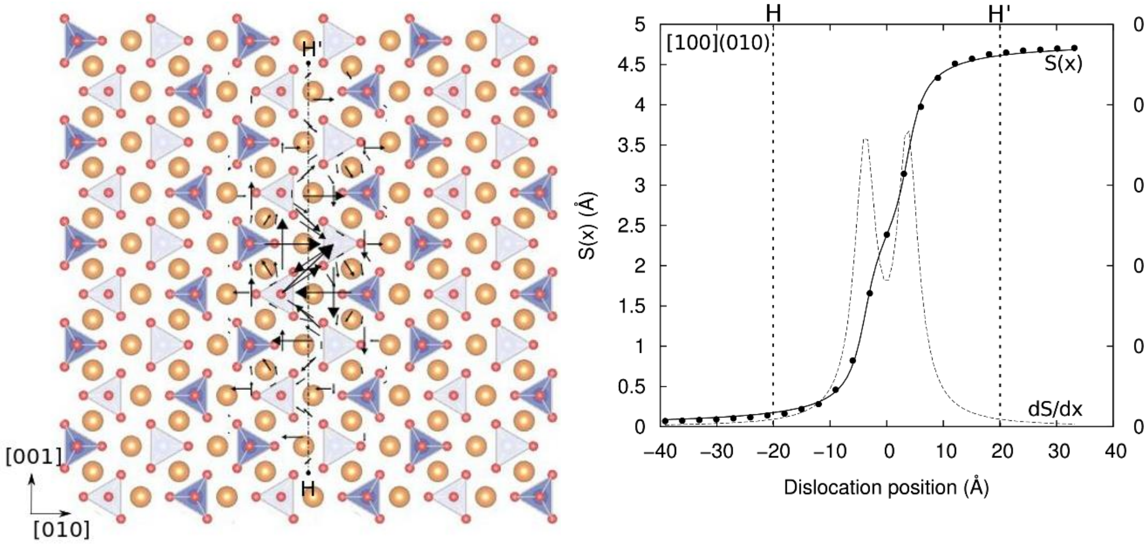

(a) (b)

Figure 4.1. *Screw dislocation core with [100] Burgers vector at 0 GPa (a) Atomic configuration of [100] screw dislocation core viewed along the line direction; the yellow, blue and red balls represent the Mg, Si and O ions and the* SiO_4 *tetrahedra; the arrows represent the differential displacement between the neighbouring ions along [100] dislocation line; (b) Corresponding disregistry S(x) and the density of [100] burgers vector dS/dx for the cationic sub-lattice. The two distinct peaks show dissociation of the core.*

Details of the atomic arrangements around the line indicate that the core of [100] dislocations involves some local edge displacements in the vicinity of (010). These local displacements do not produce any edge component of the dislocation Burgers vector but can be associated with a dilation state of the core. Following Sun *et al*. (2016), an atomistic-to-continuum cross over method is used to analyse the details of local non-screw displacements. The unrelaxed and relaxed configurations obtained during the atomistic calculations are used as the reference state and deformed state, respectively. The components of the displacement vector field, ***u***, in the vicinity of the dislocation core are calculated for the three different sub-lattices. However, since the compact anionic sub-lattice ensures continuity of the structure, only displacements corresponding to the oxygen sub-lattice are shown in what follows. The displacement vector field maps (Figure 4.2) clearly indicate that the edge components are restricted to the vicinity of (010), and correspond to outward displacements of atoms. Thus, from the computed gradient of the displacement vector, u, one can compute the corresponding strain tensor giving access to the local dilatation taken as the trace of the strain tensor. As shown in Figure 4.3, positive values for the trace of the strain tensor around the core validates the dilatation of the dislocation core.

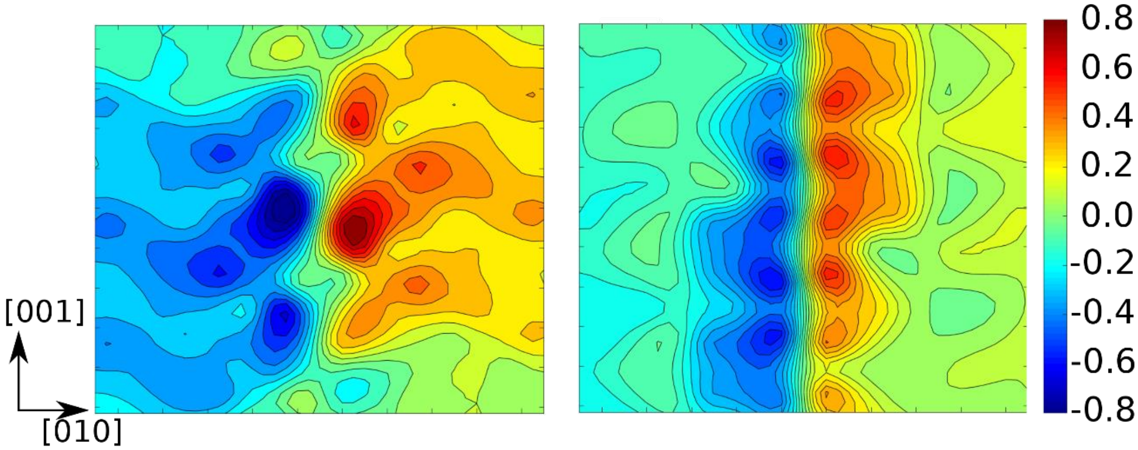

(a) (b)

Figure 4.2. *Representation of edge displacement field (in Å) around the [100] dislocation core calculated using O sub-lattice at 0 GPa. Continuum displacement fields along (a) the [010] direction and (b) the [001] direction.*

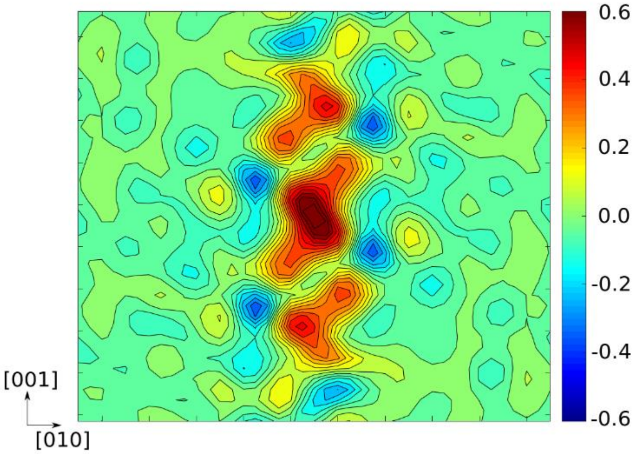

Figure 4.3. *Trace of the strain tensor around [100] screw dislocation core calculated in the O sub-lattice. The positive value for the trace of strain tensor quantify the dilatation of the dislocation core.*

4.1.2. Lattice friction

At 0 GPa, Figure 4.1 shows that the core of [100] dislocations is dissociated with spreading in (010) plane. So to study glide in (010), we computed the energy barrier associated with glide using NEB calculations. The Peierls potential in Figure 4.4.a shows a barrier with a metastable core in the middle. From disregistry of the metastable core, it turns out that the intermediate core becomes narrower and does not show any evidence of dissociation, while it is still spread in (010) (Figure 4.5.). To validate the existence of a metastable core, the NEB calculation for glide in (010) is repeated between two metastable cores separated by a distance of one lattice parameter along [001]. The result shows that the camel hump shape of the barrier is preserved (Figure 4.4.b), with the stable dissociated core observed in the middle.

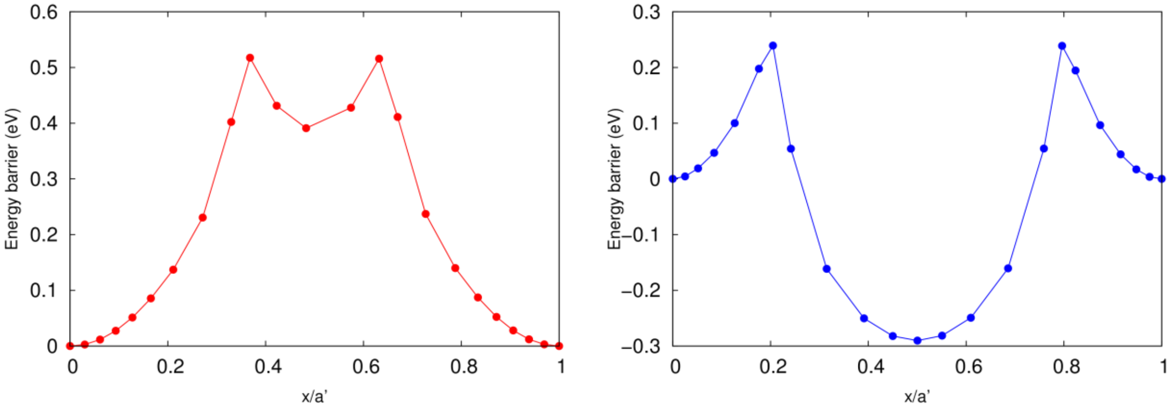

(a) (b)

Figure 4.4. *The Peierls potential as a function of dislocation centres associated with the (010) glide [100] screw dislocation at 0 GPa. The NEB calculation performed between (a) two dissociated dislocation cores spread in (010), (b) two non-dissociated metastable dislocation cores spread in (010).*

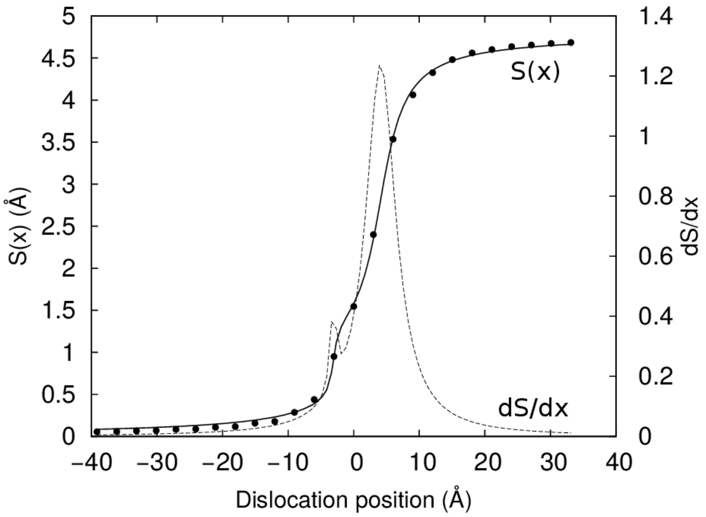

Figure 4.5. *Metastable [100] screw dislocation core observed at 0 GPa. The density of dislocation dS/dx does not show any evidence of dissociation.*

The presence of metastable core raises the question of a possible dependence of the Peierls potential on the applied stress. To address this issue, we use the same setup than for the previous NEB calculations and we add a constant strain component. The fixed stain component added is such that it induces a stress which promotes glide in (010). From the Peierls potential (Figure 4.6), the maximum slope of $V_P(x)$ is extracted and plotted it as a function of the applied stress in Figure 4.7. The result shows that irrespective of the starting configuration of the dislocation, it starts to glide in (010) at a threshold stress of 2.45 GPa.

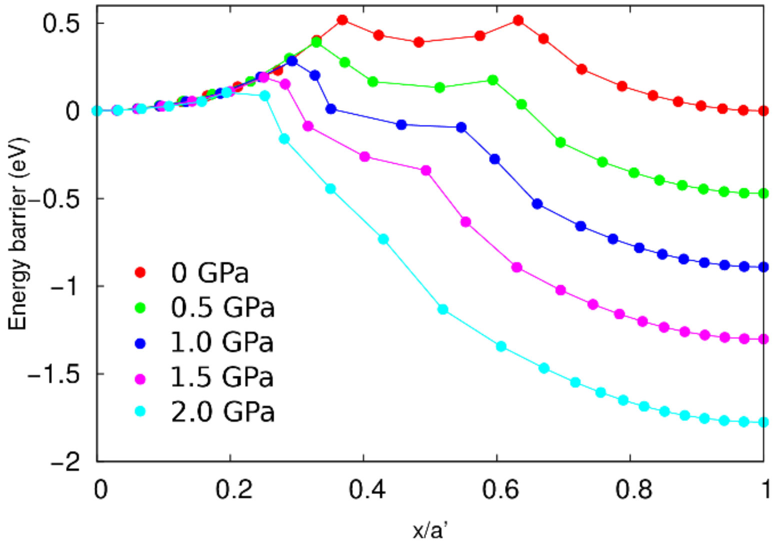

(a)

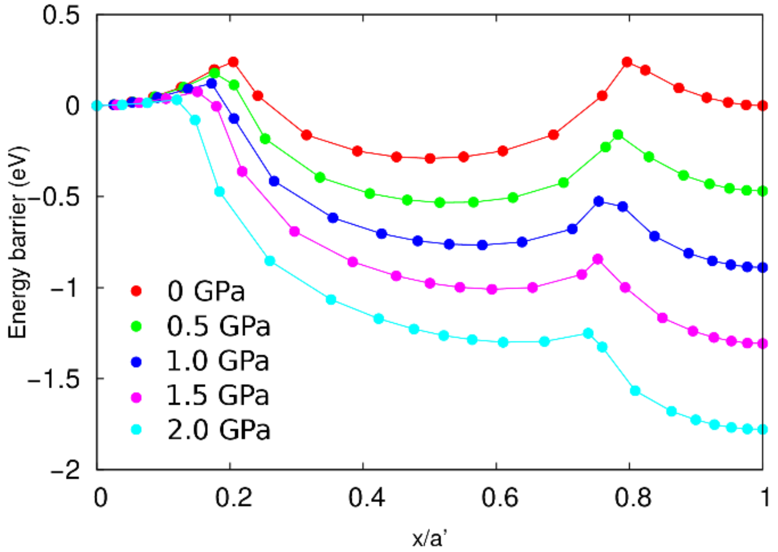

(b)

Figure 4.6. *Minimum energy path plotted for straight screw dislocation with [100] Burgers vector plotted as a funtion of applied stress from 0 – 2.0 GPa at an isostatic pressure condition of 0 GPa. For (a) a dissociated stable core spread in (010) plane and (b) an non-dissociated metastable core spread in (010) plane.*

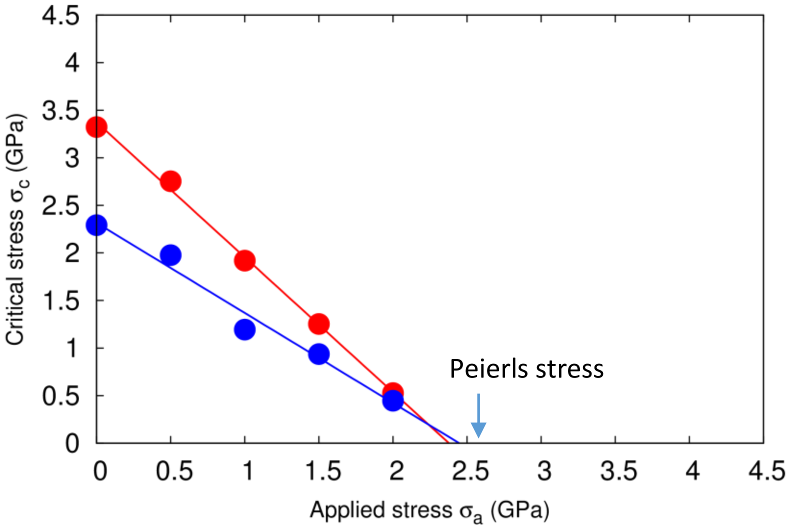

Figure 4.7. *Maximum slope of the MEP plotted against the applied shear stress during the NEB calculation for [100] screw dislocation glide in (010) at 0 GPa. The maximum slope corresponding to the dissociated stable core and non-dissociated metastable core are given in red and blue respectively.*

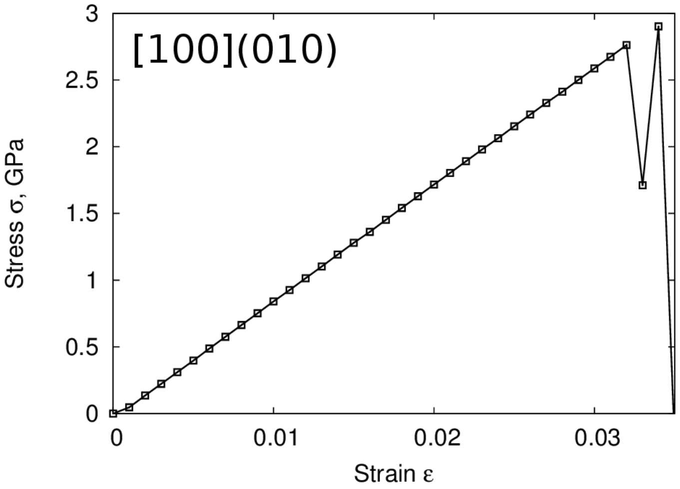

Figure 4.8. *Calculation of the Peierls stress for a [100] dislocation gliding in (010) plane by quasi-static loading. The linear trend represents the elastic response of the cell to the applied load. The critical stress above which the dislocation move corresponds to the stress drop on the plot.*

As mentioned in the methods section (Chapter 2, Section 2.5), a simple shear is applied to the stable core to determine at which critical stress the dislocation starts to move in a given glide plane. Two different critical stresses for glide in (010) and (001) are computed. For [100](010), the computed Peierls stress is 2.76 GPa (Figure 4.8). This value of Peierls stress is slightly higher than the value derived from the Peierls potential, but they are in good agreement with each other. The quasi static loading gives a good proxy of the Peierls stress. In contrast, when the [100] dislocation is forced to glide into (001), a higher value of the Peierls stress around 7 GPa is found.

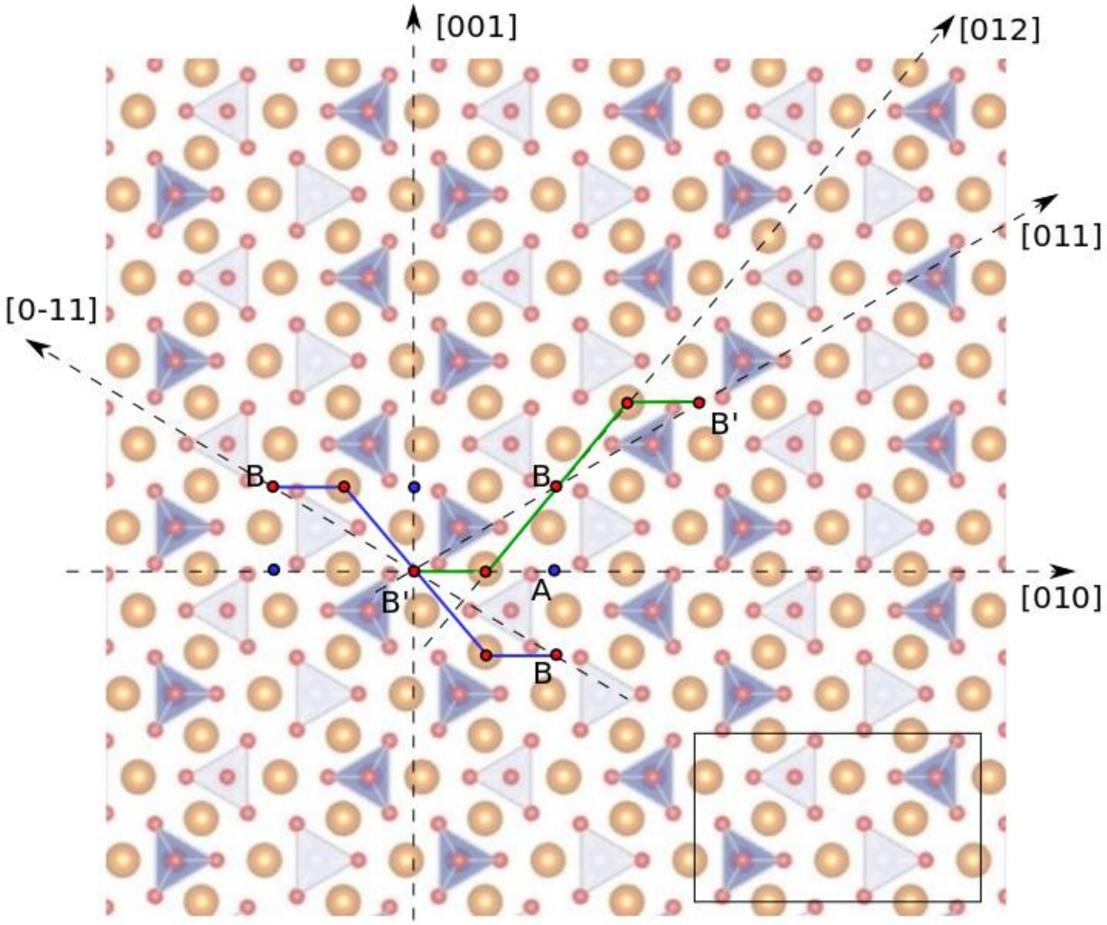

Figure 4.9. *Super cell of forsterite (Mg_2SiO_4) crystal viewed along the [100] direction. The unit cell is shown in the lower right corner. The proposed dislocation core centres for [100] screw dislocations are labelled A, B and B'. The green and blue paths correspond to the minimum energy path computed for dislocation glide in {011}.*

4.2 Effect of pressure on dislocation core

4.2.1 Low pressure core configuration

For pressures below 4 GPa, the [100] screw dislocations are fully spread in (010). A typical dislocation core configuration at 2 GPa is shown in Figure. 4.10. The analysis of the atomic disregistry across (010) reveals a tendency for planar dissociation with two fractional dislocations strongly overlapping. This is consistent with calculations performed at 0 GPa of isostatic pressure showing that [100] dislocation dissociates in (010) into two partials dislocation of 1/2[100] Burgers vector. Nevertheless, with increasing pressure, this dissociated state becomes metastable as confirmed by NEB calculations aiming to investigate the glide mechanism in (010) (Figure 4.12).

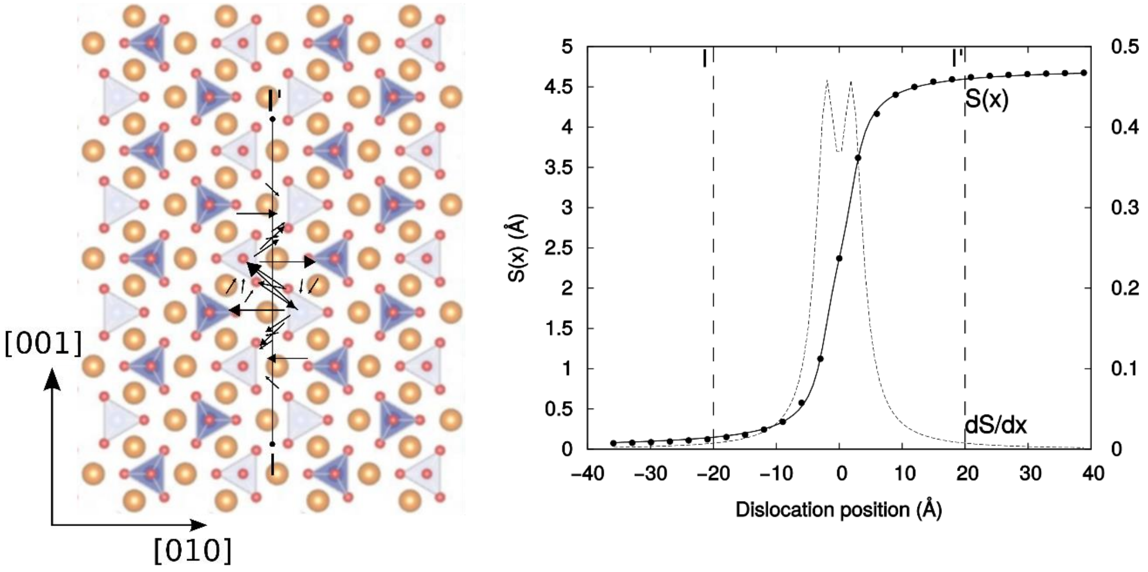

(a) (b)

Figure 4.10. *Screw dislocation core with [100] Burgers vector at 2 GPa (a) Atomic configuration of [100] screw dislocation core viewed along the line direction; the yellow, blue and red balls represent the Mg, Si and O ions and the SiO_4 tetrahedra ; the arrows represent the differential displacement between the neighbours along [100] dislocation line; the arrows show a clear planar spreading of the core in (010) plane (b) Corresponding disregistry S(x) and the density of [100] burgers vector dS/dx for the cationic sub-lattice. The peaks of the density of [100] dislocation are not distinct to show any evidence of dissociation.*

The difference in core energy between stable and metastable configurations are below 0.1 eV/Å. The non-screw displacements around the non-dissociated core spread in (010) are analysed and the corresponding displacement fields and the trace of the strain matrix for the oxygen sub-lattice are plotted in Figure 4.11. The positive values of the trace of the strain tensor shows that the stable core at 2 – 4 GPa is dilated.

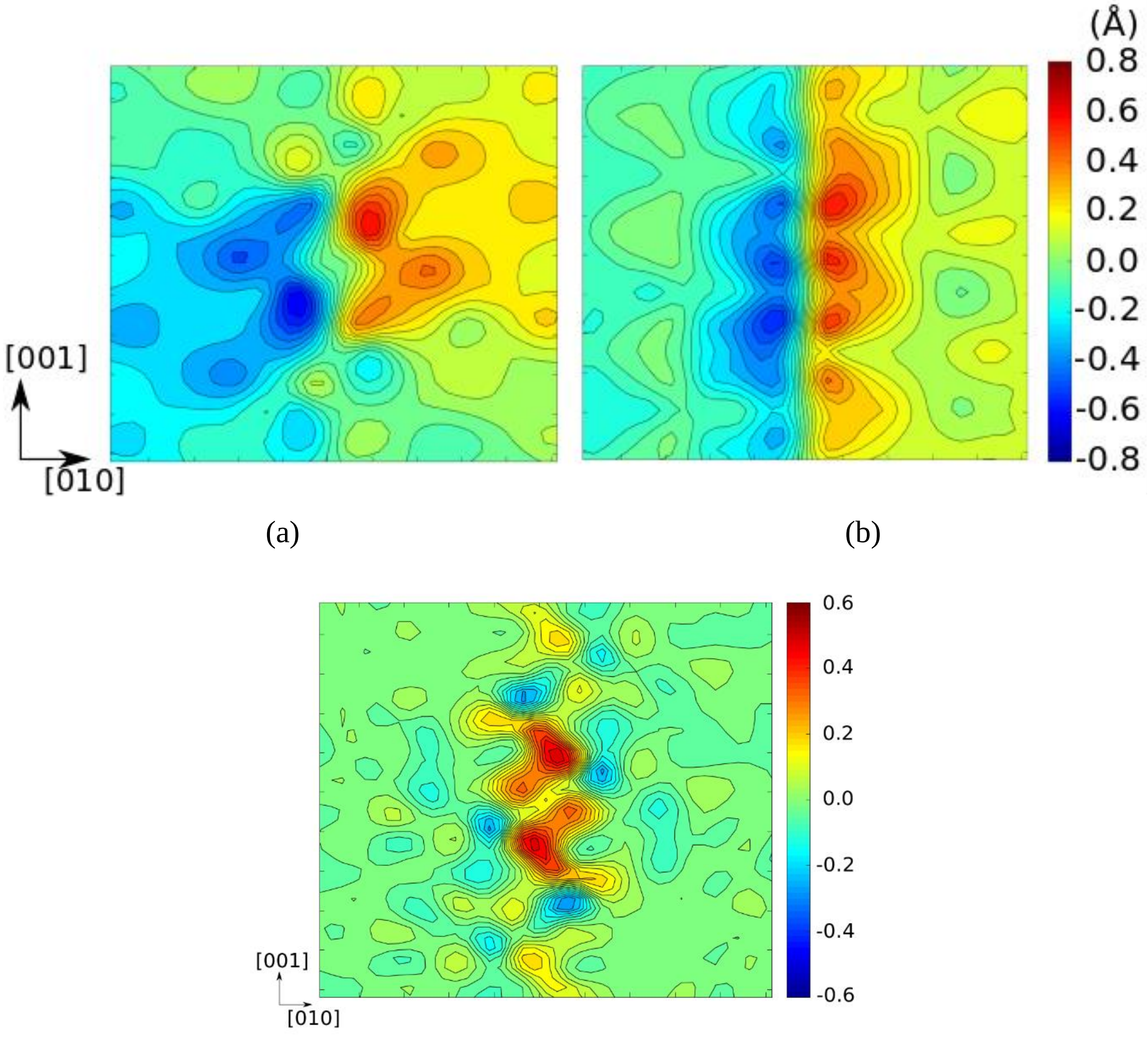

(a) (b)

(c)

Figure 4.11. *Representation of edge displacement field around the [100] dislocation core calculated using O sub-lattice at 2 GPa. Continuum displacement fields (in Å) along (a) the [010] direction, (b) the [001] direction and (c) the trace of the strain tensor.*

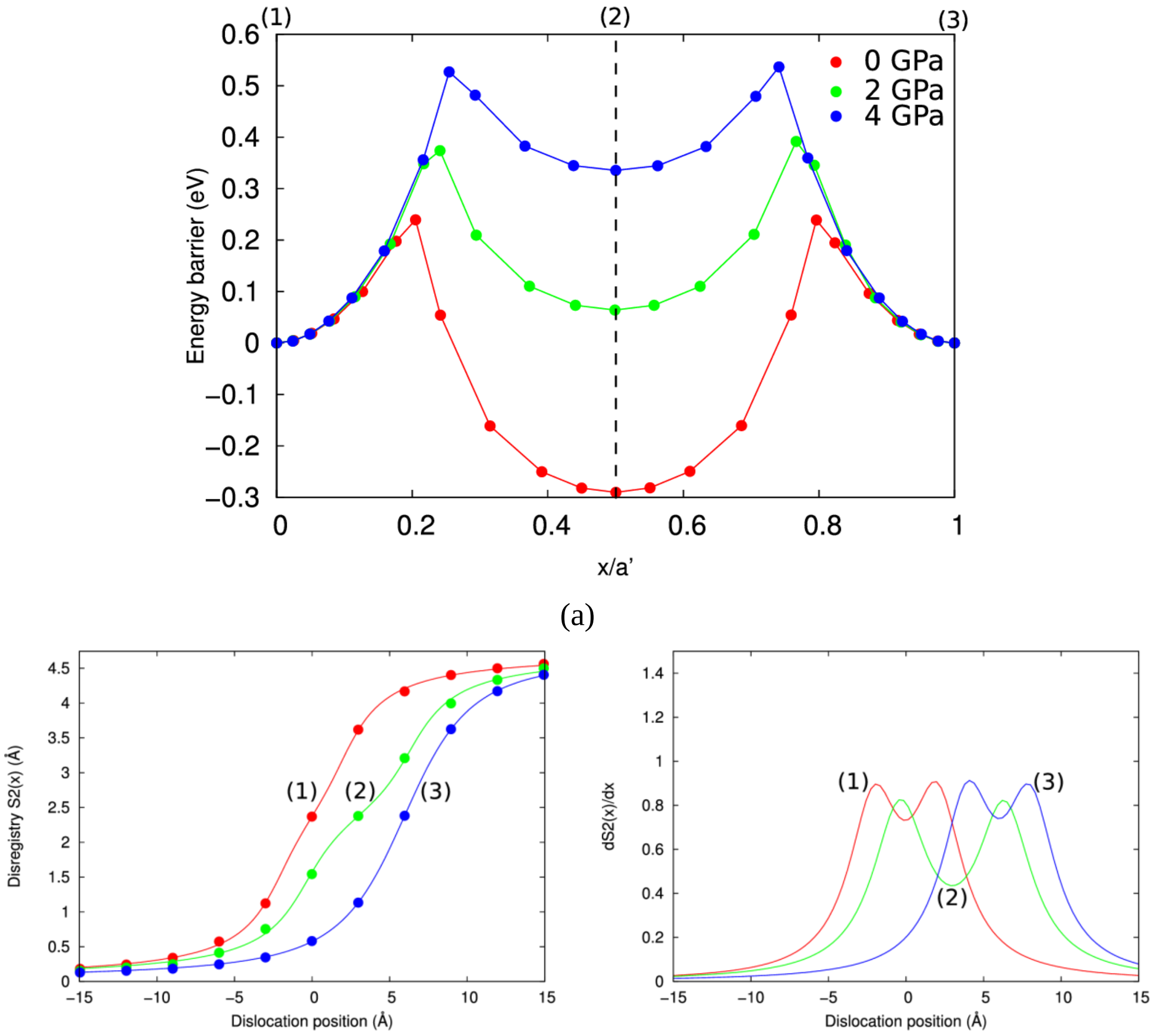

(a)

(b) (c)

Figure 4.12. *(a) The minimum energy path corresponding to the [100] screw dislocation glide in (010) plane at the low pressure range (0 – 4 GPa) computed using NEB calculations. The MEP is plotted as a function of dislocation position and the Peierls potential in (010) plane. (b) Atomic screw disregistries S(x) and (c) dislocation density dS/dx plotted as function of distance to the core centre in (010). The disregistries are computed to the cationic sub-lattice.*

The Peierls potentials for glide in (010), defined as the minimum energy path, are shown Figure 4.12 for 0, 2 and 4 GPa of pressure. Whatever the isostatic pressure, all potentials show a camel hump shape, with a dissociated metastable configuration at halfway (Figure 4.12. (b) and (c)). At 0 GPa, the stable dislocation is centred in a [B] labelled site (Figure

4.9) with the two partials exactly located in the adjacent [A] sites in (010). Increasing pressure, such dissociated state does not correspond to the most stable configuration but to a core state involved during the motion of the dislocation in (010). As the Peierls potentials are non-monotonic, we further performed NEB calculations under increasing applied shear strain components. A typical evolution of the minimum energy path as a function of the applied strain is shown Figure 4.13. From this kind of calculations, it is possible to extract the evolution of the maximum slope of the Peierls potential and plot the evolution of the slopes of the potential as a function of applied stress (Figure 4.14).

For the three low pressure conditions considered here, we find a good linear scaling of the maximum slope of Peierls potential with respect to the applied stress suggesting that [100](010) Peierls potentials are rather insensitive to the applied stress (Rodney *et al.* 2009, Kraych *et al.* 2016a). The Peierls stresses for [100](010) screw dislocations are 2.45 GPa at 0 GPa, 3.45 GPa at 2 GPa and 3.8 GPa at 4 GPa.

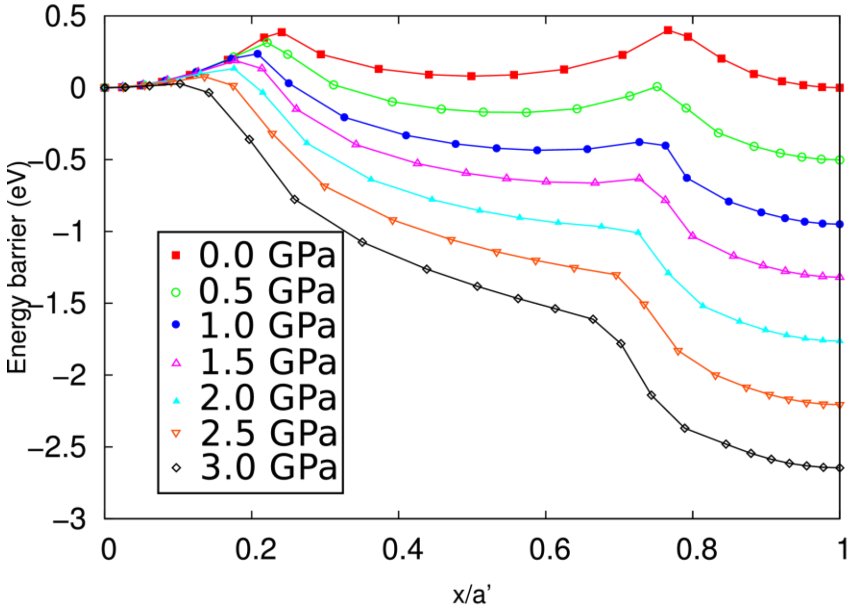

Figure 4.13. *The minimum energy path corresponding to the glide of a [100] screw dislocation in (010) as a function of the applied stress. The MEP is computed at an isostatic pressure of 2 GPa. The MEP is plotted as a function of dislocation position and the Peierls potential in (010) plane.*

As mentioned earlier, the Peierls stress values can also be computed using quasi-static loading. The stable dislocation core was thus subjected to simple shear ε_{yz} to calculate the critical stress and strain required to move the dislocation in the (010) plane. According to such calculations, the critical stresses are 2.76 GPa at 0 GPa, 3.91 GPa at 2 GPa, 4.36 GPa at 4 GPa. These critical stresses slightly overestimate the Peierls stress by less than 10% whatever the pressure investigated. It confirms that the Peierls stress is not strongly dependent on the applied stress as already shown by the linear trend in Figure 4.14. Finally, we also compute the corresponding stress for glide in (001). When the same dislocation core is quasi-statically loaded to make the [100] dislocation glide into (001) plane, a Peierls stress of approximately 7 GPa is necessary to move the dislocation at all isostatic pressures in the range 0-4 GPa.

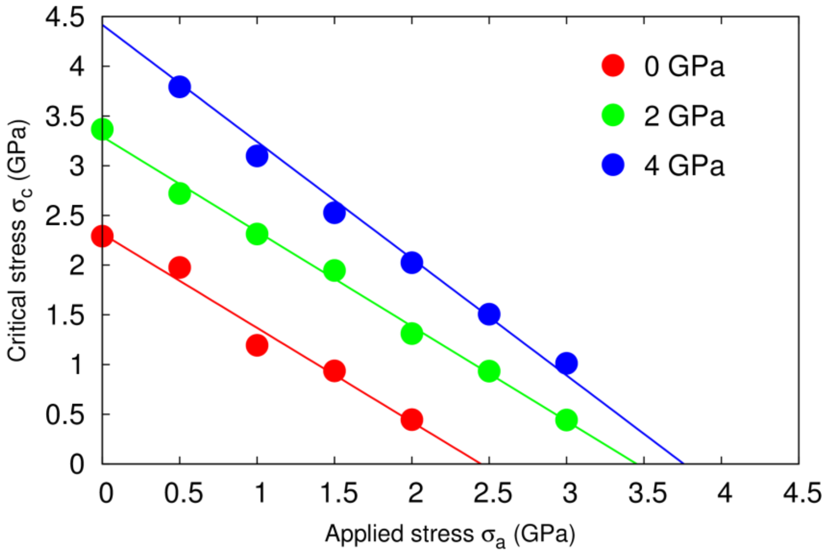

Figure 4.14. *Maximum slope of MEP plotted against the applied shear stress during the NEB calculation. The results of low pressure range are plotted. The linear dependency of maximum slope with respect to the applied stress indicates the [100](010) Peierls barrier is independent of applied stress.*

4.2.2 High pressure core configurations

Above 4 GPa of isostatic pressure, the calculations of dislocation core structures show a strong modification of the dislocation core configurations. The stable core configuration, as depicted in Figure 4.15, shows a tendency to spread in $\{021\}$ with a dislocation centre located in site labelled [B] or [B'] (see Figure. 4.9). Due to the *Pbnm* lattice, a high-pressure dislocation core has two variants corresponding to either a spreading in (021) or a spreading in $(0\bar{2}1)$, whereas the two configurations have exactly the same core width (Figure 4.15 (c)) and the same core energy. For pressure in the range 4-10 GPa, it is verified that the stable core configuration remains the one shown in Figure 4.15 (b) with no evidence of any fractional dissociation. Further the analysis of non-screw displacements around the core reveals an opposite tendency to previous cases. The negative regions around the core on trace of the strain tensor (Figure 4.16) shows the stable core is more contracted at higher pressure.

The computation of MEP through NEB between several stable core configurations enables to investigate the glide properties in $\{011\}$ planes. The MEP computed between two identical core configurations (located in site labelled B') in $(0\bar{1}1)$ is shown Figure 4.17. Along the path, the dislocation goes through a core position denoted B in Figure 4.9. The dislocation in B and B' corresponds to the two equivalent variants with a spreading in $(0\bar{2}1)$ at B' location and a spreading in $(02\bar{1})$ at B. Obviously, the minimum energy path is not symmetric and shows two distinguish slopes. The analysis of the core position along the MEP indicates that the core oscillates around $\{011\}$. Starting from a position B, the dislocation moves along [012] accordingly to its particular spreading. This process corresponds to the slowest slope on the MEP. The second part of the MEP is then dedicated to a rearrangement of the spreading in order to reach the proper core configuration in B'. The reverse situation is encountered when starting from B' location to reach B. Thus, glide in $\{011\}$ involves the two variant of the high pressure cores whose are alternatively reached along the glide path as shown by the blue and green path drawn in Figure 4.9.

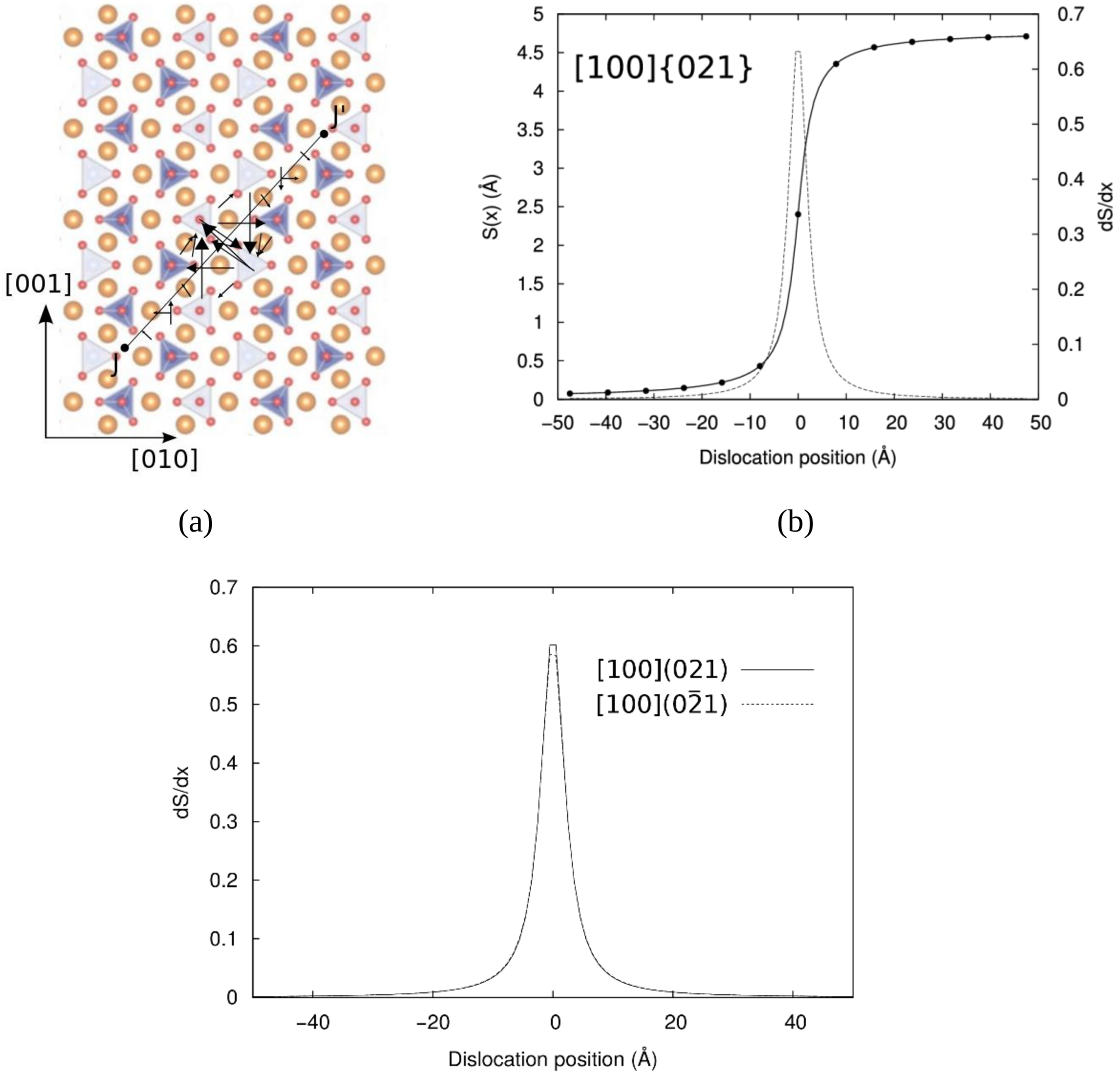

(a) (b)

(c)

Figure 4.15. *Screw dislocation core with [100] Burgers vector at 6 GPa (a) Atomic configuration of [100] screw dislocation core viewed along the line direction; the yellow, blue and red balls represent the Mg, Si and O ions and the SiO4 tetrahedra ; the arrows represent the differential displacement between the neighbours along [100] dislocation line; the arrows show a clear planar spreading of the core in* $(0\bar{2}1)$ *plane (b) Corresponding disregistry S(x) and the density of [100] burgers vector dS/dx for the cationic sub-lattice. The peaks of the density of [100] dislocation are not distinct to show any evidence of dissociation. (c) The half-width of two variant of [100] dislocation spread in (021) and* $(0\bar{2}1)$ *are compared.*

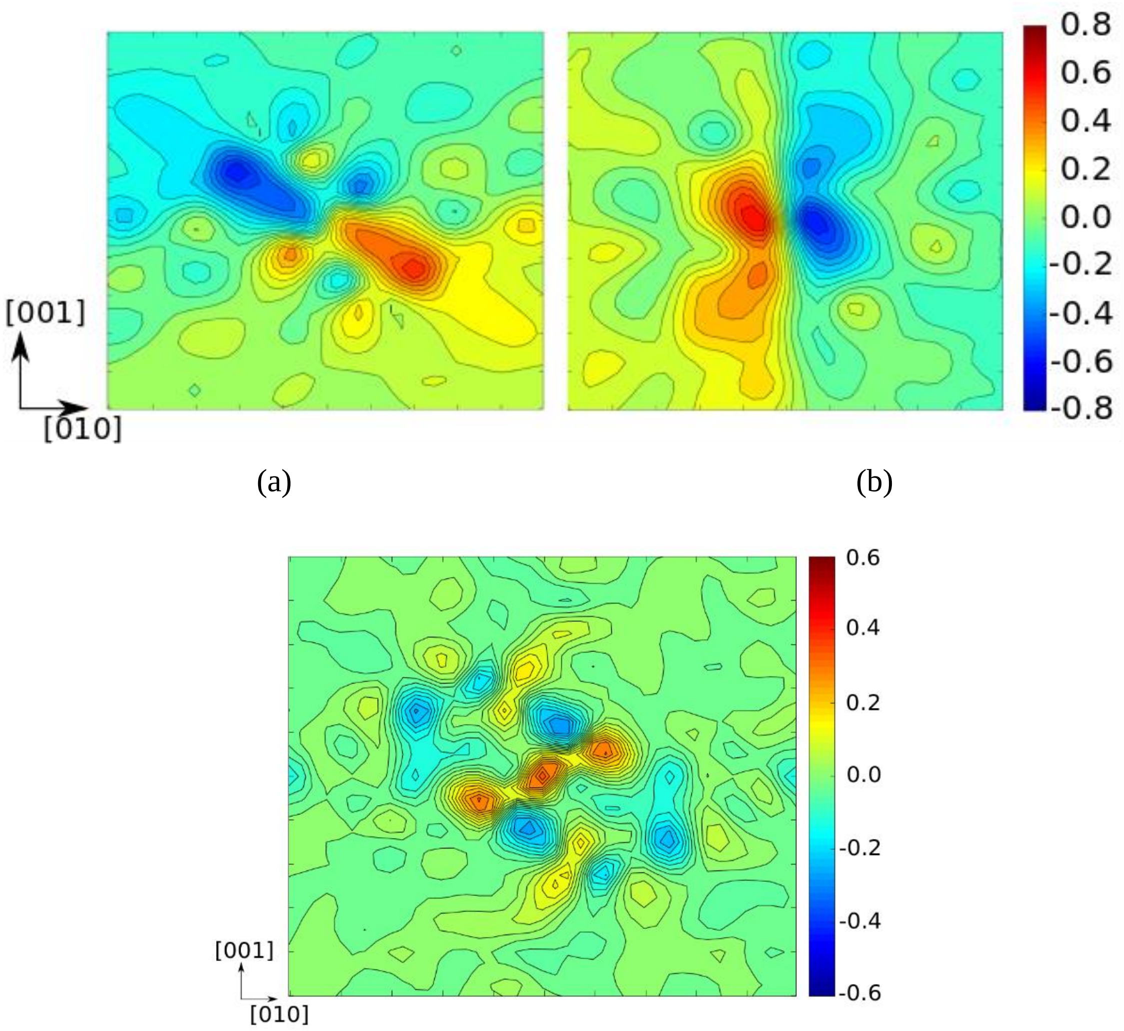

(a) (b)

(c)

Figure 4.16. *Representation of edge displacement field around the [100] dislocation core calculated using O sub-lattice at 10 GPa. Continuum displacement fields (in Å) along (a) the [010] direction, (b) the [001] direction and (c) the trace of the strain tensor.*

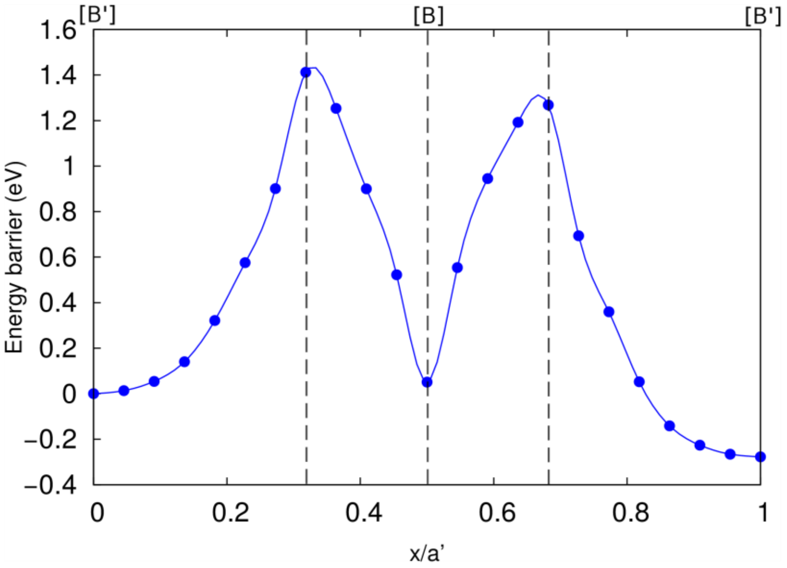

Figure 4.17. *MEP corresponding to glide in* $(0\bar{1}1)$ *of a [100] screw dislocation with a core spread in* $(0\bar{2}1)$. *The dislocation core present in B glide along blue path depicted in Figure 4.6. The dislocation moves from B to B' and B' to B, the MEP is mirrored. The calculation is performed at 6 GPa.*

The increase in height of the energy barriers as a function of pressure is plotted in Figure 4.18. In the pressure range 4-10 GPa, the maximum of the Peierls potential evolves from 1.2 eV/b to 2 eV/b. Computing the derivative of the MEP in {011} leads to an increase of Peierls stress in the range 9.3 GPa - 12.8 GPa. As for the computation performed at lower pressure, we further investigated the mobility of [100] dislocation in {011} by quasi static loading of the semi-periodic volume. However, as build, the simulated volume allows simple shear with maximum resolved shear stress in either (010) or (001). Nevertheless, by applying a simple shear to force the dislocation to glide in (001), we verified that above a critical stress, the dislocation glides in {011}. The Peierls stress computed from quasi-static loading in (001) are 7.0 GPa at 4 GPa, 7.48 GPa at 6 GPa, 8.06 at 8 GPa and 7.82 GPa at 10 GPa. Accounting for the angle of the glide in {011} with respect to the imposed shear strain in (001), these critical stresses computed from quasi-static loading conditions are in rather good agreement with the slopes of the MEP.

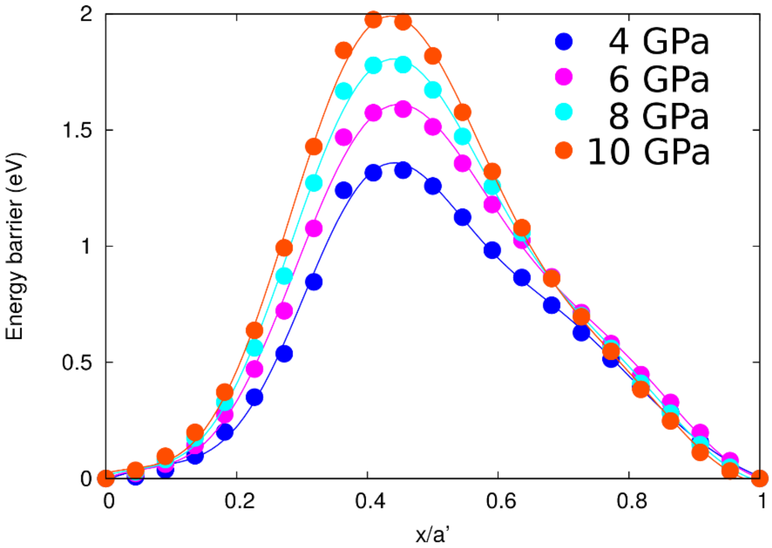

Figure 4.18. *MEP corresponding to the glide of a straight screw dislocation line (length b) of Burgers vector [100] in* $(0\bar{1}1)$ *at high pressure (from 4 GPa to 10 GPa). Plotting as a function of the dislocation core position projected in*$(0\bar{1}1)$*, the MEP describes the evolution of the Peierls potential for [100]*$(0\bar{1}1)$ *screw dislocation. In the MEP for glide from B' to B (Figure 4.9), at all pressure the barrier corresponding to the initiation of glide through (001) is steeper than the second half of the barrier corresponding to the* $(0\bar{2}1)$ *glide to reach B.*

4.3 Transition path from low pressure core to high pressure core configurations

As described in the previous section, the dislocation core configuration evolves with respect to the isostatic pressure from a core spread in (010) at low pressure to a core spread in {021} at high pressure. But both core configurations can be stabilized at any pressure. The two core centres [A] and [B] are distant from exactly 1/2[001]. Relaxing the two core configurations using a periodic system allows a precise determination of the core energy and also an investigation of the transition pathway from one configuration to the other. Figure 4.19 shows the minimum energy path resulting from a NEB calculation using the two cores as initial and final states. Below 4 GPa of pressure, spreading of the dislocation in (010) is energetically favourable, although the change in core energy is less than 0.5 eV/b. On the contrary, the stability of the core spread in {021} is strongly enhanced by the increase of pressure with a difference of core energy which reaches around 1 eV/b at the highest pressure investigated in this work: 10 GPa. For all pressures, the transition from the stable configuration to the metastable one is found to be associated with an energy barrier which increases with pressure from 1 eV/b to more than 1.5 eV/b (at least in the pressure range 2-10 GPa).

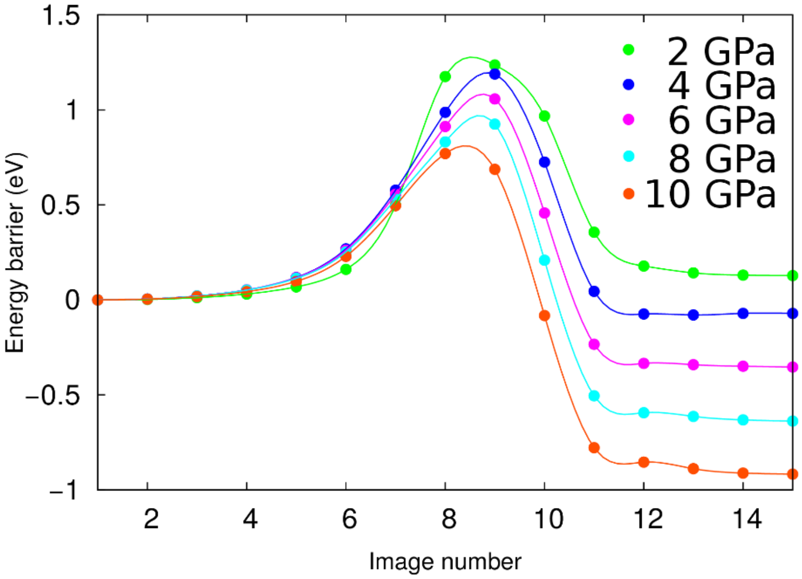

Figure 4.19. *Transition energy barrier from the low pressure stable core to high pressure stable core.*

At high pressure, introducing, as initial state, a metastable core spread in (010) and applying a quasi-static loading to enhance the glide in (010) leads to the computation of a threshold stress above which the metastable core transforms into the stable core spread in {021}. By performing these calculations 6, 8 and 10 GPa of pressure, ones can transform the transition energy barrier in terms of resolved stress (Figure. 4.20). Extrapolating the correspondence between stress and energy, we can deduce from Figure 4.15 at which stress a stable high pressure core "cross slips" into a (010) planar configuration. It is worth noticing that the similar procedure performed at low stress (i.e., below 4 GPa) never leads to the occurrence of the high pressure core configuration, the dislocation glide to next stable configuration with a barrier height of 0.5 or lower. This barrier height is lower than the energy barrier associated with the transition between two cores.

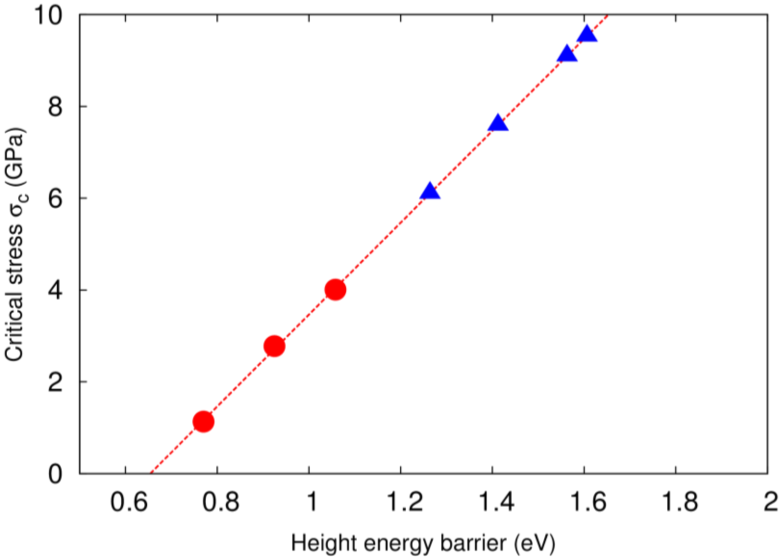

Figure 4.20. *Cross-slip stress versus the height of energy barrier. The red dots correspond to the stress values computed for transition path using quasi-static loading. The triangles represent the extrapolated stress values based on the height of the energy barrier transition.*

4.4. Summary

The dislocation core stability and the lattice friction associated with [100] screw dislocations are analysed in this chapter. Initially at 0 GPa the [100] screw dislocation forms a planar core with a strong spreading in (010) plane. The stable dislocation exhibits dissociation of the core as two strong partials of ½[100] separated by an approximate distance of one lattice parameter along [001] direction (i.e., ~7Å). The lattice friction against glide of this dislocation core in the absence of thermal activation (at 0 K) is estimated using the quasi-static loading. The Peierls stress estimated for glide in (010) and (001) are 2.76 GPa and 7 GPa respectively. The effect of pressure on the [100] dislocation core is studied leading to distinguish two domains, a low (0 – 4 GPa) and a high pressure range (4 – 10 GPa). Below 4 GPa, the most stable core has a planar configuration spread in (010), but increasing pressure tends to stabilize a more compact core (*i.e.*, with no well-developed dissociation into two partials). This is supported by the evolution of the camel hump shaped Peierls barrier computed using NEB calculations. Above 4 GPa, the dislocation core structure changes. A core spread in {021} core is identified to be energetically more favourable than the other cores. This core spread in {021} plane has two variants due to the mirror symmetry of the *Pbnm* space group of forsterite. This dislocation core glides in {011} plane with Peierls stresses of 7 GPa (at P = 4 GPa) to 10 GPa (at P = 10 GPa). These Peierls stress values are in good agreement with the results from quasi-static loading conditions. This change of stability of the dislocation core with pressure has strong implication on the slip system activities. Our calculations suggest that [100](010) slip would be the most favourable slip system below 4 GPa, [100]{011} slip becoming more favourable at higher pressures.

Table 4.1. *Dislocation disregistry analysis of dislocation with [100] Burgers vector. Half width* ξ_i *of the dislocation core estimated from the fit of the atomic disregistries using equation (4.1).*

Pressure (GPa)	Type of core configuration	Spreading plane	Distance of separation (Å)	Half width	
				ξ_1(Å)	ξ_2 (Å)
0	Stable	(010)	7.15	2.19	2.19
0	Metastable	(010)	-	2.46	-
0	Metastable	{021}	-	2.31	-
2	Metastable	(010)	6.73	2.14	2.14
2	Stable	(010)	-	2.37	-
2	Metastable	{021}	-	2.34	-
4	Metastable	(010)	6.43	2.07	2.07
4	Stable	(010)	-	2.34	-
4	Metastable	{021}	-	2.40	-
6	Metastable	(010)	6.09	2.02	2.03
6	Metastable	(010)	-	2.30	-
6	Stable	{021}	-	2.43	-
8	Metastable	(010)	5.85	1.99	1.98
8	Metastable	(010)	-	2.27	-
8	Stable	{021}	-	2.45	-
10	Metastable	(010)	5.60	1.96	1.96
10	Metastable	(010)	-	2.25	-
`	Stable	{021}	-	2.48	-

5. [001] screw dislocations

In this chapter we discuss the theoretical modelling of dislocation core and lattice friction associated with [001] Burgers vector. Initially at 0 GPa two possible [001] dislocation cores structures that can be stabilised are analysed. Then, dislocation core energies and lattice friction of both the dislocation core types are computed. Further, the effect of pressure on the core energies and mobility of the dislocation are investigated.

5.1. Dislocation core structure at 0 GPa

The [001] screw dislocation core structure is computed using a fully periodic quadrupole arrangement of dislocations (Chapter 2, Section 2.4.2). Inserting [001] dislocation into the structure leads to two possible dislocation core configurations depending on the exact position of the initial dislocation centre (Figure 5.1). The resulting core structures are labelled as “C” and “D”. At first the core configuration “C” is obtained by inserting the dislocation line with [001] Burgers vector centred on a Mg cation site between four SiO_4 tetrahedra (Figure 5.1).

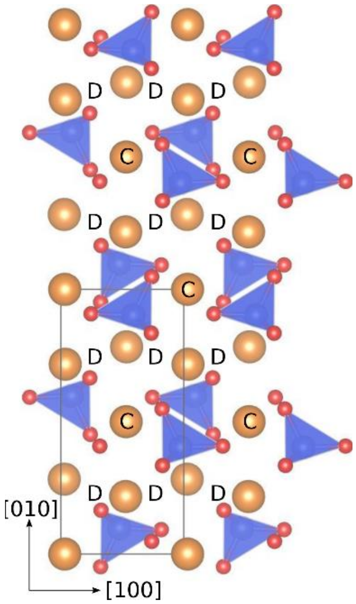

Figure 5.1. *Forsterite supercell at 0 GPa, viewed along [001] axis. The signs C and D represent the possible locations in system to introduce [001] screw dislocation of type “C” and type “D” respectively.*

After energy minimisation the core structure is analysed using the differential displacement maps. All significant displacement arrows around the dislocation line are restricted to a small area within one unit-cell (Figure 5.2). Thus, the core appeared to be compact with no particular evidence of spreading in any preferential plane.

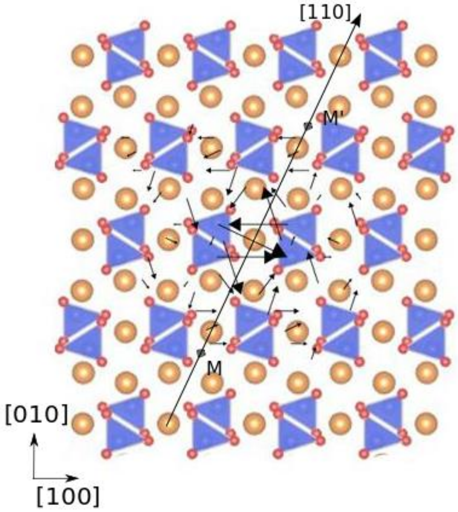

(a)

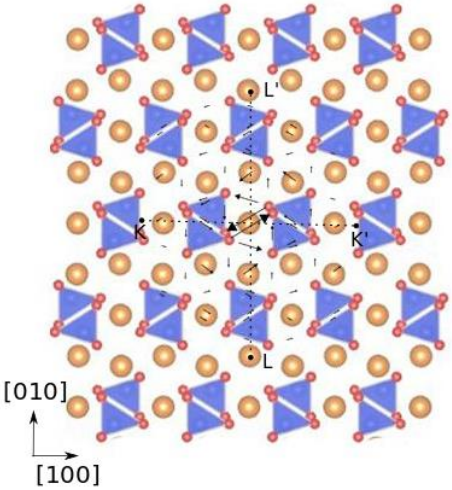

(b)

Figure 5.2. *[001] screw dislocation of type "C". (a) Atomic core configuration viewed along the dislocation line; yellow, blue, and red spheres represent Mg, Si, and O ions, respectively; SiO_4 tetrahedron are shown in transparent blue; solid arrows describe the differential displacement along the [001] direction between two ions. (b) The same core described within the oxygen sub-lattice only.*

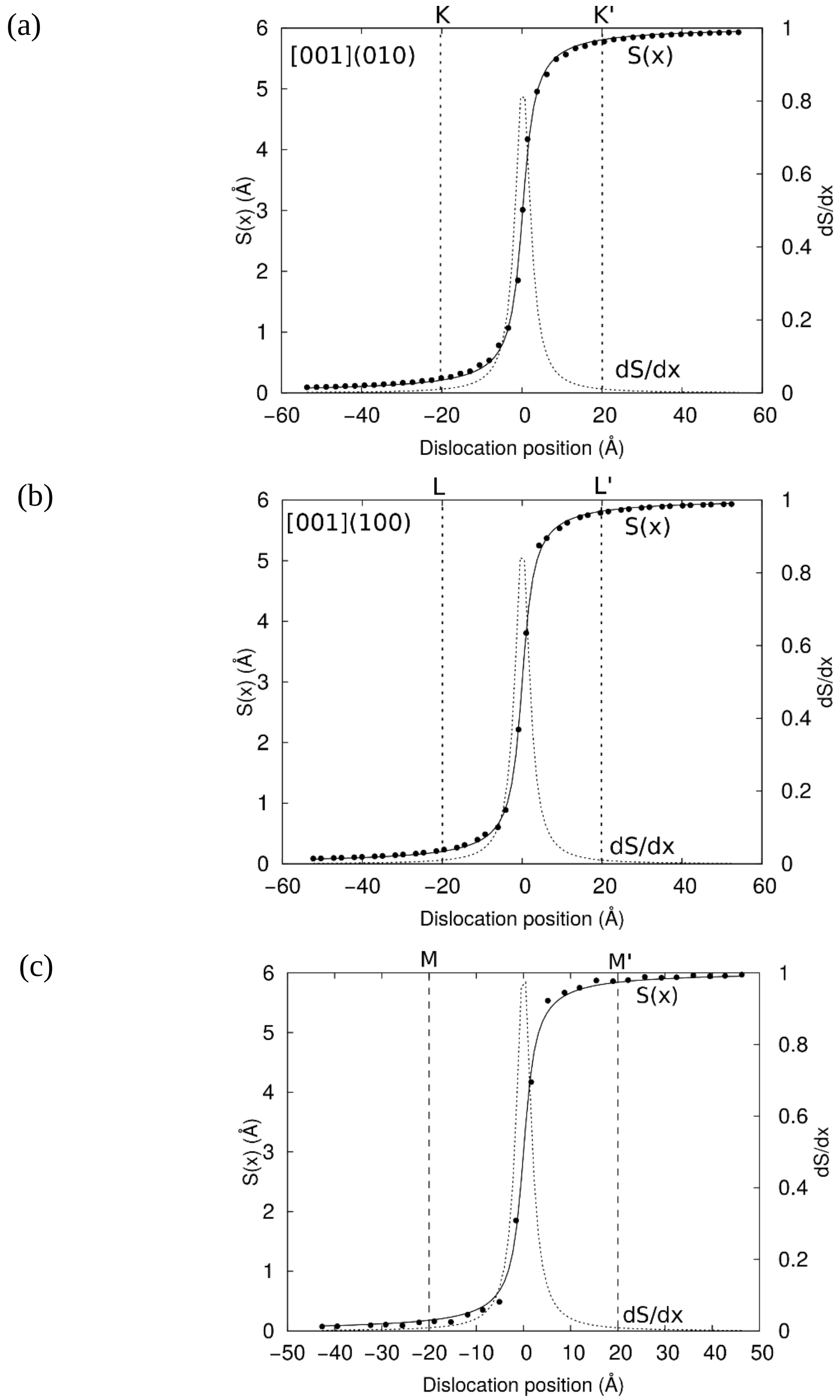

Figure 5.3. *Disregistry function S(x) and the [001] Burger vector density dS/dx of the screw dislocation of type "C" (dotted lines) for the cationic sub-lattices in (010), (100), and {110}, respectively. These disregistries are calculated along the KK', LL', and MM' profiles depicted in figure.*

This is confirmed by computing the disregistry functions in (100), (010), and {110}, planes in zone axis with the Burgers vector (Figure 5.3). Independent of the plane, the core profile is narrow with a width smaller than 5Å, preserving the shape of the SiO_4 tetrahedra. No edge displacements are observed around the [001] dislocation core of type "C". Such a compact core configuration is consistent with previous attempts to model screw dislocation cores in forsterite using THB1 potential (Walker *et al.* 2005b; Carrez *et al.* 2008), although the geometry of the simulated volumes are different. Indeed, compared to the fully periodic system used here, the previous calculations of Walker and co-workers were performed using a "cluster" approach with fixed boundary shells of cylindrical symmetry around the dislocation line.

The second core configuration "D" is achieved by inserting a [001] dislocation line in the plane containing Mg cations between three SiO_4 tetrahera (Figure 5.1.). Energy minimisation of this dislocation core results in a clear spreading in {110} as shown by the differential displacement map, Figure 5.4. Further details on the core structure are revealed using the disregistry analysis (S(x)) in the cationic sub-lattice and its first derivative in the {110} plane (Figure 5.5.). The dislocation core structure "D" corresponds to a dissociation of the core into a set of two partial dislocations of almost equal partial Brugers vectors b_p = 1/2[001]. The core spreading of each partial is narrow with the half-width values of 1.4 Å and 1.5 Å, the minor variation in half width between the partials is associated with the quality of the fit. The derivative of the disregistry function $dS/_{dx}$ highlights the dissociation with two isolated peaks of Burgers vector density separated by a distance of R = 10.19 Å, it is estimated as the distance of separation between two partials. In case of dissociated dislocation, the dissociation width is influenced by the stacking fault energy (γ). For a separation distance of R, the stacking fault energy between two partial screw dislocations (with Burgers vectors $\vec{b_i}$ and dislocation line vectors $\vec{\xi_i}$) can be extracted using the elastic equilibrium equation (Hirth and Lothe 1982).

$$\gamma = \frac{\mu}{2\pi R}(\vec{b}_1 \cdot \vec{\xi}_1)(\vec{b}_2 \cdot \vec{\xi}_2) \tag{5.1}$$

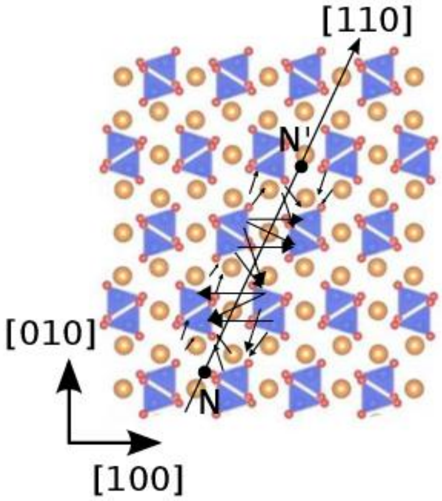

Figure 5.4. *[001] screw dislocation of type "D", atomic core configuration viewed along the dislocation line, solid arrows describe the differential displacement along the [001] direction between two ions.*

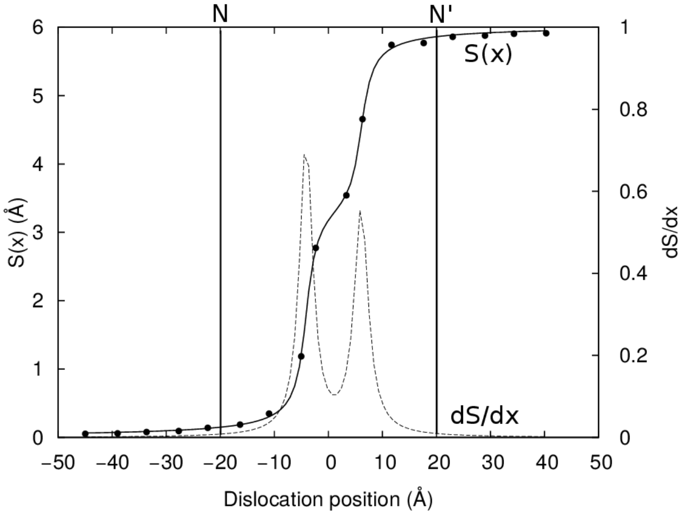

Figure 5.5. *Disregistry function S(x) and the [001] Burger vector density dS/dx of the screw dislocation of type "D" (dotted lines) for the cationic sub-lattices in {110}.*

For the calculated dissociation distance of R = 10.19 Å, the stacking fault energy is thus expected to be of 0.0457 eV/Å^2. One the other hand, from the [001]{110} GSF calculation performed by constraining the Si atoms to move perpendicular to the glide plane while Mg and O atoms are allowed to freely relax in all directions (Case 2), the γ energy associated with the $\frac{1}{2}[001]\{110\}$ stacking fault is 0.042 eV/Å^2 . The good agreement between the γ energies, derivated from the GSF calculations or the core configuration is noticeable. This emphasis that the stacking fault configuration within the dislocation core should be identical to the atomic configuration achieved using the maximum degree of freedom for GSF calculations. Similar to type "C", no evidence of edge displacement components is observed around the dislocation core.

5.2. Core energy comparison at 0 GPa

For screw dislocations arranged in a quadrupole system, the energy of the dislocation core per unit Burgers vector length scales with the intrinsic lengths (d_1, d_2) of the dislocation arrangement according to the following relationship proposed by Ismail-Beigi and Arias (2000).

$$E = E_{core} + E_{elastic} = E_{core} + \frac{\mu b^3}{4\pi}\left\{Ln\left({}^{d_1}/_{r_c}\right) + A\left({}^{d_1}/_{d_2}\right)\right\} \quad (5.2)$$

In the above equation (5.2), E on the left corresponds to the energy difference between the energy of the quadrupole system and the defect free system. On the right, E_{core} is the energy of the dislocation core, the rest corresponds to the energy due to the elastic interactions between the dislocations in the system. The elastic energy is computed using anisotropic elastic theory formulation implemented in BABEL code (Clouet 2017). In the elastic energy term d_1 and d_2 are the distances between the positive and negative dislocations along x and y directions respectively, μ is the anisotropic shear modulus and r_c is the cut-off radius for the core energy.

The energies for quadrupole system of dislocations are computed by varying the simulation box dimension from ~75 Å to ~200 Å along the x and y directions. The minimized energies from different dislocation box sizes are plotted as a function of elastic energy (Figure 5.6), the energies increase linearly with increase in box dimension. As per elastic theory the energy increases linearly, fitting of the values gives the dislocation core energy. The dislocation core energies for core configurations of types "C'' and "D" are 4.1036 eV/b (0.6813 eV/Å) and 3.2251 eV/b (0.5355 eV/Å) respectively. From the energy values the dislocation core with dissociated core of type "D" is more stable than the compact core of type “C” . The linear fit also provides the anisotropic shear modulus μ = 51.8 GPa. This compares well with the isotropic shear modulus μ = 65 GPa calculated from the elastic moduli.

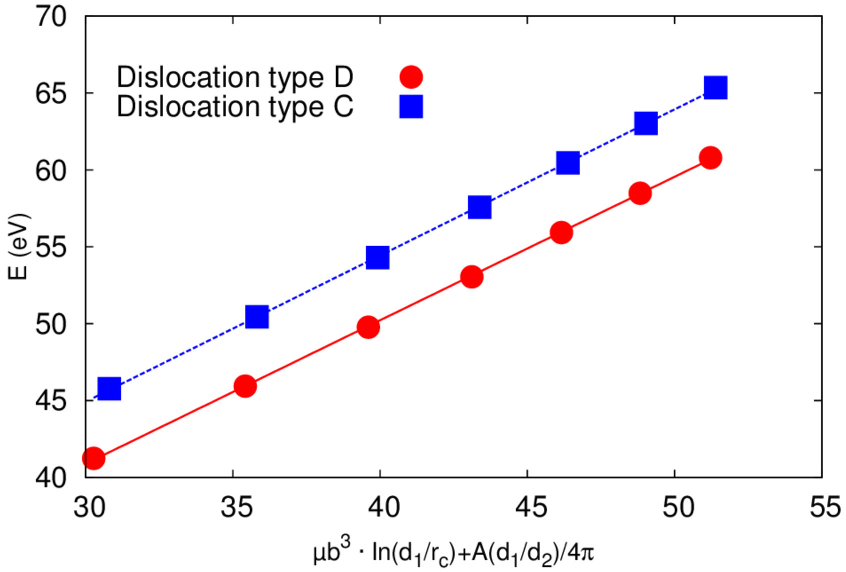

Figure 5.6. *Evolution of the total energy of the dislocation (elastic energy and core energy) obtained from the atomistic calculation as a function of the elastic energy of the dislocation only depending on the distance between dislocations in the quadrupole configurations (see Eq. (5.1)). The solid circle (red) and solid square (blue) symbols correspond to the results from dissociated dislocation core (“D”) and compact non-planar core (“C”) respective.*

5.3. Lattice friction at 0 GPa

The lattice friction associated with glide of [001] screw dislocation is computed using the fully-periodic quadrupole simulation cells. The critical stress required by the dislocation with [001] Burgers vector to promote glide in different slip systems are performed by quasi-static loading of the simulation cells. From the core energies, dissociated dislocation of type “D” is more stable than the compact non-planar dislocation of type “C”, the lattice friction associated with [001] screw dislocation glide of type “D” is therefore presented and analysed first.

For the [001] screw dislocation to glide in (010) plane, at critical stress value greater than 6.10 GPa must be applied. At critical stress, an analysis of the conjugate gradient minimiser steps shows that once the dislocation is set into motion, it exhibits a different core structure (Figure 5.7.), entirely planar, spread in (010) with no evidence of dissociation (Figure 5.8). It is worth noting that such a planar configuration cannot be stabilised without applying strain (or stress) in the simulations. Indeed, we verified that without imposed strain such planar configuration always recombines into the core of type “D” (Figure 5.4). However, once this transient state (Figure 5.7) is reached, the dislocation core can travel over several lattice repeats before finally falling again into another stable core configuration (Figure 5.4).

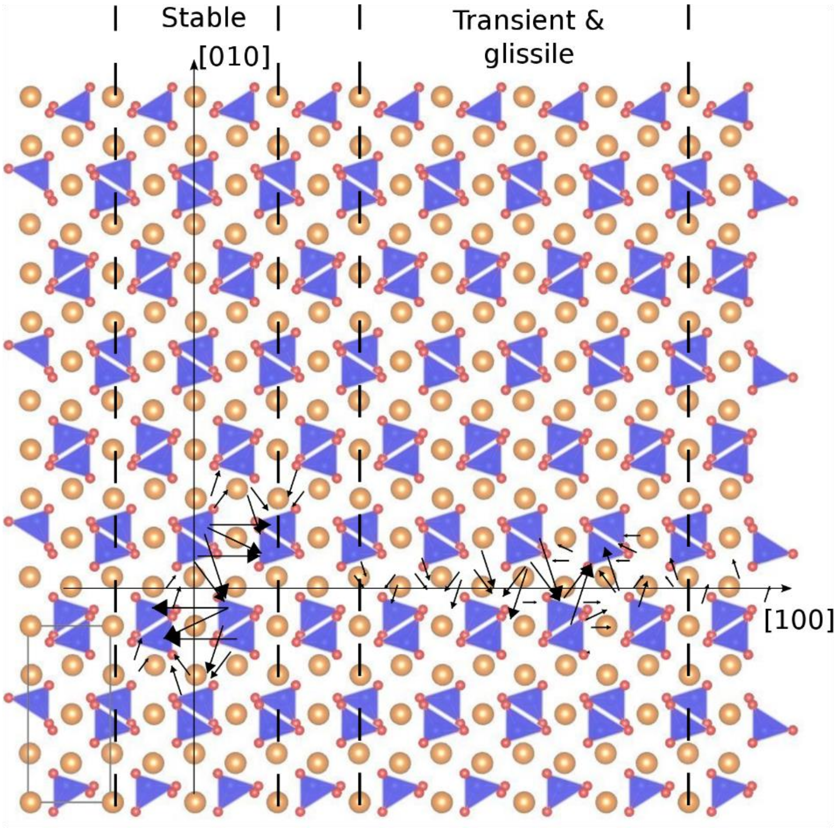

Figure 5.7. *Unlocking mechanism of [001] screw dislocation in a super cell of forsterite crystal view along [001] direction. When the system with screw dislocation of stable core “D” is quasi-statically loaded to glide in (010) plane, beyond critical stress value the dislocation unlocks into a transient high-energy core and glide past several lattice repeats before again lock into a stable core configuration similar to the initial core.*

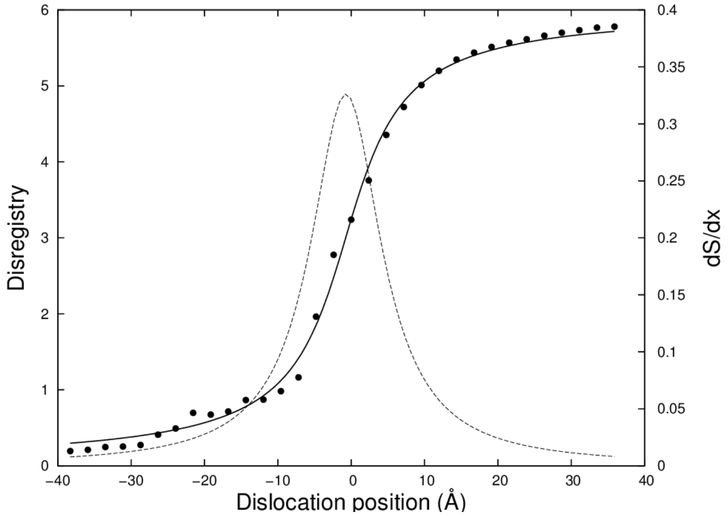

Figure 5.8. *Disregistry function of the transient planar configuration of the [001] dislocation as it glides in (010) plane.*

Once the initial dislocation core is dissociated under resolved shear stress, the [001] dislocation glides as a single planar transient core of high energy. This explains the unstable stacking fault energy barrier (Figure 3.9. (d)). This glissile transient core of [001] dislocations forming a planar core spread in (010) plane matches well with the [001] planar screw dislocation computed using the PN model by Carrez *et al.* (2008).

Now the quasi-static loading process is repeated to promote glide of [001] dislocation in (100). By progressively loading the simulation box the dislocation starts to glide at a resolved stress greater than 3.94 GPa. It is observed that under applied stress, the dislocation exhibits a glide in {110}. During the motion the two partials glide together while keeping the stacking fault width constant. The Schmid factor S, can be used to quantify the slip of [001] dislocation into $(1\bar{1}0)$ for a shear stress applied to glide in (100). For an applied shear stress of σ_a the resolved shear stress σ_{RSS}, i.e., the component of stress that actually acts on a given slip system can be computed from the following expressions.

$$\sigma_{RSS} \equiv S\sigma_a \tag{5.3}$$

$$S = cos\psi \cdot cos\lambda \tag{5.4}$$

Where $cos\psi$ is the direction cosine between the direction of the applied force and the slip direction and $cos\lambda$ is the direction cosine between the direction of the applied force and the slip plane normal. For our case the Schmid factor is 0.382, and the corresponding σ_{RSS} is 1.51 GPa. On the contrary, for gliding in (100), we expect a Peierls stress above 3.94 GPa although this cannot be verified numerically.

Similar calculations have been repeated starting from a “C” dislocation core configuration, i.e. the metastable configuration of the screw dislocation. As previously described, the “C” dislocation core configuration has been subjected to quasi-static loading in simple shear. The metastable core configuration glides in (010) for a critical stress close to 5.64 GPa. On analysis of steps from conjugate minimiser, after the critical stress of 5.64 GPa, the dislocation starts to glide in (010) and minimises to a dislocation core similar to type “D”. For the case of promoting glide in (100) plane using quasi-static loading of type “C” dislocation core, after a critical stress of 6.68 GPa the compact dislocation core dissociates into two equal partials separated in {110} similar to the core of type “D”. This transformation of core configuration from “C” to “D” on application of stress further validates our understating of type “D” core being more stable than of type “C”.

5.4. Effect of pressure on [001] dislocations

Dislocation core energies are compared between type “C” and type “D” core configuration, over a pressure range of 0-10 GPa. At all pressures it is observed that the dislocation core of type “D” is more energy favourable, the values of core energies computed at different pressures are tabulated in Table 5.1. The stacking fault (γ) energy for [001] dislocation dissociation in {110} is estimated at higher pressure values are 0.0424 eV/Å^2 at 4 GPa and 0.0416 eV/Å^2 at 10 GPa. It is worth noticing that from the core configuration analysis, the ½[001]{110} stacking fault energy seems to be pressure insensitive. This trend is nevertheless fully consistent with Durinck *et al.* (2005) results on [001](110) stacking fault energies calculated using DFT simulations showing that for the same pressure range, the GSF energy corresponding to [001](110) remains rather constant.

Table 5.1. *The dislocation core energies computed for [001] screw dislocations arranged in quadrupole configuration.*

Pressure (GPa)	[001] screw dislocation core energy (eV/b)	
	Compact core type "C"	Dissociated core type "D"
0	4.1036	3.2251
2	4.0055	3.0765
4	4.1164	3.1155
6	4.2302	3.2958
8	4.2604	3.4154
10	4.2332	3.4203

The effect of pressure on the glide of [001] dislocation of type "D" in (010) and {110} slip planes are analysed by repeating the quasi-static loading simulations over a pressure range of 0 – 10 GPa. Irrespective of the pressure the gliding mechanism remained the same for (010) glide, it occurs through the conversion of the dissociated core into a planar core at stress of 5.88 GPa at 2 GPa, 6.04 GPa at 4 GPa, 5.82 GPa at 6 GPa, 5.59 GPa at 8 GPa and 5.32 GPa at 10 GPa. The decrease in critical stress values with increase in pressure exhibit a softening effect on [001](010) slip system. With increase in pressure the atoms in the system are expected to come closer, resulting in the barrier to transform between type D core and planar transient dislocation core decreases. For the case of glide in {110} plane the resolved shear stress values at different pressures are 1.6 GPa at 2 GPa, 1.63 GPa at 4 GPa, 1.61 GPa at 6 GPa, 1.61 GPa at 8 GPa and 1.61 GPa at 10 GPa. This shows that the glide in {110} plane is less sensitive to an increase of pressure in the system.

5.5. Summary

In this chapter, we characterised the stable configuration for [001] screw dislocations. Two possible dislocation cores were proposed, the first type is of a compact non-planar core of type "C" and the second is of a dissociated core of two 1/2 [001] partials separated in {110} plane by a distance of 10.19 Å. Based on the dislocation separation distance the stacking fault energy is computed using equilibrium equation, it compares well with the stacking fault energy obtained from the GSF calculations. From the comparison core energy between dislocations of type "C" and "D" extracted from quadrupole arrangement of [001] dislocation show that the dissociated core of type "D" exhibits a more stable core. The stable core of type "D" was subjected to gradual shear loading to extract information on lattice friction in different slip systems. As first for the dislocation to glide in (010) plane, at stress values greater than 6.10 GPa the [001] glides as a transient planar core. The transient planar core compares well with the planar core of [001] dislocation spread in (010) predicted by the PN model (Carrez *et al.* 2008). With increase in pressure the critical stress required to promote glide in (010) plane decreases. This exhibits a softening of [001](010) slip system with pressure. For a shear of [001] dislocation in the (001) dislocation at stress value greater than 3.94 GPa, the dislocation starts to glide in {110} plane. Using the Schmid factor the resolved shear stress to glide in {110} is found to be 1.51 GPa. The resolved stress required to promote is non-Schmid glide in {110} remains less sensitive to increase in pressure in the system.

6. Discussion

6.1. Core configuration at 0 GPa

At 0 GPa, we identify two stable core configurations for [100] and [001] dislocations both are slightly dissociated and planar. Therefore, one can assume some tendency for the primary slip systems to be [100](010) and [001](110). Others metastable core configurations, in particular for [100] dislocations are also found which may correspond to different slip systems. This might be linked to the richness of slip systems observed experimentally. It may be useful to add here that the difference in core energies are of a few eV/b or even less.

Qualitatively our calculations are in agreement with experimental observations of dislocation slip systems at low pressure. The occurrence of a dissociated core state may also explain why [100](010) seems to be without ambiguity observed at high temperature, the temperature may stabilise or promote the dissociation although this conclusion has to be confirmed by further calculations. For [001] dislocations, recently at low temperature conditions using *in situ* TEM nanomechanical testing, Idrissi *et al.* (2016), captured the motion of [001] dislocations gliding in {110}. At the scales of the observation (timescale corresponding to the video capture, and length-scale corresponding to the spatial resolution in weak-beam dark-field) glide was observed to be smooth. This behaviour is in agreement with the planar configuration of the dislocation core we propose. Our results, show that [001] dislocations glide in {110} at low temperature (as our calculations are performed using molecular statics) can be activated with a low Peierls stress value of 1.51 GPa. More quantitatively, from Figure 1.7 for [001] dislocations, the Peierls stress value of 1.51 GPa compares well with the range of CRSS values in intermediate temperature range obtained experimentally. In comparison, glide of [100] dislocations in (010) requires a higher Peierls stress value of 2.45 GPa and one can imagine that such a slip system will be activated at higher temperature.

6.2. Locking-unlocking mechanism

For [001] screw dislocation to glide in (010), our calculations suggest a glide path involving different core structures. In particular, we find the occurrence of an undissociated planar (010) core configurations. At stresses higher than the Peierls stress, the dissociated [001] core adopts some planar transient states (Figure 5.7 and Figure 5.8). Since it is impossible to preserve the atomic configurations of these transient planar configurations when minimising the energy of the system if no external strain/stress is applied, it is suggested that the planar core configurations for [001] dislocation are highly unstable. Since the glide may involve high-energy configurations, we confirm a clear tendency of the [001] core to glide through a so-called locking–unlocking mechanism (Couret and Caillard 1989), as recently described at the atomic scale in hpc metals (Clouet *et al.* 2015).

Unlike the Peierls mechanism where dislocation jumps between adjacent Peierls valleys, this mechanism of locking-unlocking involves high energy, highly mobile, core configurations which may skip several Peierls valleys before locking itself back to a minimum energy core (Figure 6.1). This suggestion was initially proposed by Carrez *et al.* (2008) based on unrelaxed core energy calculations and the PN model of core spreading. One achievement of this work is to bring strong evidences that such a configuration is involved in the glide of a straight dislocation. Although a comparison with PN model calculations may not be straightforward, it is however interesting to note that the transient core of the [001] screw dislocation in (010) does not show any evidence of dissociation. Qualitatively, the transient cores are similar to those computed using the PN model (Durinck *et al.* 2007). This suggestion could be verified experimentally by recording a jerky motion of dislocations in transmission electron microscope (TEM) for example. A detailed study of the transition from the stable configuration to the transient state was unfortunately not performed during this work. The details of such a mechanism can be a future research direction.

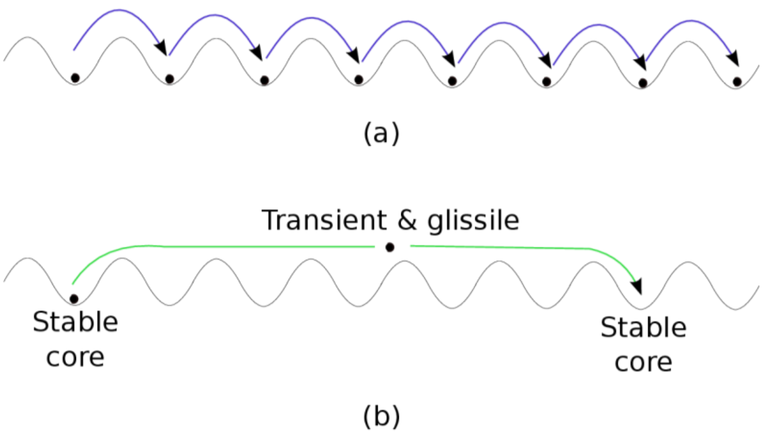

Figure 6.1. *Comparison of dislocation motion between (a) Peierls mechanism and (b) Locking – unlocking mechanism.*

6.3. Effects of pressure

In the range of values encountered in the Earth's mantle, pressure has a strong influence on the electronic structure and bonding of minerals. One could thus expect pressure to affect the structure of crystal defects and several examples, including olivine, are now well documented (Durinck *et al.* 2007; Carrez *et al.* 2015; Hirel *et al.* 2014; Kraych *et al.* 2016b). From the experimental point of view, lattice preferred orientations (LPO) are commonly used as a marker for the activation of slip systems and the change of LPO with pressure reported (Couvy *et al.* 2004; Mainprice *et al.* 2005) is an indication of the importance of this effect. Our calculations shed new light on this phenomenon.

Pressure has significant effects on the stability of the [100] dislocation cores. Below 4 GPa, the stable core spread in (010) shows local edge displacement of atoms within the vicinity of the core perpendicular to (010). This confirms the report by Durinck *et al.* (2005a) of displacements of atoms outward from (010) during [100] rigid-body shear observed along the γ-surface energy path. The present calculations confirm the occurrence of the dilatation state within the [100] screw core. In the context of the upper Earth's upper mantle, the dilatation state of the core may have strong implications on the activation of the [100] slip with respect to an increase in pressure. Indeed, as proposed by Durinck *et al.* (2005a), one effect of pressure is to work against this dilatation state, leading to an intrinsic hardening of the glide properties of [100](010). This is validated from the analysis of the most favourable dislocation cores found at higher pressures (4 -10 GPa) conditions, where the stable core spread in {021} has a contracted core (Figure 4.16).

It is useful to highlight that our calculations show that lattice friction for [001] is rather insensitive to pressure whereas pressure seems to intrinsically harden [100] slip. Thus we provide a further support to the experimental observations.

6.4. Pencil glide for [100] dislocations

The slip that occurs on several, potentially non-crystallographic planes is referred as the pencil glide. This type of glide mechanism is commonly observed in bcc metals (Taylor and Elam 1926; Ngan and Wen 2001) where it has originally been observed and reported from the occurrence of wavy slip traces which did not follow the expected dense planes. From deformation experiments performed at 1000°C with strain rates between 10^{-6} and 10^{-3} s^{-1}, a composite cross-slip of [100] dislocations on {0kl} has been reported (Raleigh 1968; Poirier 1975). By computing the evolution of dislocation cores with pressure, we also find that [100] glide follow a zig zag path to glide in $(0\bar{1}1)$, this glide is composed of glides in (001) and {021} (Figure 4.9). Being able to switch from different configurations, the screw dislocation in its glide may change glide plane at each step as a response to external loading. At a higher level the resulting motion may appear non-crystallographic although at the microscopic level it is always rigorously crystallographically controlled.

As one of the possible mechanisms for the onset of plasticity in metals is the beginning of movement of straight screw dislocations by pencil glide, this leads to a possible process constraining the deformation process. The model also predicts that pressure should enhance cross slip as core does not spread in the slip plane. This can be compared with studies of the pencil glide of screw dislocations in bcc iron (Ngan and Wen 2001, Marian *et al.* 2004). In case of iron the pencil glide dominates the regular kink-pair glide mechanism at higher strain rates. The Peierls barrier reported in this work could be a starting point for future works on describing the complex kink-pair mechanism associated with pencil glide in olivine.

6.5. Summary

Prior to this work, dislocation core structures in olivine have been modelled by Julien Durinck (Durinck *et al.* 2007) and Andrew Walker (Walker *et al.* 2005). The first work trying to link the dislocation core structure to the mechanical properties of olivine was the one of Durinck based on the PN model. It is obvious that the current work is in the continuity of this effort. One of our conclusions in front of the variety of core configurations computed here and the complexity of the energy landscape encountered by dislocation glide is that such a complexity cannot be captured by the PN approach. Such a complexity is challenging to understand the mechanical properties of olivine. An interesting hypothesis is to link the variety of core structures to the Si-O covalent bonds, qualitatively the spreading of the core is constrained by the tetrahedra, thus the SiO_4 network allows for different spreading. The situation is rather similar to what people computes for Si (Pizzagalli *et al.* 2018).

In particular, during this work, we only performed static calculations. And the main results are limited to core configurations and computation of the amount of lattice friction through the evaluation of Peierls stresses. The glide of dislocations is nevertheless driven not only by stress but also thermally activated. Our calculations can be viewed as a starting point to infer the effect of temperature on kink pairs mechanism of cross slip in Olivine.

7. Conclusion

The main aim of this work was to investigate the structure of dislocation cores, mobility and the associated energy landscapes of olivine (forsterite - Mg_2SiO_4), relying completely on atomistic simulations. The focus was on the modelling of [100] and [001] screw dislocation cores in *Pbnm* forsterite crystal structure for the upper mantle pressure range of 0 - 10 GPa. To perform these simulations on dislocation cores, this work began with the implementation of the required force-field model to an open-source classical molecular mechanics package. The inference of the study are as follows,

The core-shell potential library has been implemented to the LAMMPS molecular mechanics software as an auxiliary module to model the ionic and semi-ionic materials. The energy values and the force fields implemented with Wolf summation electrostatic term were compared to the existing core-shell implementation with traditional Ewald summation term. Further, the THB1 pair-potential parameters from the present work are validated by comparing the existing first-principle results from literature (Durinck *et al.* 2005) and were found to be in good agreement. The elastic-constant tensor validates for a system in equilibrium and the second derivative of the potential energy terms implemented. For validating the parameters of THB1 for systems far from equilibrium, like system containing dislocations, the theoretically generalized stacking faults are computed. The 1D and 2D γ-surface results are calculated using THB1 parameters. The pair-potential from the present implementation showed a well reproduced shape of the stacking-fault curves through regular minimisation scheme Case 1. The height of the stacking fault energy barriers is reproduced by the minimisation scheme Case 2 where cations are allowed to relax freely.

On successful validation of the implementation was established, the main focus was to model line defect properties. Initially, at a pressure of 0 GPa, [100] screw dislocations form a planar core with a strong spreading in (010) plane. The stable dislocation exhibits dissociation of the core as two strong ½[100] partial dislocations separated by an approximate distance of one lattice parameter along [001] direction (*i.e.*, ~7Å). The lattice friction against glide of this dislocation in the absence of thermal activation (at 0 K) is estimated using quasi-static loading. The Peierls stresses estimated for glide in (010) and

(001) are 2.76 GPa and 7 GPa respectively. The effect of pressure on the [100] dislocation core is studied, leading to two distinct domains, a low (0 – 4 GPa) and a high-pressure range (4 – 10 GPa). Below 4 GPa, the most stable core has a planar configuration spread in (010), but increasing pressure tends to stabilize a more compact core (*i.e.* with no well-developed dissociation into two partials). This is supported by the evolution of the camel hump shaped Peierls barrier computed using NEB calculations. Above 4 GPa, the dislocation core structure changes. A core spread in {021} core is identified to be energetically more favourable than the other cores and it has two variants due to the mirror symmetry of the *Pbnm* space group of forsterite. This dislocation core glides in {011} planes with Peierls stresses of 7 GPa (at P = 4 GPa) to 10 GPa (at P= 10 GPa). These Peierls stress values are in good agreement with the results from quasi-static loading conditions. From the path traced by the [100] screw dislocation to glide in {011}, we observed from the MEP, that the dislocation glides through (~~1~~001) and {021} but in the same direction. Such a glide of [100] dislocation through several planes has been reported experimentally by Raleigh (1968). It is usually called 'pencil glide'. Our work supports the occurrence of pencil glide in olivine at high-pressure conditions.

This change in stability of the dislocation core with pressure has strong implications on the slip system activities. Our calculations suggest that [100](010) is the most favourable slip system below 4 GPa, whereas at high pressures, [100]{011} is more favourable.

For [001] dislocations, two possible dislocation cores are proposed: the first type is a compact non-planar type "C" and the second is a dissociated core involving two 1/2[001] partials separated, in {110}, by a distance of 10.19Å. Based on the dislocation separation distance, the stacking fault energy is computed using equilibrium equation. The results are in agreement with the stacking fault energy obtained from the GSF calculations. From the comparison of core energy between dislocations of type "C" and "D" extracted from quadrupole arrangement of [001] dislocations, we show that the dissociated core of type "D" is the most stable. The stability of the core "D" is further validated when a shear stress is applied on the core of type "C" to enhance glide in (010) or (100). At stress values greater than the critical stress, the dislocation transforms into dissociated core of type "D" planar in {110}.

The stable core of type "D" is subjected to gradual shear loading to extract information on lattice friction in different planes. For a shear promoting glide of [001] dislocation in (100), we find that the dislocation starts to glide in {110} at a stress value greater than 3.94 GPa Based on Schmid's law, the resolved shear stress to trigger glide in {110} is found to be 1.51 GPa. The values of resolved stress to glide in {110} remains insensitive to increase in hydrostatic pressure in the system.

The [001] screw dislocation converts into a transient planar core at stress values greater than 6.10 GPa to glide in (010) plane.

The dislocation motion is associated with a transformation from a stable, rather immobile, core to a glissile core of higher energy configuration. This high-energy core may glide over several Peierls valleys before locking itself back in a particular one transforming back to a stable core. Based on such a jerky motion, it is proposed that dislocation glide follows a locking-unlocking mechanism as reported in hcp crystals (Caillard *et al.* 1993; Clouet *et al.* 2015). As predicted by the PN model (Carrez *et al.* 2008), the transient planar core compares well with the planar core of [001] dislocation spread in (010). The critical stress required to promote glide in (010) plane is indirectly proportional to pressure and further softens the [001](010) slip system.

Thus in this work, a semi-empirical potential model to model forsterite and its other high pressure polymorphs is implemented. The THB1 force field parameters for forsterite are tested and validated with the implementation. The properties of [100] and [001] screw dislocation cores are analysed and the results were extended for a pressure range of 0 – 10 GPa. An alternative to Peierls mechanism is proposed for glide of [001] screw dislocation in (010) via locking-unlocking mechanism. An experimental verification of such mechanism could be interesting. The effects of pressure and stress are studied in this work with the help of molecular static calculations. The understanding of the dislocation core structures computed in this work is intriguing and can be considered as a good starting point for future research.

Bibliography

Barber, D. J., Wenk, H.-R., Hirth, G., & Kohlstedt, D. L. (2010). Chapter 95 Dislocations in Minerals. In *Dislocations in Solids* (Vol. 16, pp. 171–232). Elsevier.

Beckstein, O., Klepeis, J. E., Hart, G. L. W., & Pankratov, O. (2001). First-principles elastic constants and electronic structure of α−Pt_2Si. *Physical Review B*, *63*(13), 134112.

Bowen, N. L., & Andersen, O. (1914). The binary system MgO-SiO_2. *American Journal of Science*, *s4-37*(222), 487–500.

Cai, W., Bulatob, V. V., Chang, J., Li, J., & Yip, S. (2003). Periodic image effects in dislocation modelling. *Philosophical Magazine*, *83*(5), 539–567.

Caillard, D., Couret, A., & Molenat, G. (1993). Mechanisms of yield stress anomalies in beryllium and Ni_3Al. *Materials Science and Engineering A*, *164*(1–2), 69–81.

Carrez, P., Godet, J., & Cordier, P. (2015). Atomistic simulations of ½〈110〉 screw dislocation core in magnesium oxide. *Computational Materials Science*, *103*, 250–255.

Carrez, P., Walker, A. M. M., Metsue, A., & Cordier, P. (2008). Evidence from numerical modelling for 3D spreading of [001] screw dislocations in Mg_2SiO_4 forsterite. *Philosophical Magazine*, *88*(16), 2477–2485.

Carter, N. L. and Ave'Lallemant, H. G. (1970). High temperature flow of dunite and peridotite. *Geological Society of America Bulletin*, 81**:** 2181-2202.

Catlow, C. R. A., Dixon, M., & Mackrodt, W. C. (1982). *Computer Simulation of Solids*. (C. R. A. Catlow & W. C. Mackrodt, Eds.) (Vol. 166). Berlin/Heidelberg: Springer-Verlag.

Clouet, E., Caillard, D., Chaari, N., Onimus, F., & Rodney, D. (2015). Dislocation locking versus easy glide in titanium and zirconium. *Nature Materials*, *14*(9), 931–936.

Clouet, E. (2017). BABEL. http://emmanuel.clouet.free.fr/Programs/Babel/

Couret, A., & Caillard, D. (1989). Glide in Prismatic Planes in Beryllium. An in situ Study. In *Strength of Metals and Alloys (ICSMA 8)* (pp. 211–216). Elsevier.

Couvy, H., Frost, D. J., Heidelbach, F., Nyilas, K., Ungár, T., Mackwell, S., & Cordier, P. (2004). Shear deformation experiments of forsterite at 11 GPa - 1400°C in the multianvil apparatus. *European Journal of Mineralogy*, *16*(6), 877–889.

Darot, M., & Gueguen, Y. (1981). High-Temperature Creep of Forsterite Single Crystals. *J. Geophys. Res.*, *86*(B7), 6219–6234.

Daw, M. S., & Baskes, M. I. (1984). Embedded-atom method: Derivation and application to impurities, surfaces, and other defects in metals. *Physical Review B*, *29*(12), 6443–6453.

de Leeuw, N. H., & Parker, S. C. (1998). Molecular-dynamics simulation of MgO surfaces in liquid water using a shell-model potential for water. *Physical Review B*, *58*(20), 13901–13908.

Deer, W. A., Howie, R. A., & Zussman, J. (1986). *Rock-Forming Minerals*. *Disilicates and Ring Silicates* (Vol. 1B). Longman.

Dick, B. G., & Overhauser, A. W. (1958). Theory of the Dielectric Constants of Alkali Halide Crystals. *Physical Review*, *112*(1), 90–103.

Downs, R. T., Zha, C. S., Duffy, T. S., & Finger, L. W. (1996). The equation of state of forsterite to 17.2 GPa and effects of pressure media. *American Mineralogist*, *81*(1–2), 51–55.

Durham, W. B., & Goetze, C. (1977). Plastic flow of oriented single crystals of olivine: 1. Mechanical data. *Journal of Geophysical Research*, *82*(36), 5737–5753.

Durham, W. B., Goetze, C., & Blake, B. (1977). Plastic flow of oriented single crystals of olivine: 2. Observations and interpretations of the dislocation structures. *Journal of Geophysical Research*, *82*(36), 5755–5770.

Durinck, J., Carrez, P., & Cordier, P. (2007). Application of the Peierls-Nabarro model to dislocations in forsterite. *European Journal of Mineralogy*, *19*(5), 631–639.

Durinck, J., Legris, A., & Cordier, P. (2005a). Pressure sensitivity of olivine slip systems: First-principle calculations of generalised stacking faults. *Physics and Chemistry of Minerals, 32*(8–9), 646–654.

Durinck, J., Legris, A., & Cordier, P. (2005b). Influence of crystal chemistry on ideal plastic shear anisotropy in forsterite: First principle calculations. *American Mineralogist*, *90*(7), 1072–1077.

Durinck, J. (2005c). Modélisation de la plasticité de la forsterite par calculs à l'échelle atomique et par dynamique des dislocations. *Universite de Lille 1*, Order number : 3661.

Dziewonski, A. M., & Anderson, D. L. (1981). Preliminary reference Earth model. *Physics of the Earth and Planetary Interiors*, *25*(4), 297–356.

Evans, B., & Goetze, C. (1979). The temperature variation of hardness of olivine and its implication for polycrystalline yield stress. *Journal of Geophysical Research*, *84*(B10), 5505–5524.

Fennell, C. J., & Gezelter, J. D. (2006). Is the Ewald summation still necessary? Pairwise alternatives to the accepted standard for long-range electrostatics. *The Journal of Chemical Physics*, *124*(23), 234104.

Gaboriaud, R. J. (1986). Dislocations in olivine single crystals indented between 25 and 1100 °C. *Bull. Mineral.*, *109*, 185–191.

Gaboriaud, R. J., Darot, M., Gueguen, Y., & Woirgard, J. (1981). Dislocations in olivine indented at low temperatures. *Physics and Chemistry of Minerals, 7*(2), 100–104.

Gale, J. D. (1997). GULP: A computer program for the symmetry-adapted simulation of solids. *Journal of the Chemical Society-Faraday Transactions*, *93*(4), 629–637.

Gale, J. D. (2005). Interatomic Potential Models for Ionic Materials. In *Handbook of Materials Modeling* (pp. 479–497). Dordrecht: Springer Netherlands.

Garvik, N., Carrez, P., Garruchet, S., & Cordier, P. (2015). Numerical modeling of the core structure of [100] dislocations in Fe_3C cementite. *Scripta Materialia*, *99*, 61–64.

Goryaeva, A. M., Carrez, P., & Cordier, P. (2015). Modeling defects and plasticity in $MgSiO_3$ post-perovskite: Part 1—generalized stacking faults. *Physics and Chemistry of Minerals*.

Gouriet, K., Carrez, P., & Cordier, P. (2014). Modelling [1 0 0] and [0 1 0] screw dislocations in $MgSiO_3$ perovskite based on the Peierls–Nabarro–Galerkin model. *Modelling and Simulation in Materials Science and Engineering*, *22*(2), 025020.

Gueguen, P. Y., & Darot, M. (1982). Les dislocations dans la forsté rite déformée à haute Tempé rature. *Philosophical Magazine A*, *45*(3), 419–442.

Gueguen, Y. (1979). Dislocations in naturally deformed terrestrial olivine: classification, interpretation, applications. *Bull. Mineral.*, *102*, 178–183.

Henkelman, G., Uberuaga, B. P., & Jónsson, H. (2000). Climbing image nudged elastic band method for finding saddle points and minimum energy paths. *Journal of Chemical Physics*, *113*(22), 9901–9904.

Hirel, P., Kraych, A., Carrez, P., & Cordier, P. (2014). Atomic core structure and mobility of [100](010) and [010](100) dislocations in MgSiO3 perovskite. *Acta Materialia*, *79*, 117–125.

Hirel, P. (2015). Atomsk: A tool for manipulating and converting atomic data files. *Computer Physics Communications*, *197*, 212–219.

Hirth, J. P., & Lothe, J. (1968). *Theory of Dislocations*. Graw-Hill.

Idrissi, H., Bollinger, C., Boioli, F., Schryvers, D., & Cordier, P. (2016). Low-temperature plasticity of olivine revisited with in situ TEM nanomechanical testing. *Science Advances*, *2*(3), e1501671–e1501671.

Isaak, D. G., Anderson, O. L., Goto, T., & Suzuki, I. (1989). Elasticity of single-crystal forsterite measured to 1700 K. *Journal of Geophysical Research*, *94*(B5), 5895.

Ismail-Beigi, S., & Arias, T. a. (1999). Ab Initio Study of Screw Dislocations in Mo and Ta: A new picture of plasticity in bcc transition metals. *Physical Review Letters*, *84*(7), 1499–1502.

Jaupart, C., & Mareschal, J.-C. (2015). Heat Flow and Thermal Structure of the Lithosphere. In *Treatise on Geophysics* (pp. 217–253). Elsevier.

Jónsson, H., Mills, G., & Jacobsen, K. W. (1998). Nudged elastic band method for finding minimum energy paths of transitions. In *Classical and Quantum Dynamics in Condensed Phase Simulations* (pp. 385–404).

Jung, H., & Karato, S.-I. (2001). Effects of water on dynamically recrystallized grain size of olivine. *Journal of Structural Geology*, *23*, 1337–1344.

Kashima, K., I. S. and K. S. (1983). Plastic deformation of olivine single crystals. In *Science Reports ofthe Tohoku University. series III* (pp. 281–407). Sendai, Japan.

Klein, C., & Hurlbut, C. S. (1999). *Manual of Mineralogy (after James D. Dana)*. Wiley.

Kohlstedt, D. L., & Goetze, C. (1974). Low-stress high-temperature creep in olivine single crystals. *Journal of Geophysical Research*, *79*(14), 2045–2051.

Kohlstedt, D. L., Goetze, C., Durham, W. B., & Sande, J. V. (1976). New Technique for Decorating Dislocations in Olivine. *Science*, *191*(4231), 1045–1046.

Kraych, A., Carrez, P., Hirel, P., Clouet, E., & Cordier, P. (2016a). Peierls potential and kink-pair mechanism in high-pressure $MgSiO_3$ perovskite: An atomic scale study. *Physical Review B*, *93*(1), 014103.

Kraych, A., Carrez, P., & Cordier, P. (2016b). On dislocation glide in MgSiO3 bridgmanite at high-pressure and high-temperature. *Earth and Planetary Science Letters*, *452*, 60–68.

Lehto, N., & Öberg, S. (1998). Effects of Dislocation Interactions: Application to the Period-Doubled Core of the 90° Partial in Silicon. *Physical Review Letters*, *80*(25), 5568–5571.

Lewis, G. V, & Catlow, C. R. A. (1985). Potential models for ionic oxides. *Journal of Physics C: Solid State Physics*.

Li, B., Gwanmesia, G. D., & Liebermann, R. C. (1996). Sound velocities of olivine and beta polymorphs of Mg_2SiO_4 at Earth's transition zone pressures. *Geophysical Research Letters*, *23*(17), 2259–2262.

Mackwell, S. J., Kohlstedt, D. L., & Paterson, M. S. (1985). The role of water in the deformation of olivine single crystals. *Journal of Geophysical Research*, *90*(5), 11319.

Mainprice, D., Tommasi, A., Couvy, H., Cordier, P., & Frost, D. J. (2005). Pressure sensitivity of olivine slip systems and seismic anisotropy of Earth's upper mantle. *Nature*, *433*(7027), 731–733.

Marian, J., Cai, W., & Bulatov, V. V. (2004). Dynamic transitions from smooth to rough to twinning in dislocation motion. *Nature Materials*, *3*(3), 158–163.

Matsui, M. (1998). Breathing shell model in molecular dynamics simulation: Application to MgO and CaO. *The Journal of Chemical Physics*, *108*(8), 3304–3309.

Matsui, M., & Busing, W. R. (1984). Calculation of the elastic constants and high-pressure properties of diopside, CaMgSi2O6. *American Mineralogist*.

Mitchell, P. J., & Fincham, D. (1993). Shell model simulations by adiabatic dynamics. *Journal of Physics: Condensed Matter*, *5*(8), 1031–1038.

Ohtani, E., & Kumazawa, M. (1981). Melting of forsterite Mg_2SiO_4up to 15 GPa. *Physics of the Earth and Planetary Interiors*, *27*(1), 32–38.

Orowan, E. (1934). Zur Kristallplastizität. III. *Zeitschrift Für Physik*, *89*(9–10), 605–613.

Peierls, R. (1940). The size of a dislocation. *Proceedings of the Physical Society*, *52*(1), 34–37.

Phakey, P., Dollinger, G., & Christie, J. (1972). Transmission Electron Microscopy of Experimentally Deformed Olivine Crystals. In *American Mineralogist* (Vol. 61, pp. 117–138). American Geophysical Union.

Pizzagalli, L., Godet, J., & Brochard, S. (2018). Influence of strain on dislocation core in silicon. *Philosophical Magazine*, *98*(13), 1151–1169.

Plimpton, S. (1995). Fast Parallel Algorithms for Short – Range Molecular Dynamics. *Journal of Computational Physics*, *117*(June 1994), 1–19.

Plimpton, S. J., & Thompson, A. P. (2012). Computational aspects of many-body potentials. *MRS Bulletin*, *37*(05), 513–521.

Poirier, J.-P. (1975). On the slip systems of olivine. *Journal of Geophysical Research*, *80*(29), 4059–4061.

Polak, E., & Ribiere, G. (1969). Note sur la convergence de méthodes de directions conjuguées. *Revue Française d'informatique et de Recherche Opérationnelle. Série Rouge*, *3*(16), 35–43.

Polanyi, M. (1934). Über eine Art Gitterstörung, die einen Kristall plastisch machen könnte. *Zeitschrift Für Physik*, *89*(9–10), 660–664.

Price, G. D., & Parker, S. C. (1984). Computer simulations of the structural and physical properties of the olivine and spinel polymorphs of Mg_2SiO_4. *Physics and Chemistry of Minerals*, *10*(5), 209–216.

Price, G. D., & Parker, S. C. (1987). The Lattice Dynamics of Forsterite. *Mineralogical Magazine*, *51*(359), 157–170.

Price, G. D., Parker, S. C., & Leslie, M. (1987). The lattice dynamics and thermodynamics of the Mg_2SiO_4 polymorphs. *Physics and Chemistry of Minerals*, *15*(2), 181–190.

Raleigh, C. B. (1968). Mechanisms of plastic deformation of olivine. *Journal of Geophysical Research*, *73*(16), 5391–5406.

Raterron, P., Amiguet, E., Chen, J., Li, L., & Cordier, P. (2009). Experimental deformation of olivine single crystals at mantle pressures and temperatures. *Physics of the Earth and Planetary Interiors*, *172*(1–2), 74–83.

Raterron, P., Chen, J., Geenen, T., & Girard, J. (2011). Pressure effect on forsterite dislocation slip systems: Implications for upper-mantle LPO and low viscosity zone. *Physics of the Earth and Planetary Interiors*, *188*(1–2), 26–36.

Raterron, P., Chen, J., Li, L., Weidner, D., & Cordier, P. (2007). Pressure-induced slip-system transition in forsterite: Single-crystal rheological properties at mantle pressure and temperature. *American Mineralogist*, *92*(8–9), 1436–1445.

Raterron, P., Wu, Y., Weidner, D. J., & Chen, J. (2004). Low-temperature olivine rheology at high pressure. *Physics of the Earth and Planetary Interiors*, *145*(1–4), 149–159.

Ringwood, A. E. (1962). A model for the upper mantle. *Journal of Geophysical Research*, *67*(11), 4473–4478.

Ringwood, A. E. (1975). *Composition and petrology of the earth's mantle*. McGraw-Hill.

Rodney, D., & Proville, L. (2009). Stress-dependent Peierls potential: Influence on kink-pair activation. *Physical Review B*, *79*(9), 094108.

Sanders, M. J., Leslie, M., & Catlow, C. R. A. (1984). Interatomic potentials for SiO_2. *Journal of the Chemical Society, Chemical Communications*, (19), 1271.

Sangster, M. J. L. (1973). Interionic potentials and force constant models for rocksalt structure crystals. *Journal of Physics and Chemistry of Solids*, *34*(2), 355–363.

Sangster, M. J. L., Peckham, G., & Saunderson, D. H. (1970). Lattice dynamics of magnesium oxide. *Journal of Physics C: Solid State Physics*, *3*(5), 1026–1036.

Schoeck, G. (2005). The Peierls model: Progress and limitations. *Materials Science and Engineering: A*, *400–401*(1–2 SUPPL.), 7–17.

Schoeck, G. (2006). The core structure of dislocations: Peierls model vs. atomic simulation. *Acta Materialia*, *54*(18), 4865–4870.

Schröder, U. (1966). A new model for lattice dynamics ("breathing shell model"). *Solid State Communications*, *4*(7), 347–349.

Sheppard, D., Terrell, R., & Henkelman, G. (2008). Optimization methods for finding minimum energy paths. *The Journal of Chemical Physics*, *128*(13), 134106.

Shimizu, H., Bassett, W. A., & Brody, E. M. (1982). Brillouin-scattering measurements of single-crystal forsterite to 40 kbar at room temperature. *Journal of Applied Physics*, *53*(1), 620–626.

Smyth, J. R., & Hazen, R. M. (1973). The Crystal Structures of Forsterite and Hortonolite at Several Temperatures Up to 900 °C. *American Mineralogist*, *58*, 588–593.

Steeds, J.W., and Willis, J. R. (1979). Dislocations in Anisotropic Media. In *Dislocations in Solids, The Elastic Theory* (pp. 143–165). Amsterdam, Netherlands: North-Holland Publishing Company, Amsterdam.

Steeds, J. W. (1973). *Introduction to anisotropic elasticity theory of dislocations*. Clarendon Press.

Stillinger, F. H., & Weber, T. A. (1985). Computer simulation of local order in condensed phases of silicon. *Physical Review B*, *31*(8), 5262–5271.

Sun, X. W., Chu, Y. D., Song, T., Liu, Z. J., Zhang, L., Wang, X. G., Chen, Q. F. (2007). Application of a shell model in molecular dynamics simulation to ZnO with zinc-blende cubic structure. *Solid State Communications*, *142*(1–2), 15–19.

Sun, X. Y., Taupin, V., Fressengeas, C., & Cordier, P. (2016). Continuous description of the atomic structure of grain boundaries using dislocation and generalized-disclination density fields. *International Journal of Plasticity*, *77*, 75–89.

Taylor, G. I. (1934). The Mechanism of Plastic Deformation of Crystals. Part I. Theoretical. *Proceedings of the Royal Society A: Mathematical, Physical and Engineering Sciences*, *145*(855), 362–387.

Taylor, G. I., & Elam, C. F. (1926). The Distortion of Iron Crystals. *Proceedings of the Royal Society A: Mathematical, Physical and Engineering Sciences*, *112*(761), 337–361.

Thompson, A. P., Plimpton, S. J., & Mattson, W. (2009). General formulation of pressure and stress tensor for arbitrary many-body interaction potentials under periodic boundary conditions. *The Journal of Chemical Physics*, *131*(15), 154107.

Vítek, V. (1968). Intrinsic stacking faults in body-centred cubic crystals. *Philosophical Magazine*, *18*(154), 773–786.

Walker, A., Gale, J., Slater, B., & Wright, K. (2005). Atomic scale modelling of the cores of dislocations in complex materials part 1: methodology. *Physical Chemistry Chemical*, 3227–3234.

Walker, A. M. A., Gale, J. J. D., Slater, B., Wright, K., Faraday, D., Street, G., & Laboratories, C. I. (2005). Atomic scale modelling of the cores of dislocations in complex materials part 2: applications. *Physical Chemistry Chemical Physics : PCCP*, *7*(17), 3235–3242.

Wang, Y., Liebermann, R. C., & Boland, J. N. (1988). Olivine as an in situ piezometer in high pressure apparatus. *Physics and Chemistry of Minerals*, *15*(5), 493–497.

Wolf, D., Keblinski, P., Phillpot, S. R., & Eggebrecht, J. (1999). Exact method for the simulation of Coulombic systems by spherically truncated, pairwise r[sup −1] summation. *The Journal of Chemical Physics*, *110*(17), 8254.

Yang, L. ., & Moriarty, J. . (2001). Kink-pair mechanisms for a/2 <111> screw dislocation motion in bcc tantalum. *Materials Science and Engineering: A*, *319–321*, 124–129. [License number for Figure 2.7. (Figure 1 in journal): 4386411385982]

Yoneda, A., & Morioka, M. (2013). Pressure Derivatives of Elastic Constants of Single Crystal Forsterite (pp. 207–214).

Yokokura, T. (1981). Viscosity of the earth's mantle: Inference from dynamic support by flow stress. *Tectonophysics*, *77*(1–2), 35–62.

Zha, C.-S., Duffy, T. S., Downs, R. T., Mao, H.-K., & Hemley, R. J. (1996). Sound velocity and elasticity of single-crystal forsterite to 16 GPa. *Journal of Geophysical Research: Solid Earth*, *101*(B8), 17535–17545.

Zhang, Y., Hong, J., Liu, B., & Fang, D. (2009). Molecular dynamics investigations on the size-dependent ferroelectric behavior of BaTiO3 nanowires. *Nanotechnology*, *20*(40), 405703.

List of abbreviations

bcc	Body centred cubic lattice
CG	Conjugate Gradient
CPO	Crystal Preferred Orientation
DD map	Differential Displacement map
DFT	Density Function Theory
EAM	Embedded Atom Method
Fp	Ferropericlase
GSF	Generalized Stacking Fault
GULP	General Utility Lattice Program
hcp	Hexagonal close packed lattice
LAMMPS	Large-scale Atomic/Molecular Massively Parallel Simulator.
LPO	Lattice Preferred Orientation
MEP	Minimum Energy Path
NEB	Nudged Elastic Band method
PN model	Peierls-Nabarro model
V_P	Peierls potential
PREM	Preliminary Reference Earth Model
Pv	Perovskite
SD	Steepest Descent
TB	Tight-Binding method
TEM	Transmission Electron Microscopy

Acknowledgements

Firstly, I would like to express my sincere gratitude to my thesis supervisors Prof. Philippe Carrez and Prof. Patrick Cordier for their continuous support of my PhD study, for their patience, motivation, and immense knowledge. Their guidance helped me in all the time of research and writing of this thesis. I could not have imagined having better advisors and mentors for my PhD study.

Besides my supervisors, I would like to thank my thesis committee: Prof. Sandrine Brochard, Prof. Sandro Scandolo, Dr. Andréa Tommasi, and Dr. Andrew Walker for examining this PhD thesis and for the insightful comments, but also for the questions which helped in improving this thesis manuscript.

I believe I made a right choice to prepare my PhD thesis with the Rheoman team. I am grateful to Philippe and Patrick for the freedom given to express my ideas and had taught me the ways to approach scientific problems. The atmosphere in the team helped me to sharpen my skills and to develop confidence to introduce myself to the scientific community. A special mention has to be given to Pierre Hirel, for the discussions we had which helped me to understand several scientific concepts and for his ATOMSK code. I thank Karine Gouriet for helping me to settle down during my initial days in France. Further I would like to thank Riccardo Reali and Alexandra Goryaeva with whom I started my PhD thesis, I cherish every moment we shared and supported each other. Also I thank Billy Clitton Nzogang who joined us later for his support. I would also like to say my thanks to other members of the team Alexande Mussi, Antoine Kraych, Sebastian Ritterbex, Franchesca Boioli and Xiao-Yu Sun for their advice and for their kind presence.

I'd like to personally thank Dr. Sebastien Groh and Prof. Meinhard Kuna for the opportunity they gave me to come in Europe and priceless hours spent on developing my skills in numerical modelling. Words can't explain my gratitude to them and TU Bergakademie Freiberg for the Computational Materials Science International Master’s program.

I would like to thank my friends Manjula Vinod and Godwin Vargheese for the support and encouragement they provided me.

Above all I am grateful for the constant support and encouragement provided by my parents, brother and in-laws. I am thankful for their belief in me to move far from home to achieve my dreams.

Finally, I take this opportunity to thank my better half Sowmiya Theivaprakasam for joining me this far and to support, motivate and guide me to finish this PhD thesis successfully.